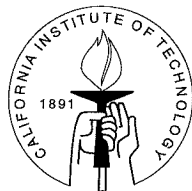# Nonlinear Control and Modeling of Rotating Stall in an Axial Flow Compressor

Thesis by
Robert L. Behnken

In Partial Fulfillment of the Requirements
for the Degree of
Doctor of Philosophy

California Institute of Technology
Pasadena, California

1997

(Defended September 3, 1996)

Acknowledgements

One of the greatest things about being at Caltech is that it makes writing acknowledgements very difficult; there are so many to thank. Nearly everyone I've come in contact with was very helpful and responsive in all aspects of my education. I would therefore like to take this time to thank the community that is Caltech. In addition to the community, I would also like to recognize a few individuals as well.

I owe thanks to the undergraduate students who helped accomplish many of the tasks associated with experimentation on the Caltech rig. Asif Khalak built the initial Caltech compressor rig, Dave Richards built and tested the air injection actuator ring, and Mina Leung performed much of the final open loop testing to determine the optimal air injection positioning.

My fellow graduate students also helped extensively. For research on the compressor, Raffello D'Andrea made an excellent partner for investigating air injection control on the Caltech rig. Raff made even not accomplishing anything in the sub-basement of Thomas (where the compressor rig lives) interesting. Simon Yeung was also a great help in keeping the compressor in running condition. Indirect help in my research came from several other friends, including: Sudipto Sur, Michiel van Nieuwstadt, Robert M'Closkey, and Andrew Lewis. A special thanks goes to Carl Wassgren and his wife Sarah.

While the faculty at Caltech have all been helpful, I would like to specifically thank Prof. Christopher Brennen for the insightful discussions. In addition, Prof. Richard Murray was also helpful (which is an understatement). Richard's energy and enthusiasm for all things were highlights of my Caltech career.

I would like to dedicate this work to my father, and thank him for all the times he worked harder to make my life a little easier.

Nonlinear Control and Modeling of Rotating Stall in an Axial Flow Compressor
by
Robert L. Behnken

In Partial Fulfillment of the
Requirements for the Degree of
Doctor of Philosophy

Abstract

This thesis focuses on understanding the use of air injection as a means of controlling rotating stall in an axial flow compressor, involving modeling, dynamical systems analysis, and experimental investigations.

The first step towards this understanding was the development of a low order model for air injection control, the starting point of which was the Moore and Greitzer model for axial flow compressors. The Moore and Greitzer model was extended to include the effects of air injection and bifurcation analysis was performed to determine how the closed loop system dynamics are different from those of the open loop system. This low order model was then used to determine the optimal placement of the air injection actuators.

Experimental work focused on verifying that the low order model, developed for air injection actuation, qualitatively captured the behavior of the Caltech compressor rig. Open loop tests were performed to determine how the placement of the air injectors on the rig affected the performance of the compressor. The positioning of the air injectors that provided the greatest control authority were used in the development of air injection controllers for rotating stall. The controllers resulted in complete elimination of the hysteresis associated with rotating stall. The use of a throttle actuator for the control of the surge dynamics was investigated, and then combined with an air injection controller for rotating stall; the resulting controller performed quite well in throttle disturbance rejection tests.

A higher order model was developed to qualitatively match the experimental results with a simulation. The results of this modeling effort compared quite well with the experimental results for the open loop behavior of the Caltech rig. The details of how the air injection actuators affect the compressor flow were included in this model, and the simulation predicted the same optimal controller that was developed through experimentation.

The development of the higher order model also included the investigation of systematic methods for determining the simulation parameters. Based on experimental measurements of compression system transients, the open loop simulation parameters were identified, including values for the compressor performance characteristic in regions where direct measurements were not possible. These methods also provided information on parameters used in the modeling of the pressure rise delivered by the compressor under unsteady flow conditions.

Contents

List of Figures

List of Tables

List of Symbols

Symbol	Description and page when applicable
A_d	Duct area, 12
A_n	Amplitude of the nth circumferential Fourier mode of rotating stall flow perturbation, 16
B	Greitzer surge parameter, 14
C_x	Mean velocity in the compressor annulus, 24
ΔP	Pressure difference, 12
δC_{x_1}	Velocity perturbation at station 1, 24
δC_{x_2}	Velocity perturbation at station 2, 24
$\delta\phi$	Flow coefficient perturbation, 15
δp_{t_1}	Total pressure perturbation at station 1, 24
δp_{t_2}	Total pressure perturbation at station 2, 24
$\delta\Theta$	Perturbation velocity potential, 15
ϵ	Singular perturbation parameter, 25
η	Nondimensional axial position, 15
γ	Throttle coefficient, proportional to throttle opening, 13
J_1	Square amplitude of the first circumferential Fourier mode of rotating stall, 17
λ	Inertia parameter for fluid in the rotor, 14
l_c	Effective overall compressor duct length, 14
l_e	Nondimensional exit duct length, 14
l_i	Nondimensional inlet duct length, 14
L_r	Total pressure loss across the rotor, 33
L_{rs}	Steady total pressure loss across the rotor, 34
L_s	Total pressure loss across the stator, 33
L_{ss}	Steady total pressure loss across the stator, 34
$\dot{m}$	Mass flow rate, 12
M_n	Amplitude of the nth circumferential Fourier mode of rotating stall static pressure perturbation, 79
μ	Inertia parameter for fluid in the compressor, 14
p_e	Static pressure downstream of the compressor, 14
Φ	Annulus average flow coefficient, 12

Chapter 1

Introduction

1.1 Background

The design process for gas turbine engines has become quite mature in the sense that substantial performance increases have become harder to achieve. While most avenues in the design process have been deeply explored, one area of performance enhancement that has not be fully exploited is that of control. One reason for this is that the amount of complexity added by a control system has been, until recently, a major concern. Currently, the presense of full authority digital engine controllers (FADECS) on most modern aircraft has decreased the amount of additional hardware required to take advantage of more sophisticated control techniques. In addition to computation power, engine hardware is also being added to aid engine operability and to help eliminate startup transients. This additional equipment could also be exploited for control purposes.

It was recently shown that passive control techniques can be used to increase both engine efficiency and power output on actual full scale engines. The simulation study by Smith et al. [42] reported a 15% increase in thrust and 3% decrease in fuel consumption with the use of a controller that scheduled engine parameters, and experimental validation of these results was presented by Gilyard and Orme [17]. The experiments involved subsonic flight tests of an F-15 airplane at the NASA Dryden Flight Research Center, and showed up to 15% increase in thrust and a 1–2% decrease in fuel consumption. These increases in performance and efficiency for one of the highest performance aircraft in the world suggest that other aircraft would also see benefits from similar controls.

The preceding results show that performance and efficiency can be increased by using passive control techniques, and suggest that active techniques could also be beneficial. This thesis investigates one active technique that results in performance improvements by allowing the operation of the engine in previously unusable regions. These unusable regions are typically due to the presense of instabilities in the compression system under low flow/high pressure rise conditions; unfortunately the peak performance of the compressor is also achieved near the operating conditions at which these instabilities occur.

Two of the performance limiting factors for which active control holds promise
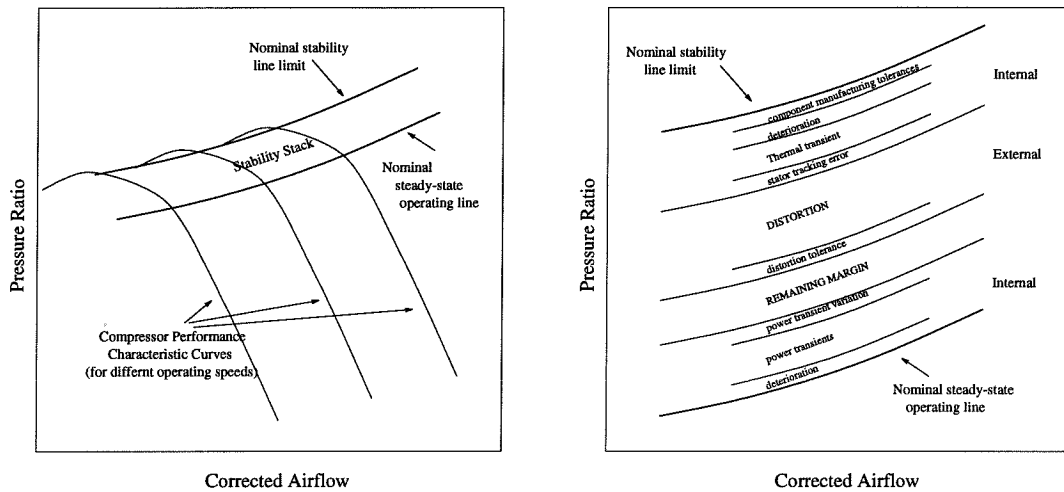
Figure 1.1 Typical components of the stability stack for a jet engine.

are rotating stall and surge. Rotating stall is a non-axisymmetric instability that is localized to the compressor, and involves periodic stalling and unstalling in the blade passages. Surge is a violent system level axisymmetric oscillation that is due to the overall dynamics of the pumping system.

Figure 1.1 shows a *stability stack* for a typical jet engine, which is a graph of the amount of margin required to avoid performance limiting instabilities due to different factors. On the left side of the figure, several compressor performance characteristics are shown along with the stability stack. These characteristics show the pressure that is delivered by the compressor at a given flow rate. The *nominal stability line* is where a compressor system would start to exhibit some sort of instability (typically rotating stall or surge) under ideal operating conditions. Since the operating conditions are never ideal, the compressor must be operated some distance away from this curve in order to avoid instability. The stability margin for a given effect is the distance away from the nominal stability line that the compressor must be operated in order to avoid instability. Examples of effects for which stability margins are included are distortion and power transients; others are listed in the figure. The *nominal steady state operating line* is the curve where compressor system would start to exhibit instability under worst case operating conditions. This worst case is obtained by adding up all of the individual margins, and this sum of all of the individual margins is called the stability stack. The stability stack therefore tells how much margin must be included in order to avoid instability. An open area of research is in determining how to sum the individual margins into the stability stack; it is not clear that a linear combination is the correct way to combine the margins. Each of the components in the stack could possibly be decreased if the performance limiting instabilities (rotating stall and surge) could be damped by active control. In order to better describe the possibilities for active control, further description of the performance limiting instabilities is now in order.
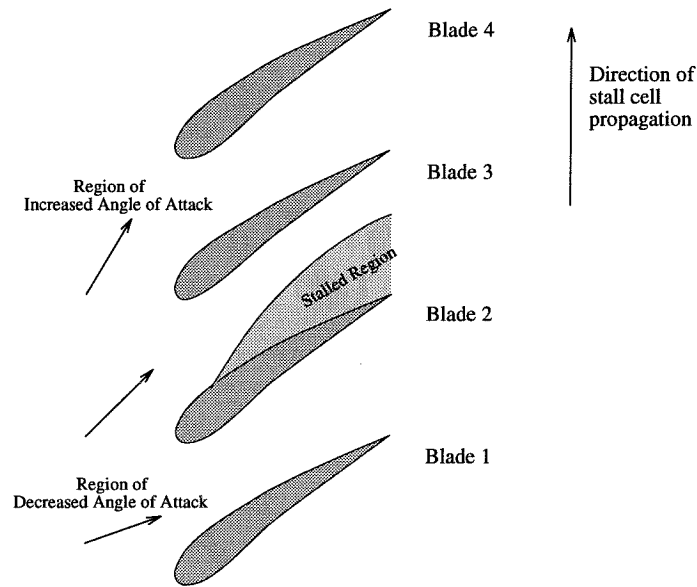
Figure 1.2 Emmons model for stall cell propagation.

The Emmons [13] model for rotating stall is shown in Figure 1.2, and provides a simple explanation for stall cell formation and propagation. As the throttle on the compressor is slowly closed, the angle of attack on the blades increases to a point where the flow separates on one of the blades; this creates a blockage that the flow is redirected around. This flow redirection causes the angle attack for the passage below the stalled region to be decreased; this makes this lower passage less likely to stall. On the blade passage above the stalled passage the angle of attack is increased; this makes this above passage more likely to stall. This effect causes the stall cell to rotate around the compressor annulus.

Surge is caused by the alternating storage and release of compressed air in the downstream ducting of the compressor. The compressibility of the air acts as a spring system, and the nonlinear compressor performance characteristic provides negative damping to this spring system under some operating conditions, and this effect leads to surge.

While these two instabilities are often modeled as separate phenomena, there is coupling between them, and rotating stall is a precursor to the onset of surge in many engines. In fact, recent work by Day [12] suggests that rotating stall causes the onset of surge. In addition to the coupling with surge, rotating stall has a large hysteresis loop associated with it. This hysteresis results in the requirement of large swings in operating conditions in order to recover from a stalled condition (in practice, recovery is usually accomplished by shutting the engine down and restarting it). A more detailed description of these and other instabilities that limit the performance of compression systems can be found in the survey paper by Greitzer [19].

While these two instabilities limit performance, there are other reasons that they must be avoided. On high speed engines (high speed refers to the Mach number

being high, and therefore that compressibility effects are important), rotating stall leads to drastic increases in compressor stage temperature and can lead to titanium fires [12]. During deep surge, reverse flow through the engine can lead to combustion gases exiting the engine inlet and can create large pressure spikes in the combustor. Rotating stall and surge must therefore be avoided not only because of the performance limitations that they are associated with, but also because they can cause severe damage to, or even failure of, the engine. Active control research for axial flow compressors therefore focuses on developing techniques for both decreasing the performance limitations associated with these instabilities and on developing active disturbance rejection techniques for avoiding them.

1.2 Previous Work

This thesis builds on several research areas which currently make up the state of the art in active control of rotating stall and surge. Ideas from compression system modeling, dynamical systems analysis, and experimental turbomachinery are combined in this thesis, and an overview of the recent work in these fields which has been applied to active control of compression systems is presented here.

1.2.1 Modeling and analysis

The centerpiece of nearly all theoretical work in the area of control of rotating stall and surge for axial flow compressors is the model developed by Greitzer beginning with [18] and Moore in [34]. Their work culminated in what is now referred to as the MG–3 model, for Moore and Greitzer three state model, and was first presented in [35]. This work is significant because it provides a low order nonlinear model which captures many of the qualitative features seen in these types of compression systems. Initial work at showing how the MG–3 model captures the behavior previously seen in experiments was performed by the same authors [20]. The Moore and Greitzer model consists of a partial differential equation (PDE) which describes the dynamics of an axial flow compressor. By assuming a potential flow solution for the flow perturbations in the inlet duct in the form of a Fourier series, the MG–3 model can be developed from this PDE by truncating the series at a single mode.

The first dynamical systems analysis performed on this model was presented by McCaughan in [32] and [33], where it was shown that the transition to rotating stall is captured as a transcritical bifurcation and that the transition to surge is captured as a Hopf bifurcation in the MG–3 model. Greitzer originally developed the B parameter [18] in order to calculate whether a given compressor would surge or transition to rotating stall, and McCaughan showed that the value of this parameter in the MG–3 model did help decide which of the instabilities would be dominant. She went on to show that the phenomena of classical and deep surge and the hysteresis associated with the jump to rotating stall were all present in the model, and could be explained from a dynamical systems standpoint. A similar analysis was performed by Abed et al. [1].

While the MG–3 model does capture much of the qualitative behavior of axial flow compressors, it does a poor job of quantitatively matching experimental data. In order to better match experimental measurements of rotating stall dynamics other researchers have included more terms in the Fourier series of the original Moore and Greitzer PDE description, and have extended the model to include additional effects. These additional modes and effects increase the order of the model substantially, but result in better correlation with experimental data. One of the most successful modeling examples was presented by Mansoux et al. [31], where time traces from flow measurements directly upstream of the compressor rotor face matched simulation results extremely well. The model used by Mansoux et al. has been labeled as the distributed model and includes higher Fourier modes for the flow perturbations at the rotor face as well as dynamics for the presure rise delivered by the compressor as the flow rate through the system is changed. These dynamics (also referred to as unsteady loss dynamics) for the response of the compressor pressure delivery to changes in the flow conditions were suggested by Haynes et al. [23], and are essential for matching simulation and experimental data.

Initial work in active control for axial flow compressors focused on designing throttle controllers for the low order MG–3 model. Throttle control techniques are one dimensional in nature since they act only on the circumferential averaged flow through the compressor. Liaw and Abed [30] developed the first model based controller for rotating stall. The most interesting aspect of their results is that the control law can eliminate the hysteresis loop associated with rotating stall. This is accomplished by stabilizing an unstable solution to the MG–3 equations which corresponds to small amplitude rotating stall (small is relative to the fully developed rotating stall that is open loop stable in the MG–3 model). Additional throttle controller design on the MG–3 model was performed by Krstić et al. [29] using backstepping techniques. The resulting controllers had similar effects of stabilizing the unstable equilibria associated with small amplitude rotating stall and, in addition, stabilized the surge dynamics.

The first extensive studies on 2-D actuation schemes for preventing rotating stall were performed by Hendricks and Gysling [24]. This work compared the linear stability of different actuator and sensing strategies to determine which was the most successful at extending the operating region of a compressor system. The result for actuation techniques was that the injection of air upstream of the rotor was the most promising method of controlling the transition to rotating stall. Further work on modeling air injection was presented by Gysling [22], where aeromechanical feedback was used to open a set of air injection ports upstream of the compressor face in response to static pressure perturbations at the outer wall of the compressor annulus.

1.2.2 Experimental results

There are several active control techniques that have been experimentally shown to decrease the detrimental effects of rotating stall in axial flow compressors, including active inlet guide vanes, high speed bleed valves, and air injection.

Control using inlet guide vane actuators works by damping out the small amplitude circumferential flow perturbations which grow into rotating stall. Paduano et al. [38, 39] and Haynes et al. [23] have both succeeded in controlling rotating stall using this type of actuation. By damping out the first several circumferential Fourier modes of the inlet flow perturbations, inlet guide vanes have been successfully used to extended the operating region of full size axial flow compressors. These methods provided as high as 18% decrease in the stalling mass flow [39].

High speed bleed valves work to control rotating stall by using the coupling between the surge and the rotating stall dynamics as described by the MG–3 model. Experimental results for controlling rotating stall using this method were presented by Badmus et al. [3], and a combined surge and rotating stall bleed valve controller was presented by Eveker et al. [15]. These actuators have been successful at eliminating the hysteresis associated with rotating stall and stabilizing the surge dynamics. One area which is problematic is the requirement of relatively high bandwidth actuators in order to control rotating stall using this actuation method.

Air injection has also proven successful at controlling rotating stall in experiments. Gysling's work [22] was based on using aeromechanical feedback for controlling a circumferential array of air injectors upstream of the rotor face. The aeromechanical feedback was based on the increased static pressure that is present in regions of the compressor annulus where rotating stall occurs. By clever valve design, this effect was used to inject air which damped out small amplitude flow perturbations at the compressor inlet which would have grown into rotating stall cells. This actuation scheme provided for a 10% decrease in the stalling mass flow rate through the compressor for the closed loop case, compared with the steady air injection case. Twenty-four valves where used to accomplish this control technique, and the mass flow addition was approximately 4% of the stalling mass flow rate.

Further work using air injection to control rotating stall was performed by Day [10]. His work focused on using several different techniques for damping out the flow perturbations which grow into rotating stall cells. Two methods were investigated, one which attempted to measure the rotating stall modes (using hot-wires) and cancel them, and a second which measured local flow perturbations and attempted to reject them individually. Both of these methods were successful at extending the operating region of the compressor system. Day also showed that this sort of rotating stall control has a beneficial effect of damping out surge oscillations.

D'Andrea et al. [9] showed that the effect of continuous air injection was to shift the steady state compressor performance characteristic and then explored the use of this for closed loop control. The result was a controller which eliminated the hysteresis region associated with rotating stall. Further work by the same authors [8] showed results for air injection control of rotating stall and surge that are similar to those of Day [10], even though the injected air flow was not axial in nature.

1.2.3 Identification

While the identification of parameters for both the MG–3 model and the higher fidelity distributed model has been an important task, it has not been addressed

systematically. Some of the parameters can be estimated from direct measurements on the compressor, but some are more problematic.

Part of the reason for this has been that the engine must normally be operated outside of the region where the models discussed so far are centered, i.e. a compressor would not normally be operated under conditions where it would transition to surge or rotating stall. The primary reason for this is that operating in regions where surge and rotating stall are present can damage the rig. Experimental data in these regions is however very important for developing simulations which accurately predict the system behavior, and the rig must be operated in this region for some period of time in order to develop accurate models.

There is also a fundamental difficulty in determining some of the parameters involved in the compressor models. This is primarily associated with gaining knowledge of the steady unstalled compressor performance map. This map describes the pressure rise delivered by the compressor for a given flow rate under steady conditions. The models require knowledge of this map in regions where the unstalled case is not a stable operating point.

The original presentation of the distributed model by Mansoux et al. [31] included the results from an identification of three separate compressors in use at MIT. The procedure for development of the compressor performance maps involved running simulations for the transition to rotating stall and comparing the results to experimental data. The simulation parameters were then iterated on until the simulation and the experimental data matched. This procedure can be quite successful, but is time consuming.

Other parameters involved in the models are estimated from physical considerations and then "adjusted" to match simulations with experimental data. A prime example of this is the values for the time constants associated with the unsteady loss dynamics. There has not been a systematic treatment of a proper way to identify all of the parameters.

1.3   Contributions of this Work

Part of the focus of this thesis is to develop a model which explains the air injection control strategy that has been developed through experiment on the Caltech rig. The MG–3 model is extended to include the effects of air injection and a dynamical systems style analysis is performed to determine how the closed loop system dynamics will be different from those of the open loop system. This low order model is then shown to capture qualitatively the effects seen in experiments and used to select parameters for the placement of the air injection actuators. A higher order model, based on the previously described distributed model of Mansoux et al. [31], is used to develop a quantitative match between the experiment and a simulation.

In addition to the modeling and simulation work, this thesis also presents further experimental results in the use of air injection for the control of rotating stall. The results include a geometric search for the optimal placement of the actuators, and experiments on combined air injection control of rotating stall with bleed valve control of surge.

1.3.1 Modeling and analysis

In this work, the MG–3 model is extended to include the effects of air injection. The air injection is included in two parts: a shift of the compressor steady state performance characteristic, and a more detailed model of the mass and momentum addition terms that the air injection actuator adds to the Moore and Greitzer PDE description. The compressor performance characteristic shifting is similar to the idea presented by Gysling [22]. The development of the mass and momentum terms is similar to the linear model presented by Hendricks and Gysling [24], although here a full nonlinear model is utilized.

For the shift effect, the closed loop, low order model is analyzed to determine the effects on the bifurcations which capture the transition to rotating stall. This is accomplished by comparison with the open loop bifurcation diagrams for the MG–3 model. From this analysis, optimal choices for how the air injection actuators should be implemented on the system are determined.

Additional analysis is performed to show the separation of surge controller design from the stall controller design. This allows the analysis for the air injection controller case to be combined with a simple linear throttle controller design for surge, and provides conditions for when this combination will be stable.

A higher order distributed model which includes the effects of air injection described above was then developed. This model was used to qualitatively match the compressor performance observed in experiments. Additional effects were also included such as the air injection actuator dynamics and system transport delays.

1.3.2 Experimental results

The experimental results which make up this work include both open and closed loop experiments. The experiments include results for control of rotating stall, surge, and the combination of these instabilities.

An open loop study of how air injection affects the compressor performance map with respect to rotating stall was performed; this involved two parametric studies of the geometric parameters associated with the upstream air injectors. The first study focuses on the positioning of the air injectors relative to the rotor. The span position in the compressor annulus where the injected air reaches the rotor is investigated, as well as the angle relative to the compressor axis at which the air is injected. In the second parametric study, the amount of injected air is varied in order to determine the minimum amount of injection required to achieve the decrease in stalling flow rate and the reduction in the size of the hysteresis loop. This study is of particular interest since the viability of air injection actuation on real gas turbine engines depends on using very low amounts of injected air.

The original closed loop experiments using pulsed air injection to control rotating stall on the Caltech rig were presented in [7, 8, 9] and represent joint work with R. D'Andrea. Further investigations of this control strategy are presented here. A control strategy for the elimination of the surge cycle oscillations using a bleed valve is investigated. This strategy was originally suggested by Eveker et al. [15]. In addition, closed loop experiments showing how a combined controller which uses this

bleed valve controller to stabilize the surge dynamics and an air injection controller for rotating stall performs are presented. The results show an improvement in the elimination of the surge limit cycle over the air injection controller alone, and the feasibility of combining control designs for each of the two compression system instabilities.

Detailed measurements of the behavior of the air injection actuators were performed in order to develop a model for use in simulations of the closed loop compressor/air injector system. Tests included the measurement of the dispersion pattern at the jet exit, and the results were used to calculate the mass/momentum/energy content of the injected air. The time delays (including the lags of the electronics driving the mechanical valves and the transport delay for the fluid) between command signals for opening of the injectors and the arrival of injected air at the rotor face were also measured.

1.3.3   Identification

A systematic procedure for using experimental measurements of the behavior of axial flow compressors to develop a distributed model representation is presented. This procedure was validated on the Caltech rig. Many of the rig's geometric parameters were initially determined by measurements on the rig and from details about the compressor itself. Further refinements were made by a series of dynamic measurements of compressor transients. The transients included fixed throttle measurements of surge cycles, step changes in the throttle position, and fixed throttle measurements of rotating stall cycles.

Expermental data taken over surge cycles was used to back out the compressor performance characteristic curve in regions were the rig cannot be operated in a steady condition. This technique provides a straightforward method for determining the compressor characteristic over a wide range of flow rates and also provides uncertainty values for the compressor performance map, which aid in the assessment of robustness for control techniques. This identification scheme also gives results for the system parameters when the rig is in its surge configuration. The transient data from step changes in the throttle position was used to determine parameters for the rig operating in the rotating stall configuration.

A final method of identifying the compressor performance map and testing one of the assumptions of the Moore and Greitzer model was performed. The local pressure rise and flow rate across the rotor was measured during rotating stall cycles. Previous testing on the Caltech rig had shown that the stall events occur on the rotor and that greater than 90% of the pressure rise delivered by compressor occurred here. When these two items are taken into account, the results between the surge transient identification scheme described above and this local scheme are in agreement. This local scheme also gives a method of directly measuring the importance of the unsteady loss dynamics terms, through the comparison of simulation and experimental data.

Finally, this identification technique was applied to the output from a distributed model simulation. The results of this study were used to determine the sensitivity

of the identification algorithm.

1.4 Outline of Thesis

Chapters 2 and 3 contain the basic modeling and analysis results contained in this thesis. Chapter 2 contains an introduction to the Moore and Greitzer PDE description of rotating stall and surge in axial flow compressors and its reduction to MG–3. The fluid mechanical modeling of the air injection actuators is also presented. This chapter also contains an overview of the bifurcation analysis that others have performed on MG–3 and a bifurcation analysis of one closed loop air injection system. Chapter 3 contains a description of the distributed model used to simulate the Caltech rig, including the unsteady loss dynamics.

Experimental results are presented in Chapters 4 and 5. Chapter 4 contains a description of the Caltech rig, including information on all of the main components used in experiments presented in later chapters. This chapter also includes measurements of the transition to rotating stall for the open loop compressor system, and the parametric study of the effects of continuous air injection on the compressor performance characteristic. Chapter 5 contains the experimental results for closed loop control of rotating stall using pulsed air injection. These results have previously been reported in [8], but the presentation here is more through. Additional experiments involving bleed valve control of surge and a combined surge (bleed valve)/rotating stall (air injection) controller are also included in this chapter.

The model identification and simulation results are presented in Chapters 6 and 7. Chapter 6 contains a description of the identification schemes used to develop parameters for the distributed model of the Caltech rig. The results of these identification schemes are used in simulating the distributed model presented in Chapter 3. Chapter 7 contains simulation studies that were performed using this distributed model. These studies include comparisons between simulation output and experimental data, and the closed loop simulation of the air injection controller.

Chapter 8 contains discussion, conclusions, and suggestions for future work in this research area.

Chapter 2

Low Order Modeling, Analysis and Control

The model which has had the most success in qualitatively capturing the dynamics of rotating stall and surge in axial flow compressors was developed by Moore and Greitzer and was first presented in final form in [35]. The model combines a PDE description of the flow field upstream of the rotor face and an ordinary differential equation (ODE) description of the overall pressure rise delivered by the compressor. The most common form of this model is a reduction of the PDE description to three coupled ODEs; this reduced model will be referred to here as MG-3. The reduction is accomplished by assuming a Fourier series for the solution of the PDE and then truncating the series at a single mode.

The full PDE description developed by Moore and Greitzer is presented here since it is required for the derivation of the air injection model, and because it will be used later in the presentation of the distributed model in Chapter 3. The basic assumptions and derivation of the model are reproduced here, although some of the details are left to the original work of Moore and Greitzer. The reduction of the PDE description to the to MG-3 model is also covered.

Analysis from a dynamical systems perspective on this three state model was first performed by McCaughan [32, 33]; similar analysis was performed by Abed et al. [1] on a slightly different model. In addition to the outline of the derivation, basic dynamical systems style nonlinear analysis of the MG-3 model is reproduced here so that it can be used for comparison with the bifurcation analysis of closed loop systems developed in this chapter.

For the air injection actuated case, based on the assumption that air injection results in a shift of the steady state compressor performance characteristic, the optimal form of the control input is obtained. In addition, the mass and momentum effects of air injection are derived and appended to the Moore and Greitzer PDE model. This derivation is based on the linear model originally developed by Gysling and Hendricks [24], but includes the nonlinear terms as well. Finally, the possibility of decoupling the design of surge and stall controllers for the MG-3 model is investigated. This chapter begins with begin with an overview of the steady state behavior of axial flow compression systems, and then proceeds to model development and analysis.
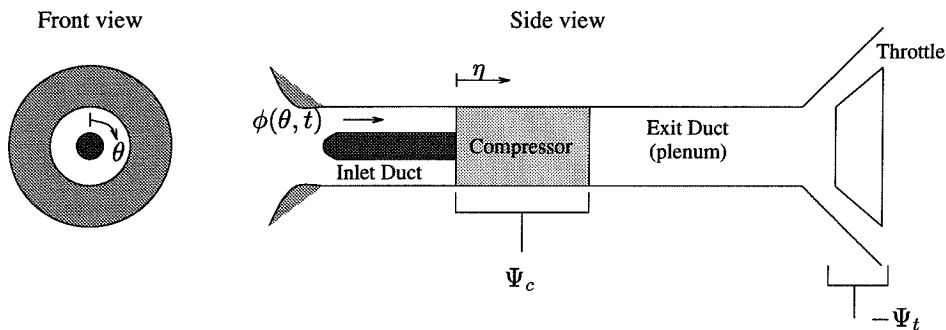
Figure 2.1 Schematic of compression system used for modeling.

2.1   Overview of Compression Systems

A schematic of a compression system is shown in Figure 2.1. The performance of a compressor is typically described by the steady state compressor characteristic, $\Psi_c(\Phi)$, which is a map that gives the pressure rise delivered by the compressor as a function of the flow rate through the compressor. Typically this map is a presented as a polynomial,

$$\Psi_c(\Phi) = a_0 + a_1\Phi + a_2\Phi^2 + a_3\Phi^3 + \cdots \tag{2.1}$$

where Φ is the annulus averaged non-dimensional flow coefficient[1] and the a_i are coefficients used to fit experimental data. In experiments, only the portion of the compressor characteristic with negative slope can be measured, since in the region with positive slope, rotating stall or surge (i.e. instability) occurs. These instabilities will be investigated further later in this chapter.

There is a similar relation for the pressure loss versus flow rate relation delivered by the downstream throttle. Typically this relation is quadratic and is of the form

$$\Psi_t(\Phi) = \frac{1}{\gamma^2}\Phi^2, \tag{2.2}$$

where $\Psi_t(\Phi)$ is the pressure drop across the throttle and γ is the throttle coefficient.

---

[1]As an aside, it should be noted that the flow rates and pressures given throughout this chapter and those to follow are nondimensionalized using the following relations:

$$\Phi = \frac{\dot{m}}{\rho U A_d} \qquad \Psi = \frac{\Delta P}{\rho U^2},$$

where $\dot{m}$ is the mass flow rate to be nondimensionalized, ρ is the density of air, U is the velocity of the rotor blades at the mean rotor radius, A_d is the area of the duct that the flow is traveling through, and ΔP is the pressure difference to be nondimensionalized. More information on the numerical values of the parameters used for the nondimensionalization can be found in Chapter 4. These nondimensional numbers make comparisons between different compressors easier, see for example the texts by Sabersky et al. [40] or Gerhart and Gross [16].
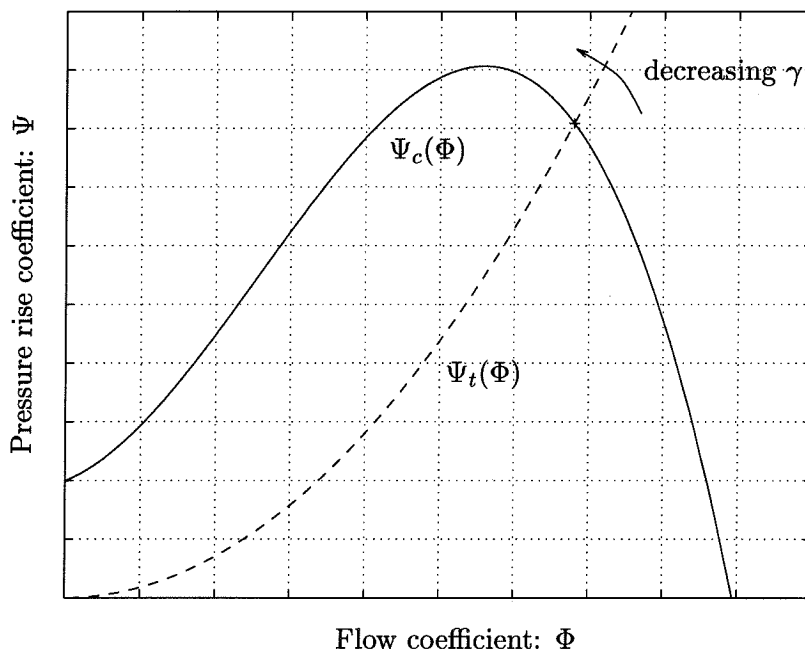
Figure 2.2 Compressor and throttle characteristics. The solid line is the compressor characteristic, $\Psi_c(\Phi)$, and the dashed line is the throttle characteristic, $\Psi_t(\Phi)$

The particular form for the constant in front of the quadratic Φ term has been selected to make the inverse of the relation shown in equation (2.2) (which will be required later) simpler. The physical amount of throttle opening dictates the value of γ; large γ implies a wide open throttle and small γ implies a closed throttle. The intersection of these two pressure delivery curves gives the steady state operating point for the compressor system, as is indicated by the + in Figure 2.2.

2.2 Moore–Greitzer Model

In this section the basic derivation of the Moore–Greitzer model for rotating stall and surge in axial flow compressors will be presented. The model consists of a system of equations which describe how the states of a compression system evolve in time. These states are the pressure rise delivered by the compressor, the flow rate through the compressor, and the amplitude of the rotating stall cell present at the rotor face. A reduction of this system of equations to the MG–3 model is also presented.

2.2.1 Description and assumptions

The model developed by Moore and Greitzer [35] for axial flow compression systems is based on three assumptions. In the description of the model here, each of these basic assumptions will be presented, and then the details of how each comes about will be provided. The presentation here follows the treatment by Mansoux et al. [31], but also draws on results from the original work by Moore and Greitzer [35].

Figure 2.1 shows a schematic of an axial flow compression system for which the Moore and Greitzer PDE was developed. The flow enters from atmospheric pressure at the inlet duct at the left of the figure, proceeds through the compressor block where the static pressure is increased, enters the outlet duct, and then exits to atmospheric pressure through the downstream throttle.

The three basic assumption of the Moore and Greitzer compression system model are:

1. The pressure rise across the compressor lags behind the pressure drop delivered by the throttle due to mass storage in the exit duct (or plenum).

2. Across the compressor, the difference between the pressure delivered by the compressor and pressure rise that currently exists across the compressor acts to accelerate the flow rate through the compressor.

3. The flow in the inlet is given by the solution to Laplace's equation.

The first assumption gives the relationship

$$\frac{\partial \Psi(\xi)}{\partial \xi} = \frac{1}{4l_c B^2} \left(\Phi(\xi) - \gamma \sqrt{\Psi(\xi)} \right), \tag{2.3}$$

where ξ is the nondimensional time in rotor radians, l_c is the effective duct length of the compressor, B is the Greitzer surge parameter, Φ is the annulus averaged flow coefficient, γ is the throttle coefficient, and Ψ is the pressure rise coefficient which is given by

$$\Psi(\xi) = \frac{P_e(\xi) - P_{t_i}(\xi)}{\rho U^2}. \tag{2.4}$$

The second assumption leads to the following relationship for the dynamics of the flow through the compressor:

$$\frac{p_e(\theta, \xi) - p_{t_i}(\theta, \xi)}{\rho U^2} = \Psi_c(\phi(\theta, \xi)) - (l_i + l_e)\frac{d\Phi(\xi)}{d\xi} -$$
$$\lambda \frac{\partial \phi(\theta, \xi)}{\partial \theta} - \mu \frac{\partial \phi(\theta, \xi)}{\partial \xi} \qquad \eta = 0, \tag{2.5}$$

where λ represents the fluid inertia in the rotor, μ represents the fluid inertia in the compressor, ϕ is the local flow coefficient in the compressor annulus, l_i and l_e are the effective nondimensional inlet and exit duct lengths, θ is the circumferential position around the compressor annulus, p_e is the static pressure downstream of the

compressor, η is the nondimensional axial position in the duct ($\eta = 0$ corresponds to the rotor face), and p_{t_i} is the total pressure at the compressor inlet. Note that each of the quantities in equation (2.5) are functions of the circumferential position θ and the nondimensional time ξ (i.e. $\phi = \phi(\theta, \xi)$, etc.), and therefore equation (2.5) holds locally around the compressor annulus at each instant in time.

In order to simplify the equations, the equation states are broken into annulus averaged and circumferential perturbation components. This gives rise to the change of coordinates

$$
\begin{aligned}
\phi(\theta, \xi) &= \Phi(\xi) + \delta\phi(\theta, \xi) \\
p_e(\theta, \xi) &= P_e(\xi) + \delta p_e(\theta, \xi) \\
p_{t_i}(\theta, \xi) &= P_{t_i}(\xi) + \delta p_{t_i}(\theta, \xi),
\end{aligned}
\tag{2.6}
$$

where the uppercase quantities are annulus averaged quantities, i.e.

$$
\Phi(\xi) = \int_0^{2\pi} \phi(\theta, \xi) d\theta,
\tag{2.7}
$$

and δ indicates a perturbation quantity, i.e. $\delta\phi$ is the perturbation of the flow coefficient. The axisymmetric part of equation (2.5) is given by

$$
\frac{\partial \Phi(\xi)}{\partial \xi} = \frac{1}{l_c} \left(\int_0^{2\pi} \Psi_c(\Phi(\xi) + \delta\phi(\theta, \xi)) d\theta - \Psi(\xi) \right) \qquad \eta = 0,
\tag{2.8}
$$

where the effective compressor duct length l_c is given by

$$
l_c = l_i + l_e + \mu
\tag{2.9}
$$

and the pressure rise coefficient Ψ is as was previously given in equation (2.4). Note that from this point on, the explicit dependencies of variables on θ and ξ should be clear from context, and will not be shown. The non-axisymmetric part of equation (2.5) is given by

$$
\frac{\delta p_e - \delta p_{t_i}}{\rho U^2} = \Psi_c(\Phi + \delta\phi) - \int_0^{2\pi} \Psi_c(\Phi + \delta\phi) d\theta - \lambda \frac{\partial(\delta\phi)}{\partial \theta} - \mu \frac{\partial(\delta\phi)}{\partial \xi}.
\tag{2.10}
$$

The potential flow assumption gives the functional form for the flow perturbations in the upstream duct, based on the solution of Laplace's equation. This suggests the following perturbation velocity potential $\delta\Theta$ which is defined as

$$
\frac{\partial(\delta\Theta)}{\partial \eta} = \delta\phi.
\tag{2.11}
$$

Laplace's equation in the inlet duct is then given by

$$
\nabla^2 \delta\Theta = 0 \qquad \eta \leq 0,
\tag{2.12}
$$

which has the solution

$$\delta\Theta(\theta, \eta, \xi) = \sum_{n=1}^{\infty} \frac{e^{n\eta}}{n} A_n(\xi) \sin\left(n\theta + r_n(\xi)\right), \tag{2.13}$$

where A_n is the amplitude of the nth circumferential Fourier mode and r_n is its phase. Combining equations (2.11) and (2.13) gives the perturbation of the flow coefficient as

$$\delta\phi(\theta, \xi) = \sum_{n=1}^{\infty} A_n(\xi) \sin\left(n\theta + r_n(\xi)\right) \qquad \eta = 0. \tag{2.14}$$

Note that the solution for the flow perturbation $\delta\phi(\theta, \xi)$ is evaluted at the rotor face. Based on this potential flow solution, the downstream static and upstream total pressures are given by

$$\frac{\delta p_e}{\rho U^2} = \frac{\partial(\delta\Theta)}{\partial\xi} \qquad \frac{\delta p_{t_i}}{\rho U^2} = -\frac{\partial(\delta\Theta)}{\partial\xi} \tag{2.15}$$

(see Epstein et al. [14]). Combining equations (2.10) and (2.15) gives the following relation for non-axisymmetric unsteady behavior in the compressor annulus,

$$2\frac{\partial(\delta\Theta)}{\partial\xi} + \lambda\frac{\partial(\delta\phi)}{\partial\theta} + \mu\frac{\partial(\delta\phi)}{\partial\xi} = \Psi_c(\Phi + \delta\phi) - \int_0^{2\pi} \Psi_c(\Phi + \delta\phi)d\theta. \tag{2.16}$$

The system of equations describing the behavior of an axial flow compression system are therefore given by

$$\frac{\partial\Psi}{\partial\xi} = \frac{1}{4l_c B^2}\left(\Phi - \gamma\sqrt{\Psi}\right)$$

$$\frac{\partial\Phi}{\partial\xi} = \frac{1}{l_c}\left(\int_0^{2\pi} \Psi_c(\Phi + \delta\phi)d\theta - \Psi\right) \qquad \eta = 0$$

$$2\frac{\partial(\delta\Theta)}{\partial\xi} + \lambda\frac{\partial(\delta\phi)}{\partial\theta} + \mu\frac{\partial(\delta\phi)}{\partial\xi} = \Psi_c(\Phi + \delta\phi) - \int_0^{2\pi} \Psi_c(\Phi + \delta\phi)d\theta \qquad \eta = 0. \tag{2.17}$$

2.2.2 Reduction to MG–3

In order to further simplify the above equations to a low order model which could be readily analyzed, Moore and Greitzer [35] explored the first term in the Fourier series for the flow perturbation $\delta\phi$. By truncating the Fourier series for the potential flow solution given in equations (2.13) and (2.14) and combining equations (2.3), (2.8), and (2.16), they were able to obtain the following four ODEs are obtained for the

compression system dynamics

$$\frac{d\Psi}{d\xi} = \frac{1}{4l_c B^2}\left(\Phi - \gamma\sqrt{\Psi}\right)$$

$$\frac{d\Phi}{d\xi} = \frac{1}{l_c}\left(\int_0^{2\pi}\Psi_c(\Phi + A_1\sin\zeta)d\zeta - \Psi\right)$$

$$\frac{dA_1}{d\xi} = \frac{1}{\pi(2+\mu)}\int_0^{2\pi}\Psi_c(\Phi + A_1\sin\zeta)\sin\zeta\, d\zeta$$

$$\frac{dr_1}{d\xi} = \frac{-\lambda}{2+\mu}. \tag{2.18}$$

For more details on this reduction procedure, see the original work by Moore and Greitzer [35]. Note that the $(dr_1)/(d\xi)$ equation shows that the stall cell will rotate at a constant rate, and since r_1 doesn't appear in the other three equations, this fourth equation is often left out of the analysis of the MG–3 model.

2.2.3 Bifurcation analysis

By performing the integrals indicated in the system of equations (2.18), substituting $J_1 = A_1^2$, and assuming a third order polynomial expansion for the compressor performance characteristic $\Psi_c(\Phi)$ i.e.

$$\Psi_c(\Phi) = a_0 + a_1\Phi + a_2\Phi^2 + a_3\Phi^3, \tag{2.19}$$

we obtain the following set of ODEs which describe the dynamics of the compression system:

$$\dot{\Psi} = \frac{1}{4l_c B^2}\left(\Phi - \gamma\sqrt{\Psi}\right) \tag{2.20}$$

$$\dot{\Phi} = \frac{1}{l_c}\left(\Psi_c(\Phi) - \Psi + \frac{J_1}{4}\frac{\partial^2\Psi_c}{\partial\Phi^2}\right) \tag{2.21}$$

$$\dot{J}_1 = \frac{2}{\mu+2}J_1\left(\frac{\partial\Psi_c}{\partial\Phi} + \frac{J_1}{8}\frac{\partial^3\Psi_c}{\partial\Phi^3}\right), \tag{2.22}$$

where ($\dot{\ }$) denotes differentiation of ( ) with respect to ξ. Equation (2.22) clearly shows that the compressor characteristic, $\Psi_c(\Phi)$, must contain terms of at least third order to capture a stalled equilibrium point.

The bifurcation properties of the open loop three state compression system model were initially studied by McCaughan in [32] and [33]. There the bifurcations for the pure rotating stall case, the pure surge case, and combination stall/surge case were thoroughly investigated. A throttle based closed loop system for the pure rotating stall case was developed and analyzed by Liaw and Abed in [30].

Here we are interested only in the pure rotating stall case for the closed loop compression system with the control based on shifting of the steady state compressor characteristic. For the open loop case, the bifurcation diagram for a representative
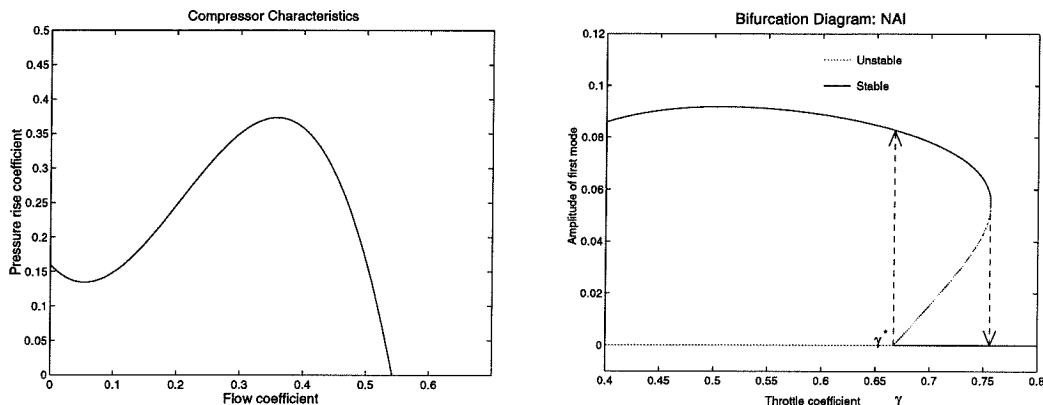
Figure 2.3 Bifurcation diagram showing jumps associated with the hysteresis loop for an open loop compression system with the characteristic shown at the left (pure rotating stall case).

compressor characteristic is known to have a transcritical bifurcation[2] (for the choice of coordinates used in this paper) at the point which corresponds to operating at the peak of the steady state compressor characteristic (see Figure 2.3). The throttle setting which corresponds to the peak of the characteristic, $(\partial\Psi_c/\partial\Phi) = 0$, will be denoted by γ^*. This operating point corresponds to where the stalled branch intersects the horizontal axis in the bifurcation diagram shown in Figure 2.3.

The unstable sections of the bifurcation diagram in Figure 2.3 are shown as grey lines, and the stable sections are shown as black lines. This diagram suggests a hysteresis region since as the throttle is closed (γ is decreased) $J_1 = 0$ is a stable solution until γ^* is reached, at which point the stable solution for J_1 is non-zero (which corresponds to a jump to rotating stall). As γ continues to decrease, the stable solution for J_1 continues to be non-zero. If the throttle is then opened, beginning at $\gamma < \gamma^*$, the system continues to evolve along the stalled branch until γ is increased to a value substantially greater than γ^* before returning to the $J_1 = 0$ branch. The system has substantially different solutions depending on the path that γ follows.

When the compressor system is not in a stalled condition, equation (2.21) reduces to

$$\dot{\Phi} = \frac{1}{l_c}\left(\Psi_c(\Phi) - \Psi\right). \tag{2.23}$$

Similarly, when the system is in a stalled condition, equation (2.21) can be written as

$$\dot{\Phi} = \frac{1}{l_c}\left(\Psi_{c_{stall}}(\Phi) - \Psi\right) \qquad \Psi_{c_{stall}} = \Psi_c - 2\frac{\frac{\partial\Psi_c}{\partial\Phi}}{\frac{\partial^3\Psi_c}{\partial\Phi^3}}\frac{\partial^2\Psi_c}{\partial\Phi^2} \tag{2.24}$$

---

[2]For more information on bifurcation analysis see the text by Guckenheimer and Holmes [21] or the text by Wiggins [43].
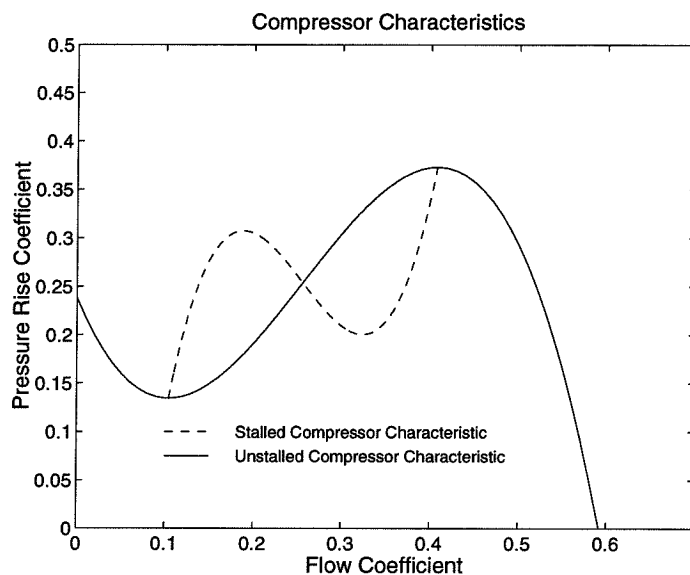
Figure 2.4 Unstalled (solid) and stalled (dashed) compressor characteristics.

by using the nonzero equilibrium solution for J_1 from equation (2.22). This *stalled* (or effective) compressor characteristic is important because this is the pressure rise that the MG–3 model predicts would be measured experimentally when the system is stalled and therefore gives one validation test for this model. Figure 2.4 shows a plot of $\Psi_c(\Phi)$ (solid curve) and $\Psi_{c_{stall}}(\Phi)$ (dashed curve). The stalled compressor characteristic will important for the parameter identification methods addressed in Chapter 6. Note that the stability of these curves of equilibria are not shown. For a more detailed description of the bifurcations associated with the MG–3 model see the work by McCaughan [32] and [33].

2.3 Moore–Greitzer Model with Air Injection

There are two primary effects caused by adding air injection actuators to an axial flow compression system: a shift in the steady state compressor performance characteristic and momentum addition effects. The shift effect is addressed first in this section.

The physical basis for adding air injection into the model as a shift to the steady state compressor characteristic is based on the experimental results presented by D'Andrea et al. [9], where air injection actuators substantially shifted the compressor performance characteristic. The idea that an actuator could effect the pressure rise delivered by the compressor was proposed by Gysling [22]. On the Caltech rig, the shift is used primarily to model the swirl (angular momentum) added by the air injection actuators.

In addition to the swirl component, air injection also adds mass and momentum

to the compressor inlet, these effects are addressed in the final subsection. These effects complicate the model to a greater extent and will require further derivation along the lines of Section 2.2.

2.3.1 Compressor characteristic shift effects

The results presented in this subsection are based on the Moore–Greitzer model [35] presented in Section 2.2. Here we present one method for changing the hysteresis behavior of the compression system by selecting a control input which directly changes the bifurcation diagram in the hysteresis region.

Optimal compressor characteristic shift

Based on the experimental results described in [9] we attempt to model the air injection actuators as direct actuators of the steady state compressor characteristic. In this paper we analyze the results of the closed loop system where the feedback is proportional to the size of the first mode of the stall cell squared:

$$\Psi_c = \Psi_{c_{nom}} + K J_1 \Psi_{c_u} \qquad (2.25)$$

where

$$\Psi_{c_{nom}} = a_0 + a_1\Phi + a_2\Phi^2 + a_3\Phi^3 \qquad \Psi_{c_u} = c_0 + c_1\Phi. \qquad (2.26)$$

A shifting of the steady state compressor characteristic curve proportional to J_1 can accomplish this. To see how, we first solve for the slope of the bifurcation curve at the point γ^*. On the stalled branch of the bifurcation diagram, the following algebraic equations must hold

$$\Phi^2 = \gamma^2\Psi, \qquad (2.27)$$

$$\Psi_c = \Psi - \frac{J_1}{4}\frac{\partial^2\Psi_c}{\partial\Phi^2}, \qquad (2.28)$$

and

$$\frac{\partial\Psi_c}{\partial\Phi} = -\frac{J_1}{8}\frac{\partial^3\Psi_c}{\partial\Phi^3}. \qquad (2.29)$$

Noting that, for each equilibrium solution on the stalled branch of the bifurcation diagram, choosing J_1 fixes Φ, Ψ, and γ, and by differentiating equation (2.27) with respect to J_1 we obtain

$$2\Phi\frac{d\Phi}{dJ_1} = 2\gamma\Psi\frac{d\gamma}{dJ_1} + \gamma^2\frac{d\Psi}{dJ_1}. \qquad (2.30)$$

By differentiating equation (2.28) with respect to J_1, an expression for $\frac{d\Psi}{dJ_1}$ at the peak of the compressor characteristic is found to be

$$\frac{d\Psi}{dJ_1}\bigg|_{\gamma=\gamma^*} = K\Psi_{c_u} + \frac{1}{4}\frac{\partial^2\Psi_{c_{nom}}}{\partial\Phi^2}. \tag{2.31}$$

By similar differentiation of equation (2.29) with respect to J_1, an expression for $(d\Phi/dJ_1)$ at the same point is found to be

$$\frac{d\Phi}{dJ_1}\bigg|_{\gamma=\gamma^*} = \frac{K\frac{\partial\Psi_{c_u}}{\partial\Phi} + \frac{1}{8}\frac{\partial^3\Psi_{c_{nom}}}{\partial\Phi^3}}{-\frac{\partial^2\Psi_{c_{nom}}}{\partial\Phi^2}}. \tag{2.32}$$

If equations (2.31) and (2.32) are substituted into equation (2.30) and the result solved for $(dJ_1/d\gamma)$, the slope of the bifurcation diagram at the equilibrium point associated with γ^* is obtained as:

$$\frac{dJ_1}{d\gamma}\bigg|_{\gamma=\gamma^*} = \frac{\sqrt{\Psi}}{\frac{K\Psi'_{c_u}+\frac{1}{8}\Psi'''_{c_{nom}}}{-\Psi''_{c_{nom}}} - \frac{\Phi}{2\Psi}\left(K\Psi_{c_u} + \frac{1}{4}\Psi''_{c_{nom}}\right)}, \tag{2.33}$$

where all expressions in the right hand side of equation (2.33) are evaluated at the equilibrium point at the peak of the compressor characteristic, and ( )$'$ denotes partial differentiation of ( ) with respect to Φ.

From this expression it is easy to see how varying the gain on the shifted characteristic affects the slope of the bifurcation diagram at γ^*. Typically, $(dJ_1/d\gamma)|_{\gamma=\gamma^*}$ is positive (as is shown in the bifurcation diagram in Figure 2.3) and if this positive value were increased, the size of the hysteresis region could be decreased. If the shifted portion of the characteristic, Ψ_{c_u}, has a positive offset term ($c_0 > 0$) the slope will be increased by a positive gain K, and if the shifted characteristic has a negative linear term ($c_1 < 0$) the slope will also be increased for a positive gain K. In Chapter 5 experiments will be presented which validate this modeling technique for axisymmetric shifts of the compressor performance characteristic.

Figure 2.5 shows how the bifurcation diagram changes as the gain K is increased for the Caltech rig. This same sort of analysis can also be used to show how the hysteresis loop in the bifurcation diagram cannot be changed with nonlinear feedback of Ψ or Φ via throttle control. This result was shown previously, using a different method, by Liaw and Abed [30].

The above analysis applies to any physical mechanism which can be used to change the compressor performance characteristic. Some possible other possible methods of achieving a shift in the compressor characteristic include active casing treatments and hub distortion. The optimal choice of shift would be as described, and equation (2.33) would show the tradeoff of varying the slope versus the offset.
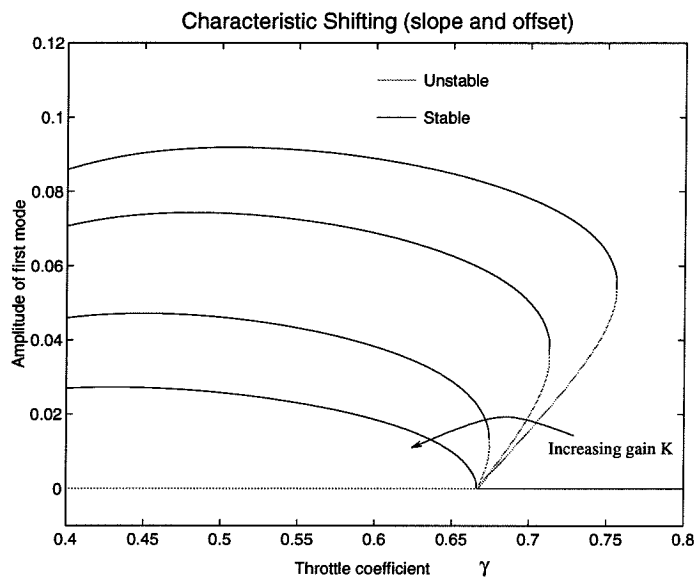
Figure 2.5 Closed loop bifurcation diagram as K is varied for the Caltech compressor. The top curve corresponds to $K = 0$.

Effects of saturation

The entire family of bifurcation diagrams shown in Figure 2.5 may not be physically possible in practice; there will be a maximum amount that the steady state compressor characteristic can be shifted. The plot on the left of Figure 2.6 shows the maximal amount that the characteristic can be shifted for the actuators installed on the Caltech compressor (as a dashed line). This saturation of the actuators translates to direct limit on how much the closed loop bifurcation diagram can be modified. On the right of Figure 2.6 the dashed line shows the saturation limit (the dashed line) for the compressor characteristic obtained with continuous air injection. Shifts which lie to the right of the saturation line are allowed, and for shifts which lie to the left, the saturation line becomes the curve that describes the system behavior.

Based on the previous analysis, the amount of characteristic shifting required to eliminate the rotating stall hysteresis loop would be the amount which equation (2.33) is infinite. In practice this calculation is very conservative. In most applications, noise will drive the compressor into rotating stall at a value of γ which is substantially greater than γ^*. This throttle position will therefore dictate the amount that the characteristic must be shifted to eliminate the hysteresis loop.

2.3.2 Mass and momentum addition effects

To complete the model for the effects of air injection actuation, the fluid mechanics of the original Moore–Greitzer model need to be augmented to include the mass and momentum addition of the air injectors. This was previously done in a linear context
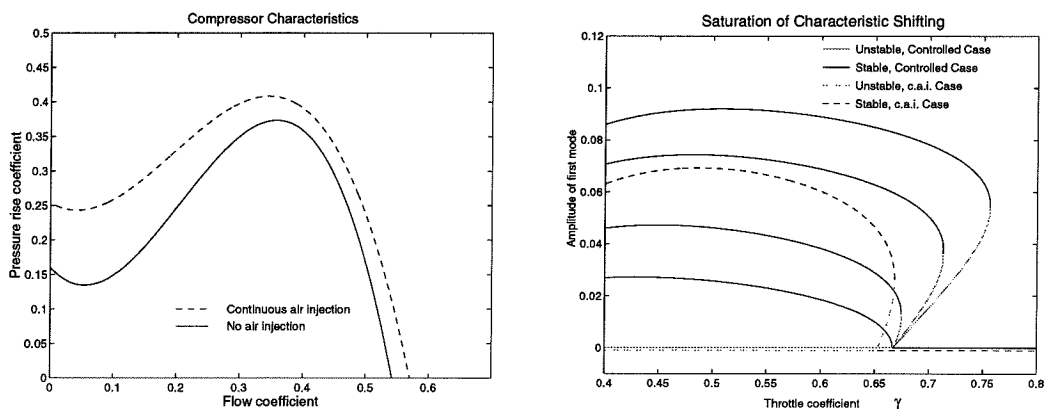
Figure 2.6 Bifurcation diagram showing the saturation limits of the Caltech rig (dashed line).
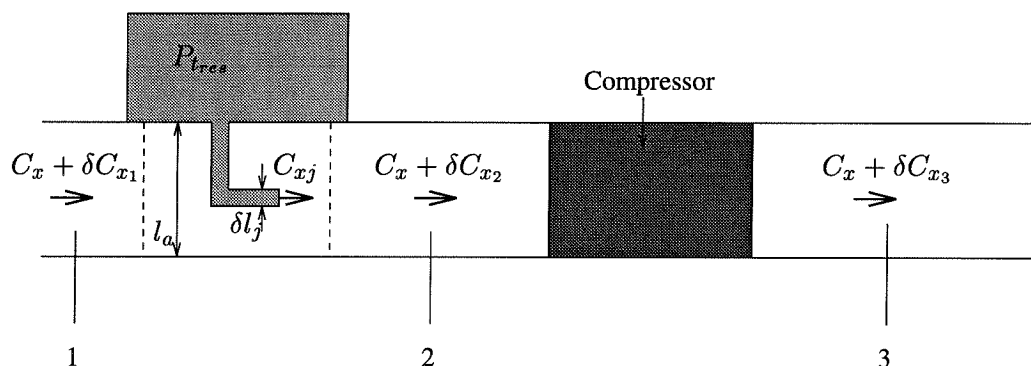
Figure 2.7 Air injection actuator upstream of the compressor rotor developed by Hendricks and Gysling [24].

by Hendricks and Gysling [24]. The derivation presented there is followed here but is extended to include the nonlinear effects of the air injection. The equations are developed by performing mass and momentum balances across the air injection actuator and combining the resulting equation with the original Moore and Greitzer PDE for the flow through the compressor.

Figure 2.7 shows a schematic for the air injection actuator upstream of the compressor, and includes the quantities that will be needed to develop the model.

In Section 2.2.1, equation (2.5) was presented. This equation can be re-written in the notation of Figure 2.7 as

$$\frac{p_3 - p_{t2}}{\rho U^2} = \Psi_c(\Phi + \delta\phi_2) - l_c\frac{d\Phi}{d\xi} - \lambda\frac{\partial\phi_2}{\partial\theta} - \mu\frac{\partial\phi_2}{\partial\xi}. \tag{2.34}$$

In order to develop a model of the combined air injection/compressor system, the relationship between the total pressure at station 1 (just upstream of the air injector)

and station 2 (just downstream of the air injector) must be developed. Then the air injection/compressor system can be combined with a potential flow solution in the inlet duct, as was done previously for the isolated compressor.

In order to develop the relationship between the total pressures at stations 1 and 2 two additional equations must be developed, a mass and a momentum balance across the air injector. The mass balance across the air injector is given by

$$\rho l_a (C_x + \delta C_{x_1}) + \rho \delta l_j C_{x_j} = \rho l_a (C_x + \delta C_{x_2}), \qquad (2.35)$$

where C_x is the mean velocity in the annulus, δC_{x_1} and δC_{x_2} are the velocity perturbations at stations 1 and 2, l_a is the height of the compressor annulus, and δl_j is the opening of the air injector. This equation reduces to

$$\delta \phi_2 = \delta \phi_1 + \frac{\delta l_j}{l_a} \Phi_j, \qquad (2.36)$$

where $\delta \phi_1$ and $\delta \phi_2$ are the nondimensional flow perturbations respectively upstream and downstream of the air injector. The momentum balance across the air injector is given by

$$l_a (P + \delta p_1) + \rho l_a (C_x + \delta C_{x_1})^2 + \rho \delta l_j C_{x_j}^2 = l_a (P + \delta p_2) +$$
$$\rho l_a (C_x + \delta C_{x_2})^2, \qquad (2.37)$$

where P is the static pressure in the annulus, and δp_1 and δp_2 are the static pressure perturbations at stations 1 and 2. Equation (2.37) can be combined with equation (2.36) and the relationship between the static and total pressure perturbations at station 1 given by

$$\frac{\delta p_{t_1}}{\rho U^2} = \frac{\delta p_1}{\rho U^2} + \Phi \delta \phi_1 + \frac{1}{2} \delta \phi_1^2, \qquad (2.38)$$

to obtain

$$\frac{\delta p_{t_2}}{\rho U^2} = \frac{\delta p_{t_1}}{\rho U^2} + (\Phi_j - \Phi - \delta \phi_1) \frac{\delta l_j}{l_a} \Phi_j - \frac{1}{2} \left(\frac{\delta l_j}{l_a} \Phi_j \right)^2. \qquad (2.39)$$

Combining equations (2.34) and (2.39) we obtain the following expression for the air injection/compressor system

$$\frac{p_3 - p_{t_1}}{\rho U^2} = \Psi_c (\Phi + \delta \phi_1 + \frac{\delta l_j}{l_a} \Phi_j) - l_c \frac{d\Phi}{d\xi} - \lambda \frac{\partial \phi_1}{\partial \theta} - \mu \frac{\partial \phi_1}{\partial \xi} +$$
$$(\Phi_j - \Phi - \delta \phi_1) \frac{\delta l_j}{l_a} \Phi_j - \frac{1}{2} \left(\frac{\delta l_j}{l_a} \Phi_j \right)^2. \qquad (2.40)$$

This equation can be combined with the relations similar to those given in equation (2.15) for the total and static pressure based on a potential flow solution in the

inlet duct to obtain

$$\left[\left(\frac{2}{n}+\mu\right)\frac{\partial}{\partial\xi}+\lambda\frac{\partial}{\partial\theta}\right]\left(\delta\phi_1+\frac{\delta l_j}{l_a}\Phi_j\right) = \Psi_c(\Phi+\delta\phi_1+\frac{\delta l_j}{l_a}\Phi_j)-\Psi-$$

$$l_c\frac{d\Phi}{d\xi}+(\Phi_j-\Phi-\delta\phi_1)\frac{\delta l_j}{l_a}\Phi_j-\frac{1}{2}\left(\frac{\delta l_j}{l_a}\Phi_j\right)^2. \quad (2.41)$$

The control input to this system is the opening of the air injector δl_j. Equation (2.41) shows if $\frac{\delta l_j}{l_a}\Phi_j \ll \delta\phi_1$, then the effect of the mass and momentum terms is to create an effective compressor characteristic, $\Psi_{c_{ai}}$, given by

$$\Psi_{c_{ai}} = \Psi_c(\Phi+\delta\phi_1+\frac{\delta l_j}{l_a}\Phi_j)+(\Phi_j-\Phi-\delta\phi_1)\frac{\delta l_j}{l_a}\Phi_j-\frac{1}{2}\left(\frac{\delta l_j}{l_a}\Phi_j\right)^2. \quad (2.42)$$

The shift of the compressor characteristic has already been investigated in the previous section, and analysis of this shift would be similar. In order to perform the analysis, a control law for the input δl_j would need to be selected (similar to what was done for the linear case by Hendricks and Gysling [24] where δl_j was selected a phase shifted and scaled version of $\delta\phi_1$), and then the effective compressor characteristic would be projected onto the Fourier bases as was done in Section 2.2.3.

2.4   Control in the Presence of Surge

The decoupling of designs for rotating stall and surge controllers can be approached from a singular perturbations standpoint. The first step is to find a time scale which separates the fast and slow manifolds of the system. This can be accomplished for the MG–3 model by choosing $\xi = l_c\tilde{\xi}$, which gives the new system

$$\frac{d\Psi}{d\tilde{\xi}} = \frac{1}{4B^2}\left(\Phi-\gamma\sqrt{\Psi}\right), \quad (2.43)$$

$$\frac{d\Phi}{d\tilde{\xi}} = \left(\Psi_c-\Psi+\frac{J_1}{4}\frac{\partial^2\Psi_c}{\partial\Phi^2}\right), \quad (2.44)$$

and

$$\frac{1}{l_c}\frac{dJ_1}{d\tilde{\xi}} = \frac{2}{\mu+2}J_1\left(\frac{\partial\Psi_c}{\partial\Phi}+\frac{J_1}{8}\frac{\partial^3\Psi_c}{\partial\Phi^3}\right). \quad (2.45)$$

For the Caltech compressor, $l_c \approx 30$, so $\frac{1}{l_c}$ is reasonably small. The perturbation parameter, ϵ, is therefore given by $\frac{1}{l_c}$. In addition, it is convenient if the origin is an equilibrium point; choosing $\Psi = \tilde{\Psi}+\Psi_e$ and $\Phi = \tilde{\Phi}+\Phi_e$ accomplishes this if Ψ_e and Φ_e are the intersection point of the compressor and the throttle characteristics.

The equations are then:

$$\frac{d\tilde{\Psi}}{d\tilde{\xi}} = \frac{1}{4B^2}\left(\tilde{\Phi} + \Phi_e - \gamma\sqrt{\tilde{\Psi} + \Psi_e}\right),\tag{2.46}$$

$$\frac{d\tilde{\Phi}}{d\tilde{\xi}} = \left(\Psi_c(\tilde{\Phi} + \Phi_e) - \tilde{\Psi} - \Psi_e + \frac{J_1}{4}\frac{\partial^2\Psi_c}{\partial\Phi^2}\right),\tag{2.47}$$

and

$$\frac{1}{l_c}\frac{dJ_1}{d\tilde{\xi}} = \frac{2}{2+\mu}J_1\left(\frac{\partial\Psi_c}{\partial\Phi} + \frac{J_1}{8}\frac{\partial^3\Psi_c}{\partial\Phi^3}\right).\tag{2.48}$$

In order to decouple the design process, a controller must be found which exponentially stabilizes the slow manifold (the surge dynamics). This can be accomplished by a throttle controller as was previously shown experimentally by Eveker et al. [15]. The fast hysteresis associated with the fast dynamics can be eliminated with the shifting compressor characteristic controller previously described. The combination of these two controllers is investigated below.

The form of the throttle controller for the surge dynamics that was the same as that specified by Eveker et al. [15] and is given by

$$\gamma = \gamma_0 + k_1\dot{\Phi}.\tag{2.49}$$

This controller intuitively adds damping to the system for a negative gain k_1. The control law would then open the throttle when the flow through the compressor is decreasing (acting to increase the flow rate) and close the throttle when the flow through the compressor is increasing (acting to decrease the flow rate).

In order to control the rotating stall dynamics the previously described shifting compressor characteristic controller is included as

$$\Psi_c = \Psi_{c_{nom}} + k_2 J_1 \Psi_{c_u},\tag{2.50}$$

where

$$\Psi_{c_{nom}}(\Phi) = a_0 + a_1\Phi + a_2\Phi^2 + a_3\Phi^3\tag{2.51}$$

$$\Psi_{c_u}(\Phi) = c_0 + c_1\Phi.\tag{2.52}$$

To apply the method of singular perturbations, we first make the origin an equilibrium point for equation (2.48) by choosing $J_1 = \tilde{J}_1 + J_{1e}$. The resulting equation for the growth of the rotating stall amplitude (the fast system) is

$$\epsilon\frac{d\tilde{J}_1}{d\tilde{\xi}} = \frac{2}{2+\mu}(\tilde{J}_1 + J_{1e})\left(\frac{\partial\Psi_c}{\partial\Phi} + k_2(\tilde{J}_1 + J_{1e})\frac{\partial\Psi_{c_u}}{\partial\Phi} + \frac{\tilde{J}_1 + J_{1e}}{8}\frac{\partial^3\Psi_c}{\partial\Phi^3}\right),\tag{2.53}$$

which has an has two branches of equilibria at

$$J_{1e} = 0, \tag{2.54}$$

and

$$J_{1e} = \frac{-8\frac{\partial \Psi_c}{\partial \Phi}}{\frac{\partial^3 \Psi_c}{\partial \Phi^3} + 8k_2 \frac{\partial \Psi_{c_u}}{\partial \Phi}} \tag{2.55}$$

which depend on the value of the throttle coefficient, γ_0. It should be noted that γ_0 sets the value of Φ_e, and the value of Φ_e dictates the behavior of the fast system.

The slow system is the combination of equations (2.46), (2.47), (2.49), and (2.50) and is given by

$$\frac{d\tilde{\Psi}}{d\tilde{\xi}} = \frac{1}{4B^2} \left(\tilde{\Phi} + \Phi_e - \left[\gamma_0 + k_1 \left(\Psi_c + k_2(\tilde{J}_1 + J_{1e})\Psi_{c_u} - \tilde{\Psi} - \Psi_e + \right. \right. \right.$$
$$\left. \left. \left. \frac{\tilde{J}_1 + J_{1e}}{4} \frac{\partial^2 \Psi_c}{\partial \Phi^2} \right) \right] \sqrt{\tilde{\Psi} + \Psi_e} \right) \tag{2.56}$$

$$\frac{d\tilde{\Phi}}{d\tilde{\xi}} = \left(\Psi_c + k_2(\tilde{J}_1 + J_{1e})\Psi_{c_u} - \tilde{\Psi} - \Psi_e + \frac{\tilde{J}_1 + J_{1e}}{4} \frac{\partial^2 \Psi_c}{\partial \Phi^2} \right). \tag{2.57}$$

The analysis of Section 2.3.1 showed that for large enough gain on the shifting compressor characteristic (i.e. k_2 in equation (2.50)) the entire stalled branch of equilibria can be made to be stable (note that the entire branch may already be stable for a given $\Psi_c(\Phi)$). A schematic of a stable branch of stalled equilibria, J_{1e}, as a function of the throttle coefficient, γ_0 is shown in Figure 2.8. For the gain shown in the figure there is a unique stable equilibrium value of the stall cell amplitude for a given value of γ_0. The stable branches in the figure refer to the stall dynamics being stable. Since we have not introduced the throttle controller for surge, it is still possible that the slow system may be unstable for some throttle settings.

The stability of the combined system, equations (2.53), (2.56), and (2.57), can be determined by using results from singular perturbation analysis. The idea is that if the slow system and the fast system are both asymptotically stable, then the combined system is also asymptotically stable for initial conditions close enough to the equilibrium point and for ϵ sufficiently small. The full closed loop system is reproduced below.
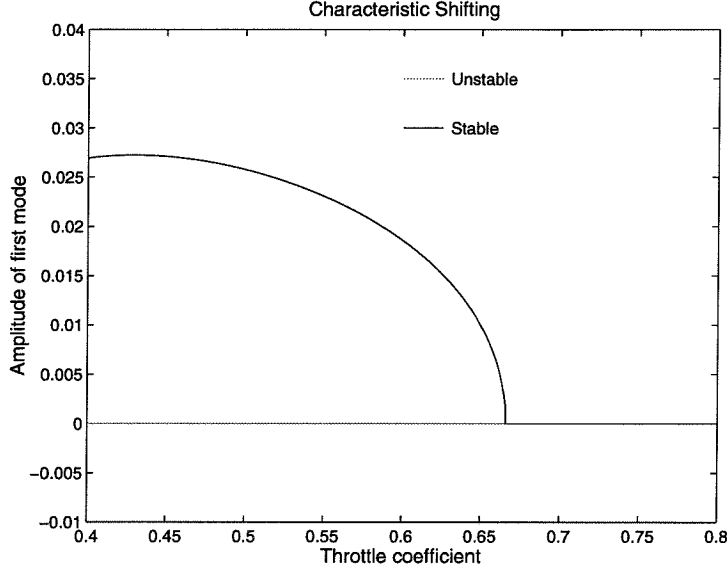
Figure 2.8 Closed loop bifurcation diagram required in decoupling analysis.

$$\frac{d\tilde{\Psi}}{d\tilde{\xi}} = \frac{1}{4B^2}\left(\tilde{\Phi} + \Phi_e - \left[\gamma_0 + k_1\left(\Psi_c + k_2(\tilde{J}_1 + J_{1e})\Psi_{c_u}\right.\right.\right.$$
$$\left.\left.\left. - \tilde{\Psi} - \Psi_e + \frac{\tilde{J}_1 + J_{1e}}{4}\frac{\partial^2\Psi_c}{\partial\Phi^2}\right)\right]\sqrt{\tilde{\Psi} + \Psi_e}\right)$$

$$\frac{d\tilde{\Phi}}{d\tilde{\xi}} = \left(\Psi_c + k_2(\tilde{J}_1 + J_{1e})\Psi_{c_u} - \tilde{\Psi} - \Psi_e + \frac{\tilde{J}_1 + J_{1e}}{4}\frac{\partial^2\Psi_c}{\partial\Phi^2}\right)$$

$$\epsilon\frac{d\tilde{J}_1}{d\tilde{\xi}} = \frac{2}{2+\mu}(\tilde{J}_1 + J_{1e})\left(\frac{\partial\Psi_c}{\partial\Phi} + k_2(\tilde{J}_1 + J_{1e})\frac{\partial\Psi_{c_u}}{\partial\Phi} + \frac{\tilde{J}_1 + J_{1e}}{8}\frac{\partial^3\Psi_c}{\partial\Phi^3}\right). \quad (2.58)$$

Theorem 2.1 *For a given throttle setting* γ_0, *the closed loop system* (2.58) *is locally asymptotically stable for an appropriate choice of gains* k_1 *and* k_2, *and* ϵ *sufficiently small.*

Proof: Note that the closed loop system described in equations (2.58) requires equations (2.50), (2.51), and (2.52) to be complete, and that for the class of compressors studied here a_3 (from equation (2.51)) is negative. The gain for the compressor characteristic shift, k_2, is first selected, so as to make the entire branch of equilibria associated with the bifurcation to rotating stall be stable. This can be accomplished using equation (2.33) to compute the value of k_2 which provides an infinite slope to the bifurcation diagram at γ^*. This selection of k_2 will produce a bifurcation

diagram similar to that shown in Figure 2.8. To complete the proof, the stability of the fast and slow subsystems must be shown; this is performed in the next two lemmas.

Lemma *The fast dynamics are asymptotically stable for the choice of k_2 given in Figure 2.8.*

Proof: This can be shown using the Lyapunov function

$$V(\tilde{J}_1) = \frac{1}{2}\tilde{J}_1^2. \tag{2.59}$$

Computing the derivative along the trajectories of the fast dynamics gives

$$\dot{V} = \tilde{J}_1 \dot{\tilde{J}}_1, \tag{2.60}$$

where

$$\dot{\tilde{J}}_1 = \frac{2}{2+\mu}(\tilde{J}_1 + J_{1e})\left(\frac{\partial \Psi_c}{\partial \Phi} + k_2(\tilde{J}_1 + J_{1e})\frac{\partial \Psi_{c_u}}{\partial \Phi} + \frac{\tilde{J}_1 + J_{1e}}{8}\frac{\partial^3 \Psi_c}{\partial \Phi^3}\right). \tag{2.61}$$

Note that equation (2.61) is equation (2.53) with time scaled by ϵ. Equation (2.60) therefore reduces to

$$\dot{V} = \frac{2}{2+\mu}\left(\tilde{J}_1 + J_{1e}\right)\tilde{J}_1\left(\frac{\partial \Psi_c}{\partial \Phi} + k_2(\tilde{J}_1 + J_{1e})\frac{\partial \Psi_{c_u}}{\partial \Phi} + \frac{\tilde{J}_1 + J_{1e}}{8}\frac{\partial^3 \Psi_c}{\partial \Phi^3}\right). \tag{2.62}$$

For an equilibrium point to the right of the peak of the compressor characteristic $J_{1e} = 0$, and all of the terms of equation (2.62) are less than zero when $\tilde{J}_1 \neq 0$. Since $\dot{V}$ is negative definite the origin is asymptotically stable (see Khalil [28]). In this case, since $\dot{V}$ is quadratic, the fast system is exponentially stable.

To the left of the peak the equilibrium value of the first mode stall cell amplitude (using equation (2.61)) becomes

$$J_{1e} = \frac{-\frac{\partial \Psi_c}{\partial \Phi}}{\frac{1}{8}\frac{\partial^3 \Psi_c}{\partial \Phi^3} + k_2\frac{\partial \Psi_{c_u}}{\partial \Phi}}. \tag{2.63}$$

This gives

$$\dot{V} = \frac{2}{2+\mu}\left(\tilde{J}_1 + J_{1e}\right)\tilde{J}_1\left[\frac{\partial \Psi_c}{\partial \Phi} + k_2\tilde{J}_1\frac{\partial \Psi_{c_u}}{\partial \Phi} + \frac{\tilde{J}_1}{8}\frac{\partial^3 \Psi_c}{\partial \Phi^3} + \left(k_2\frac{\partial \Psi_{c_u}}{\partial \Phi} + \frac{1}{8}\frac{\partial^3 \Psi_c}{\partial \Phi^3}\right)\frac{-\frac{\partial \Psi_c}{\partial \Phi}}{\frac{1}{8}\frac{\partial^3 \Psi_c}{\partial \Phi^3} + k_2\frac{\partial \Psi_{c_u}}{\partial \Phi}}\right], \tag{2.64}$$

which reduces to

$$\dot{V} = \frac{2}{2+\mu} \left(\tilde{J}_1 + J_{1e} \right) \tilde{J}_1^{\ 2} \left(k_2 \frac{\partial \Psi_{c_u}}{\partial \Phi} + \frac{1}{8} \frac{\partial^3 \Psi_c}{\partial \Phi^3} \right). \tag{2.65}$$

Note that $\tilde{J}_1 + J_{1e}$ is always positive, $\frac{\partial \Psi_{c_u}}{\partial \Phi} = c_1 < 0$ (see equation (2.52)), and $\frac{\partial^3 \Psi_c}{\partial \Phi^3} = 6a_3 < 0$ (see equation (2.50)). Since $\dot{V}$ is negative definite, the origin is again asymptotically stable.

The final case is right at the peak of the compressor characteristic $\Psi_c(\Phi)$, where $\frac{\partial \Psi_c}{\partial \Phi} = 0$, and therefore

$$\dot{V} = \frac{2}{2+\mu} \left(\tilde{J}_1 + J_{1e} \right) \tilde{J}_1^{\ 2} \left(\frac{1}{8} \frac{\partial^3 \Psi_c}{\partial \Phi^3} \right). \tag{2.66}$$

Since $\dot{V}$ is negative definite and the origin is also asymptotically stable (note that $\dot{V}$ is not quadratic in this case). ▼

Lemma *The slow system dynamics are exponentially stable for a sufficiently negative value of throttle controller gain k_1.*

Proof: This can be shown by computing the linearization of the system and verifying that the eigenvalues are always negative. The linearization of the closed loop slow system is given by:

$$\begin{bmatrix} \dot{\tilde{\Psi}} \\ \dot{\tilde{\Phi}} \end{bmatrix} = A \begin{bmatrix} \tilde{\Psi} \\ \tilde{\Phi} \end{bmatrix} \tag{2.67}$$

$$A = \begin{bmatrix} a_{11} & a_{12} \\ a_{21} & a_{22} \end{bmatrix}, \tag{2.68}$$

where

$$a_{11} = \frac{-1}{8B^2\sqrt{\Psi_e}} \left[\gamma_0 + k_1 \left(\Psi_c + k_2 J_{1e} \Psi_{c_u} + \frac{J_{1e}\Psi_c''}{4} - 3\Psi_e \right) \right] \tag{2.69}$$

$$a_{12} = \frac{1}{4B^2} \left[1 - \left(k_1 k_2 (J_{1e}'\Psi_{c_u} + J_{1e}\Psi_{c_u}') + k_1(J_{1e}'\Psi_c'' + J_{1e}\Psi_c''') \right) \sqrt{\Psi_e} \right] \tag{2.70}$$

$$a_{21} = -1 \tag{2.71}$$

$$a_{22} = \Psi_c' + k_2 J_{1e} \Psi_{c_u}' + \frac{J_{1e}\Psi_c'''}{4} + k_2 J_{1e}'\Psi_{c_u} + \frac{J_{1e}'\Psi_c''}{4}. \tag{2.72}$$

In these equations $(\ )'$ denotes partial differentiation with respect to Φ, and all quantities are evaluated at the point (Φ_e, Ψ_e). Note that near the peak of the compressor characteristic, a_{12} and a_{21} have opposite sign and to the right of the peak (where $J_{1e} = 0$) the surge dynamics are exponentially stable. Since a_{12} and a_{21} have opposite sign, if the trace of A is zero, the slow system will have pure imaginary

eigenvalues. Testing for $\text{Tr}(A) = 0$ gives

$$\text{Tr}(A) = \Psi'_c + k_2 J_{1e} \Psi'_{c_u} + \frac{J_{1e} \Psi'''_c}{4} + k_2 J'_{1e} \Psi_{c_u} + \frac{J'_{1e} \Psi''_c}{4} - \frac{1}{8B^2 \sqrt{\Psi_e}} \left[\gamma_0 + k_1 \left(\Psi_c + k_2 J_{1e} \Psi_{c_u} + \frac{J_{1e} \Psi''_c}{4} - 3\Psi_e \right) \right]. \qquad (2.73)$$

Note that for a third order compressor characteristic (which characterizes a real system), i.e.

$$\Psi_c(\Phi) = a_0 + a_1 \Phi + a_2 \Phi^2 + a_3 \Phi^3, \qquad (2.74)$$

$a_3 < 0$. In addition, the types of compressor characteristic shifts considered here move the peak of the compressor characteristic up and to the left, i.e. equation (2.52) with $c_0 > 0$ and $c_1 < 0$. Note that to the left of the peak, Ψ_{c_u} is always positive. Under these conditions the signs of the terms in equation (2.73) can be determined. To begin with, to the right of the peak of the compressor characteristic, $J_{1e} = 0$, and all of the terms are negative (note that $\Psi_c(\Phi_e) - 3\Psi_e = -2\Psi_e$). Under these conditions, the slow system dynamics are therefore exponentially stable.

To the left of the peak the Ψ'_c term is positive, and therefore, in order to keep the system exponentially stable, the remaining terms must be made sufficiently negative that $\text{Tr}(A)$ remains negative. The term $k_2 J_{1e} \Psi'_{c_u}$ term is less than zero since c_1 is less than zero (note that J_{1e} and k_2 are positive). The term $\frac{J_{1e} \Psi'''_c}{4}$ is negative since $a_3 < 0$. The condition on the remaining terms is given by

$$k_1 < \frac{-4\Psi'_c - J'_{1e} \Psi''_c}{4(2\Psi_e - k_2 J_{1e} \Psi_{c_u})}. \qquad (2.75)$$

Note that this condition will always be satisfied near the peak of the compressor characteristic since there $(-4\Psi'_c - J'_{1e} \Psi''_c) < 0$ and $4(2\Psi_e - k_2 J_{1e} \Psi_{c_u}) > 0$. Therefore the negative gain on the throttle controller extends the region of exponential stability of the slow system. ▼

Because of the uniform asymptotic stability of the two subsystems (the slow system was shown to be exponentially stable, which implies asymptotic stability), the combined system is locally asymptotically stable. This can be shown using a theorem due to Hoppensteadt [6], and also by Theorem 8.2 in the text by Khalil [28]. In Khalil's theorem, bounds for the allowable size of ϵ can also be computed. This computation requires the parameterization of the compressor characteristic and the compressor characteristic shift. ■

The decoupling analysis presented here is usefull because it shows that in some situations, controllers for the rotating stall and surge dynamics can be designed separately and the results combined. A combined surge and rotating stall controller along the lines presented here is presented in Chapter 5, and the experimental results suggest that this sort of design has promise on the physical system.

Chapter 3

High-fidelity Modeling

The 3-state Moore-Greitzer model presented earlier provided an analysis tool for understanding how best to exploit the structure of the compression system for control purposes. While this model provides good qualitative comparison with experimental data, it performs poorly in quantitative comparisons. The MG-3 model is particularly poor at capturing multiple characteristics observed in experiments, i.e. capturing both the size of the rotating stall hysteresis loop and the stall cell growth rate. In order to develop simulations which predict (or match) experimental results more complicated models must therefore be used.

One model which has been used successfully to simulate the details of the transition to rotating stall is also based on the Moore-Greitzer PDE model for compression systems. This model includes arbitrary number of circumferential Fourier modes (in a way which is attractive for control purposes) and dynamics for how the compressor characteristic, Ψ_c, responds to unsteadiness in the flow coefficient ϕ. This model was originally presented by Mansoux in [31] and will be referred to as the distributed model. This distributed model was also investigated by Setiawan [41]. In [31] experimental measurements of the local flow rate near the compressor face were made during the transition to rotating stall for three different compressors, the simulation parameters in the distributed model were then tuned to give the best match to the experiments. The results were quite good.

In this chapter, the open loop distributed model will be presented and then extended to include the air injection actuators installed on the Caltech rig. This air injection extension will incorporate the shifted compressor characteristic and the mass/momentum terms developed in Chapter 2, with slight modifications to fit into the higher-fidelity distributed model.

3.1 Unactuated Distributed Model

The distributed model provides a strong connection between the simulation and the experiment because the local flow coefficients at discrete points around the compressor annulus correspond directly to the states of the model. As more modes are included in the simulation, the number of points around the compressor annulus increases. The central point of the model is to use the Discrete Fourier Transform

(DFT) to move between flow coefficient perturbations in physical coordinates to flow coefficient perturbations in Fourier modes.

3.1.1 Description

The distributed model makes nearly the same assumptions as those presented in the three state model section. The only relaxations involve the single Fourier mode truncation for the flow coefficient perturbation and the time response of the compressor characteristic. The upstream potential flow solution that will be substituted into the Moore and Greitzer PDE is written (in a slightly different form than in Chapter 2) as

$$\delta\Theta(\theta,\eta,\xi) = \sum_{n=1}^{\infty} \frac{\tilde{\phi}_n(\xi)}{n} e^{in\theta} e^{n\eta} \qquad \eta \le 0, \tag{3.1}$$

where i is $\sqrt{-1}$, $\tilde{\phi}_n$ is n^{th} spatial Fourier coefficient of the velocity perturbation at the compressor face[1] ($\eta = 0$). This equation leads to the following expression for the velocity perturbation at the compressor face

$$\delta\phi(\theta,\eta,\xi) = \sum_{n=1}^{\infty} e^{n\eta} \tilde{\phi}_n(\xi) e^{in\theta} \qquad \eta \le 0. \tag{3.2}$$

Substituting this relation into equation (2.16) gives

$$\sum_{n=1}^{\infty} \left(\frac{2}{n} \dot{\tilde{\phi}}_n + \mu \dot{\tilde{\phi}}_n + in\lambda\tilde{\phi}_n \right) = \Psi_c(\Phi + \delta\phi) - \int_0^{2\pi} \Psi_c(\Phi + \delta\phi) d\theta. \tag{3.3}$$

Unsteady loss dynamics

The compressor performance characteristic $\Psi_c(\Phi)$ is a steady state map which describes how the pressure rise delivered is related to the flow rate through the compressor. In practice, this is only a good approximation if the flow rate is a constant or slowly varying. Haynes et al. [23] proposed the following model for a transients that occur when the flow rate through the compressor is time varying

$$\Psi_c(\Phi,\xi) = \Psi_{isen}(\Phi) - L_r(\Phi,\xi) - L_s(\Phi,\xi), \tag{3.4}$$

where Ψ_{isen} is the isentropic total pressure rise across the compressor and L_r and L_s are the rotor and stator total pressure losses. The equations for how L_r and L_s

---

[1]Note that therefore

$$\tilde{\phi}_n(\xi) = \frac{1}{2\pi} \int_0^{2\pi} \delta\phi(\theta,0,\xi) e^{-in\theta} d\theta.$$

evolve with time are given by

$$\tau_L \left(\frac{\partial(L_r)}{\partial \xi} + \frac{\partial L_r}{\partial \theta} \right) = L_{sr}(\phi) - L_r, \tag{3.5}$$

and

$$\tau_L \frac{\partial(L_s)}{\partial \xi} = L_{ss}(\phi) - L_s, \tag{3.6}$$

where L_{rs} and L_{ss} are the steady total pressure loss across the rotor and the stator and τ_L is the unsteady loss dynamics time constant.

These equations basically describe the time lags in the pressure rise delivered by the compressor associated with the transition from one flow rate to another. These equations become especially important when the compressor characteristic is assumed to hold locally around the compressor annulus during rotating stall, since the flow rate will vary substantially over short time scales (since the stall cell is a moving area of decreased flow which moves at a significant percentage of the rotor speed).

3.1.2 Unactuated equations

The equations of motion for the distributed model of an axial flow compression system are developed from the treatment by Mansoux et al. [31]. The additions here correspond to the addition of the unsteady loss dynamics described by Haynes et al. [23]. The resulting equations are

$$\dot{\vec{\phi}} = E^{-1} \left(-A\vec{\phi} + \Psi_c(\vec{\phi}) - T\Psi \right) \tag{3.7}$$

and

$$\dot{\Psi} = \frac{1}{4l_cB^2} \left(S\vec{\phi} - \gamma\sqrt{\Psi} \right), \tag{3.8}$$

where $\vec{\phi}$ is the vector of flow coefficients at discrete points around the compressor annulus, Ψ is the annulus averaged pressure rise coefficient,

$$A = G^{-1}D_A G \qquad E = G^{-1}D_E G, \tag{3.9}$$

where G is the real valued Discrete Fourier Transform matrix which maps the flow coefficient values at discrete points around the compressor annulus (which are stacked as column vector in $\vec{\phi}$) to the real and imaginary components of the Fourier

coefficients:

$$G : \vec{\phi} \mapsto \begin{bmatrix} \tilde{\phi}_0 \\ \mathrm{Re}(\tilde{\phi}_1) \\ \mathrm{Im}(\tilde{\phi}_1) \\ \vdots \\ \mathrm{Re}(\tilde{\phi}_n) \\ \mathrm{Im}(\tilde{\phi}_n) \end{bmatrix},$$

where $\tilde{\phi}_j$ corresponds to the Fourier coefficient associated with the jth mode. The matrix G is given by

$$G = \frac{2}{2n+1} \begin{bmatrix} \frac{1}{\sqrt{2}} & \frac{1}{\sqrt{2}} & \cdots & \frac{1}{\sqrt{2}} \\ \cos\theta_1 & \cos\theta_2 & \cdots & \cos\theta_{2n+1} \\ \sin\theta_1 & \sin\theta_2 & \cdots & \sin\theta_{2n+1} \\ \cos 2\theta_1 & & & \\ \sin 2\theta_1 & & \ddots & \\ \vdots & & & \\ \cos n\theta_1 & \cos n\theta_2 & \cdots & \cos n\theta_{2n+1} \\ \sin n\theta_1 & \sin n\theta_2 & \cdots & \sin n\theta_{2n+1} \end{bmatrix}, \qquad (3.10)$$

where the θ_j are the angular positions around the compressor annulus of each of the discrete points associated with the elements of ϕ. The remaining elements of equations (3.7) and (3.8) listed below, the precise meaning of each should be referenced from [31] and [25].

$$D_A = \begin{bmatrix} 0 & & & \\ & \begin{bmatrix} 0 & \lambda \\ -\lambda & 0 \end{bmatrix} & & \\ & & \ddots & \\ & & & \begin{bmatrix} 0 & n\lambda \\ -n\lambda & 0 \end{bmatrix} \end{bmatrix}$$

$$D_E = \begin{bmatrix} l_c & & & \\ & \begin{bmatrix} (\frac{2}{1}+\mu) & 0 \\ 0 & (\frac{2}{1}+\mu) \end{bmatrix} & & \\ & & \ddots & \\ & & & \begin{bmatrix} (\frac{2}{n}+\mu) & 0 \\ 0 & (\frac{2}{n}+\mu) \end{bmatrix} \end{bmatrix}$$

$$S = \begin{bmatrix} \frac{1}{2n+1} & \cdots & \frac{1}{2n+1} \end{bmatrix}. \qquad (3.11)$$

$$T = \begin{bmatrix} 1 & \cdots & 1 \end{bmatrix}^T. \qquad (3.12)$$

The unsteady loss dynamics are introduced into equations (3.7) and (3.8) by defining

$$W = G^{-1}D_W G, \tag{3.13}$$

where

$$D_W = \begin{bmatrix} \frac{1}{\tau_L} & & & & \\ & \begin{bmatrix} \frac{1}{\tau_L} & 1 \\ -1 & \frac{1}{\tau_L} \end{bmatrix} & & & \\ & & \ddots & & \\ & & & \begin{bmatrix} \frac{1}{\tau_L} & n \\ -n & \frac{1}{\tau_L} \end{bmatrix} \end{bmatrix}.$$

The distributed model versions of equations (3.6) and (3.5) are

$$L_{rs} = \Psi_{isen}(\Phi) - \Psi_{c_{ss}}(\Phi)R \qquad L_{ss} = \frac{1-R}{R}L_{rs} \tag{3.14}$$

and

$$\dot{L}_r = \frac{1}{\tau_L}(WL_{rs}(\vec{\phi}) - L_r) \qquad \dot{L}_s = \frac{1}{\tau_L}(L_{ss}(\vec{\phi}) - L_s). \tag{3.15}$$

$$\Psi_c(\vec{\phi}, \xi) = \Psi_{isen}(\vec{\phi}) - L_R(\vec{\phi}, \xi) - L_S(\vec{\phi}, \xi). \tag{3.16}$$

The above equations give one ODE for the average pressure rise coefficient Ψ, $(2n+1)$ ODEs for the vector of flow coefficients around the annulus $\vec{\phi}$, $(2n+1)$ ODEs for the losses across the rotor L_r, and $(2n+1)$ ODEs for the losses across the stator L_s. This results in a total of 46 ODEs if an open loop model with seven modes being simulated.

3.2 Distributed Model with Air Injection

In this section, the additions to the distributed model that were used to simulate the air injectors installed on the Caltech rig. The distributed model is attractive for modeling the air injection on the Caltech rig because the steady state compressor characteristic shifting can be included in a local way instead of as an axially averaged shift (as was done in the analysis on the MG–3 model). This allows the compressor characteristic to be shifted in phase as well as in magnitude. This actuated distributed model will later in Chapter 7 to perform simulation based parametric studies and to match the experimental results for rotating stall control using air injection which will be presented in 5.

The Caltech compressor rig has three air injectors placed 120 degrees apart around the compressor annulus (further details on this will be presented in Chapter 4) and each injector has an effect on a small region of the compressor rotor. In the distributed model, the pressure rise delivered by the compressor around the annulus

is given by $\Psi_c(\phi_i)$ where ϕ_i is the flow coefficient at location i. In this model, the compressor performance characteristic shifting and the mass/momentum addition effects will both be included.

Compressor characteristic shift

In order to include the compressor characteristic shifting as a local effect, the shift is included as

$$\Psi_c(\phi_i) = \Psi_{c_{nom}}(\phi_i) + \left(\Psi_{c_{sh}}(\phi_i) - \Psi_{c_{nom}}(\phi_i)\right) F(u_i) \tag{3.17}$$

at the points around the annulus which have air injectors associated with them and as

$$\Psi_c(\phi_i) = \Psi_{c_{nom}}(\phi_i) \tag{3.18}$$

for the remaining positions. Here $\Psi_{c_{nom}}$ is the nominal compressor characteristic, while $\Psi_{c_{sh}}$ is the locally shifted characteristic. The control variables are the u_i, which take the values of 0 or 1 if the air injector is off or on respectively. The transient effect of the air injection on the compressor characteristic shift is modeled as a delay followed by a first order lag; this is captured by operator F, which takes the time history of the commanded valve position (0 or 1) and computes the current valve position. The values for the delay and lag were chosen to correspond to the values observed in the experiment, for further details on the exact values of these lags see Appendix C.

Mass and momentum effects

In order to include the mass and momentum addition effects, a relation similar to equation (2.42) will be used. As was previously described, the mass and momentum terms result in an augmentation of the compressor performance characteristic. At the points in the compressor annulus which have air injectors associated with them

$$\Psi_{c_{ai}}(\phi_i) = \Psi_{c_{nom}}(\phi_i) + \left(\Psi_{c_{sh}}(\phi_i) - \Psi_{c_{nom}}(\phi_i)\right) F(u_i) +$$
$$(\Phi_j - \phi_i)\frac{F(u_i)}{l_a}\Phi_j - \frac{1}{2}\left(\frac{F(u_i)}{l_a}\Phi_j\right)^2 \tag{3.19}$$

where u_i is the opening of the air injector, and F is the delay/first order lag operator described above. As before, the points which did not have air injectors associated with them had a compressor performance characteristic of

$$\Psi_c(\phi_i) = \Psi_{c_{nom}}(\phi_i). \tag{3.20}$$

Note that in this model for the air injectors, the shifted compressor characteristic $\Psi_{c_u}(\phi_i)$ includes both the swirl effect and the axial velocity effects.
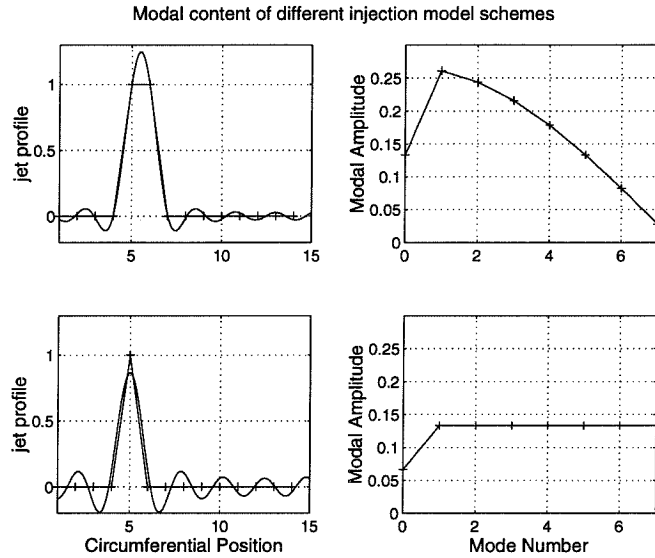
Modal content of different injection model schemes

Figure 3.1 Comparison of modal content for two different discrete air injection models. Each model corresponds to fifteen discrete points around the compressor annulus.

Air injection modeling

In order to best model the air injection actuators, the points around the compressor annulus where the proceeding compressor characteristic shifts would be implemented need to be determined. While the obvious solution may seem to use three equally spaced points around the annulus, Figure 3.1 shows why this is not the best modeling choice. The reason lies in the modal content that the DFT predicts for a single point air injection scheme. The figure shows the amplitude of the Fourier coefficients for a scheme which models a single air injector as having an effect at an isolated point in the compressor annulus and for a scheme that models a single air injector as having an equal effect at two adjacent points in the compressor annulus. The single point scheme has equal amplitude for all of the Fourier modes, but the two point scheme has roll-off as the mode number increases. The figure also shows that there is much less overshoot and oscillation when the input to the DFT is reconstructed from the Fourier modes.

Chapter 4

Description of Experiment

This chapter presents a hardware description of the Caltech compressor rig, as well as some experimental measurements which give insight into the behavior of this particular compressor system. The two main rig configurations, the rotating stall configuration and the surge configuration, are both described. In addition, the individual components that make up the compression system and the rig instrumentation (i.e. computer interface) are also described. Further details on the rig components are presented in Appendix A. In order to better motivate the detailed work associated with the distributed model simulation, the basic experimental setup must be described. The experimental descriptions and data presented in this chapter are background information that will be referred to throughout the remaining chapters.

Measurements for the unactuated compressor include the compressor performance map and transient measurements of the transition to rotating stall; in addition, further detailed measurements of the compressor behavior presented in Appendix B. The effects of open loop air injection actuation are also presented, including a parametric study to determine how open loop air injection geometric parameters effect the compressor performance characteristic. The study is a search for the optimal placement and orientation of the air injection actuators; in this case optimal refers to the set of geometric parameters which produce the most favorable change in the bifurcation diagrams as described in the analysis presented in Section 2.3.1.

4.1   Compressor System

In order to investigate and validate active control techniques for rotating stall and surge, a low-speed, axial flow compressor facility was designed built. Initial construction was performed Khalak [26], and modifications have been continuous since then. The compressor system is built around an axial fan manufactured by Able Corporation. While this compressor is substantially simpler than a typical compressor in a gas turbine engine (it is low speed and has a single stage), the overall compression system has many of the essential operating characteristics of high speed engines and is ideally suited for implementation of active control techniques due to
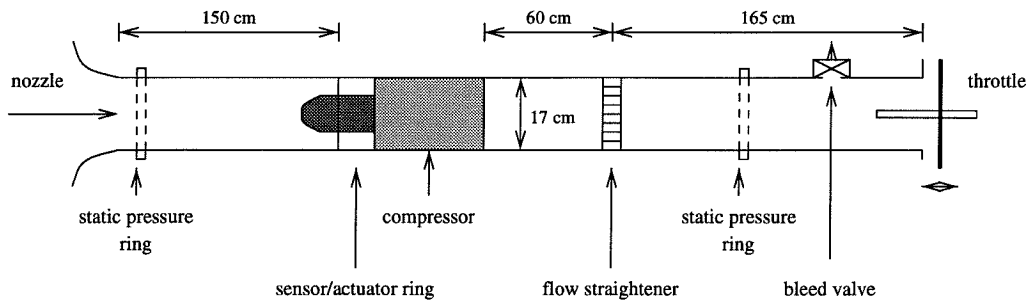
Figure 4.1 Caltech compressor rig in rotating stall configuration, see text for complete description.

its size and ease of use.

The rig includes numerous "bolt on" subsystems which are used to investigate specific aspects of compression system dynamics (an example of which is the removable plenum which is used to change the dominant instability from rotating stall to surge). The overall compressor system will be described first, and then the three subsystems that were required to perform the majority of the experimental work presented here. Further details on the individual components which make up each of these subsystems (and others) can be found in Appendix A.

The Caltech rig was designed to be run in one of two main configurations, one configuration in which the rotating stall dynamics dominate, and a second in which the surge dynamics are dominant. Figure 4.1 shows a schematic of the rig in the configuration in which the rotating stall dynamics dominate. The rig can be modified such that the surge dynamics dominate by adding a 1.81 m^3 plenum between the outlet duct static pressure ring and the throttle. These two configurations will referred to throughout this and the remaining chapters as the rotating stall configuration and the surge configuration respectfully. This compression system was designed and constructed in accordance with AMCA/ASHRE standards for measurement and calibration of compressors of this type [2].

The compression system consists of the following components (from left to right in Figure 4.1): an inlet nozzle, inlet duct, sensor/actuator ring, compressor, outlet duct, bleed valve, and exit throttle. The inlet nozzle is a smooth bell-mouth constructed to minimize the inlet flow distortion and is an integral part of the 17 cm diameter inlet duct. Sensors include a pair of static pressure rings on the inlet and outlet ducts (for measuring the slowly varying average static pressure in the duct), pitot measuring planes at the inlet and near the outlet (for measuring the velocity profile in the duct), an array of six static pressure transducers located in front of the compressor face (as part of the sensor and actuator ring), and hotwire probes mounted in the inlet duct and in the compressor housing. Throttle actuation is achieved with a low-speed, electrically driven throttle at the outlet (used to set the gross operating point of the rig) and a high speed bleed valve which can be located in the outlet duct either before or after the plenum (used to generate disturbances and for fine tuning the operating point). All sensors and actuators are interfaced to
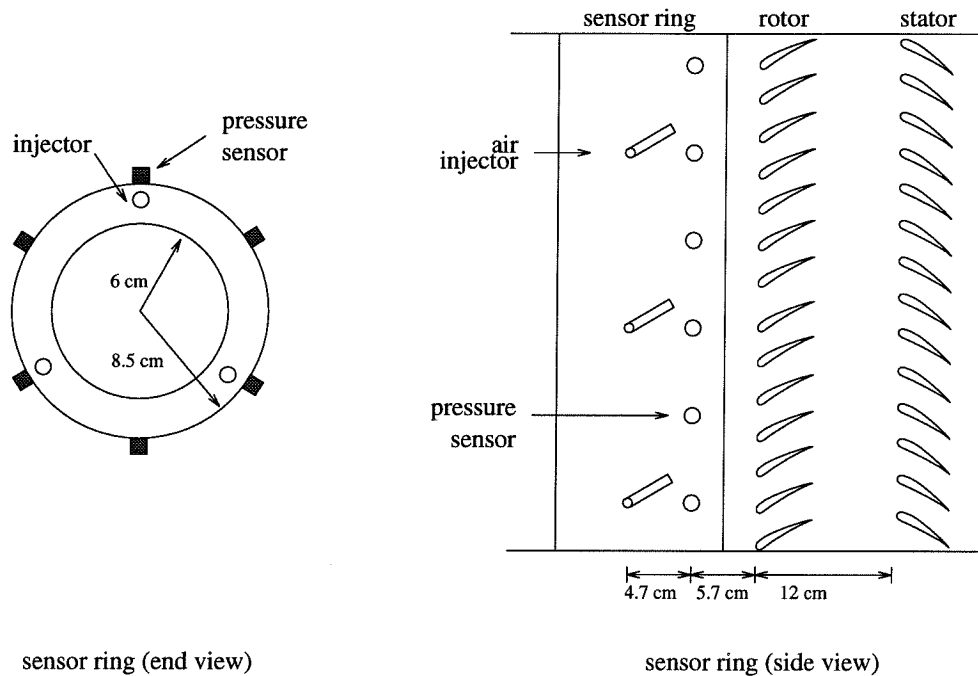
Figure 4.2 Sensor ring.

a PC-based real-time control computer which samples and updates at a servo rate of 2000 Hz. More details on the computer interface are presented in the following subsections and in Appendix A.

The main subsystems of the rig are the sensor/actuator ring, the compressor, and the bleed valve, each of which was used extensively in the experimental work presented here are described in the following subsections.

4.1.1 Sensor/actuator ring

Figure 4.1 shows the sensor/actuator ring in its normal position just upstream of the compressor, and a more detailed schematic is given in Figure 4.2. The ring is used to measure the unsteady pressures upstream of the rotor and to hold the air injection actuators. The ring is outfitted with six pressure transducers equally spaced around the compressor circumference, approximately 5 cm (0.7 mean rotor radii) upstream of the rotor. There are ports for up to 18 pressure sensors, but only six are typically used at any one time. These transducers have a resolution of approximately 1.2 Pa and a bandwidth of 1 kHz, and are low pass filtered (using filters further described in Appendix A) at 500 or 1000 Hz prior to sampling by a 12 bit A/D converter. These sensors are used to track the development of rotating stall in the compressor annulus. The inlet and outlet static pressure rings shown in Figure 4.1 are instrumented with similar transducers and are used to measure the presure rise delivered by the compressor.

Number of Blades	14
Hub radius	0.085 m
Tip radius	0.060 m
Blade chord	0.037 m
Rotation rate	6000 rpm

Table 4.1 Parameters for computing the aerodynamic performance of the rotor installed on the Able 29680 axial fan.

The three air injection actuators located on the ring are also shown in Figure 4.2. The flow through each of the injectors is controlled by an on/off solenoid valve, and the exit port of each injector can be placed at a variety of locations and orientations. The valves are actuated using custom overdriving circuitry interfaced directly to the data acquisition computer and are capable of providing a 50% duty cycle at up to 200 Hz. Hotwire measurements were performed to determine the velocity profile of the air injection at the compressor face, and further details on this testing are presented in Appendix C. The injected air was found to disperse from 3 mm at the exit of the injector to approximately 20 mm at the compressor face; this dispersion occurred over a distance of 9 cm (the distance between the exit of the air injector and the rotor face). This corresponds to each air injector changing the flow pattern at the compressor rotor over a region that is about 10% of the total compressor annulus. Based on these velocity profile measurements, three measures of control authority were calculated to characterize the air injectors: the mass flux, the momentum flux, and the energy flux. As a percentage of the mean values for the compressor operating at the peak of the compressor characteristic, the flow through each air injector on continuously contributed 1.7% to the mass flux, 2.4% to the momentum flux, and 1.3% to the energy flux. The control authority measures are thus small compared to the corresponding values for the compressor.

4.1.2 Compressor

The compressor is an Able Corporation model 29680. Table 4.1 shows several parameters of interest for compressors of this sort. Except where noted, throughout the work presented here the rig was run 6000 rpm. Under these conditions, the peak pressure rise coefficient is 0.38 at a flow coefficient of 0.37 (these values occur at the stall inception point), and the rotor tip speed has a Mach number of 0.17. Since the Mach number of the rotor blade tips is < 0.2 the flow is assumed incompressible. The compressor is driven by an induction motor, the speed of which can be set via the frequency of the input voltage. The rotation rate of 6000 rpm is achieved with a supply voltage at 200 Hz. Further details on the compressor can found in Appendix A.

4.1.3 Bleed valve

In addition to the low speed throttle used to set the operating point of the rig, the compression system is also outfitted with a secondary higher speed throttle. This high speed bleed valve is located just upstream of the primary throttle (see Figure 4.1) and is used to generate throttle disturbances and to fine tune the operating point of the system. The valve can modulate 0-30% of the flow through the compressor at the stall inception point. A calibration of the bleed valve position with the throttle coefficient γ (defined in Section 2.1) is presented in Section 6.3. The valve has large signal bandwidth of 20 Hz and small signal bandwidth of 50 Hz and is a butterfly design. It is controlled using simple servo motor, the set-point of which is commanded by the computer using custom built interface hardware.

4.1.4 Computer interface

A Pentium based PC was used to control operation of the rig and to perform data acquisition. Outputs from the computer to the rig include signals for: turning the compressor and each of the air injectors on or off, opening and closing the primary throttle, and setting the position of the bleed valve. Inputs to the computer from the rig include signals from: the inlet, outlet, and compressor annulus pressure transducers, the inlet duct and compressor annulus hotwire anemometers, and the position encoder installed on the bleed valve. This information is collected and sent using a standard data acquisition board and a variety of custom hardware. The flow of data to and from the PC is managed using the Sparrow real-time kernel [36] developed at Caltech. Sparrow provides a set of C routines for accessing I/O boards and executing servo-loops. As previously stated, the servo rate on the compressor rig is typically 2000 Hz.

4.2 Unactuated Compressor Behavior

There are some basic measurements of the open loop experimental behavior of the Caltech rig which are required for understanding what changes actuation (open or closed loop) produces. In this section some of these measurements are presented; they include compressor characteristic performance maps and transient data for the transition from a steady operating point to rotating stall. Transient data for surge cycles can be found in Section 6.2.

Additional measurements of the compressor behavior are located in Appendix B. In particular, the appendix contains data on how much the rotating stall cell extends throughout the compressor annulus (both over the span and around the circumference). The percentage of the overall pressure rise delivered by the rotor and by the stator are also presented.

4.2.1 Compressor performance characteristic

The dynamic behavior of the compressor system has many of the basic properties of high performance, axial flow compressors, and the primary way of showing this
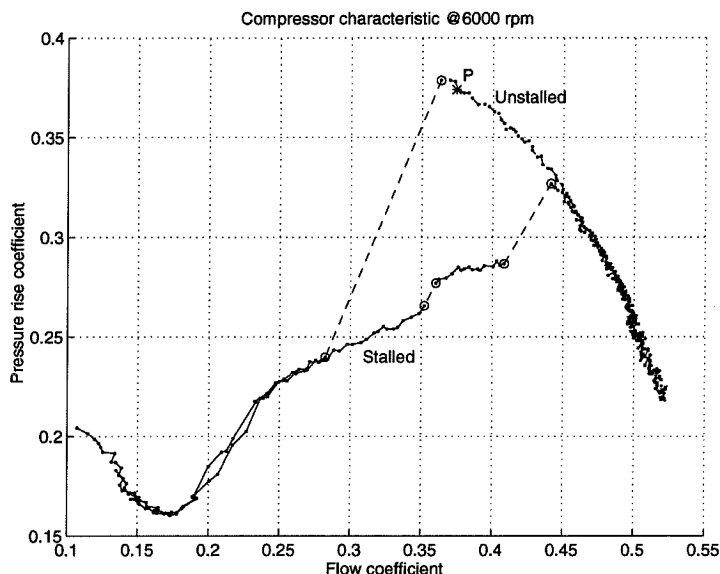
Figure 4.3 Caltech rig compressor characteristic. Dark lines indicate continuous changes in the operating point while lighter lines represent discontinuous changes. The circles mark the points of discontinuity. 'P' is the operating point for the parametric studies outlined in Chapter 5.

is by comparing the compressor performance to that obtained from a real engine, see for example the text by Wilson [44]. The measured compressor characteristic for the Caltech rig is shown in Figure 4.3. The effect of rotating stall is clearly seen in the measured compressor performance characteristic. As the flow is decreased beyond the value at which the characteristic reaches its peak (by closing down throttle), the compressor enters rotating stall and operates at a much lower average pressure. Once in rotating stall the flow must be increased substantially (by opening the throttle) before the system returns to the unstalled portion of the compressor characteristic.

4.2.2 Stall cell development

In addition to the annulus averaged values of the pressure rise and flow coefficients, it is also instructive to look at the transient behavior of the pressures in the compressor annulus near the rotor face. Figure 4.4 shows data taken using the six pressure transducers installed on the sensor/actuator ring. The figure shows a first mode dominated rotating stall condition. The rotation rate of the first mode of rotating stall just after the transition to stall was found to be 65 Hz. This corresponds to a single region of higher than average pressure rotating around the compressor annulus at 65 Hz. The plots in Figure 4.4 show the modal components of the pressure disturbance when a transition from unstalled to stalled behavior occurs. Since six equally spaced pressure transducers were used to measure the pressure disturbance,
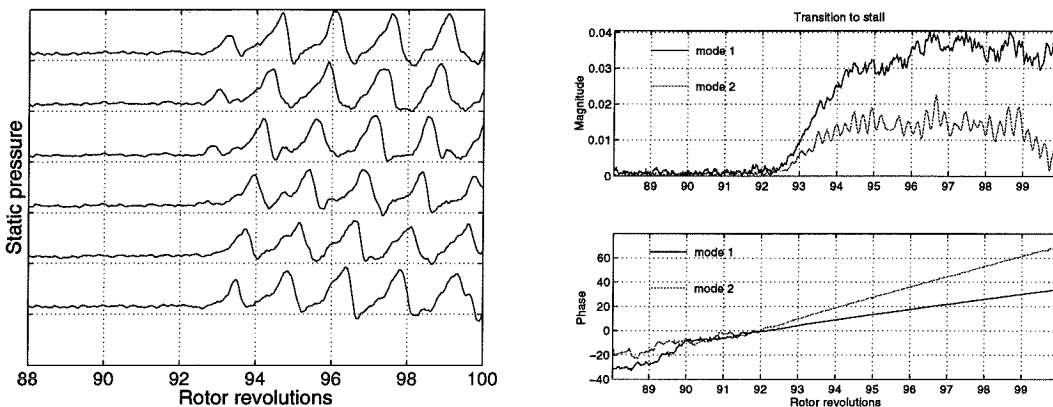
Figure 4.4 Annulus pressure transducer data for the transition to rotating stall.

only the first two modes could be determined. As can be seen, the dominant mode during the transition is the first one. From the slope of the phase plots one can conclude that the first mode disturbance is rotating at a rate of approximately 65 Hz, and the second mode is also rotating at approximately 65 Hz. This is consistent with a pressure disturbance rotating about the circumference of the compressor at a rate of 65 Hz. To ascertain that no significant aliasing was taking place due to the use of only six pressure transducers, time domain measurements were analyzed for each pressure transducer and the power spectrum determined. It was found that most of the signal power was contained in two bands centered around 65 Hz and 130 Hz. Assuming that the pressure disturbance is a traveling wave about the circumference of the compressor, this would indicate that the third mode component is also negligible spatially about the circumference of the compressor.

If the rig is allowed to continue to operate in a stalled condition, then there is a transition to a second mode dominant rotating stall. This corresponds to two regions of higher than average pressure rotating around the compressor annulus. These modes of rotating stall are bistable; i.e. the rig will transition back and forth between the two modes without changes in the throttle setting. This behavior is shown in Figure 4.5, and further measurements of this effect are presented in Appendix B. The figure suggests that at least two modes of rotating stall must be included in any model or simulation of the Caltech rig.

4.3 Actuated Compressor Behavior

The effects of the air injectors can be roughly characterized by their effect on the static compressor map. In [9], the effect of continuous air injection into the rotor face at different incident angles was investigated. Similar effects were presented by Day [11], and by Khalak and Murray [27]. The experimental results presented there indicated that the steady state compressor characteristic could be substantially
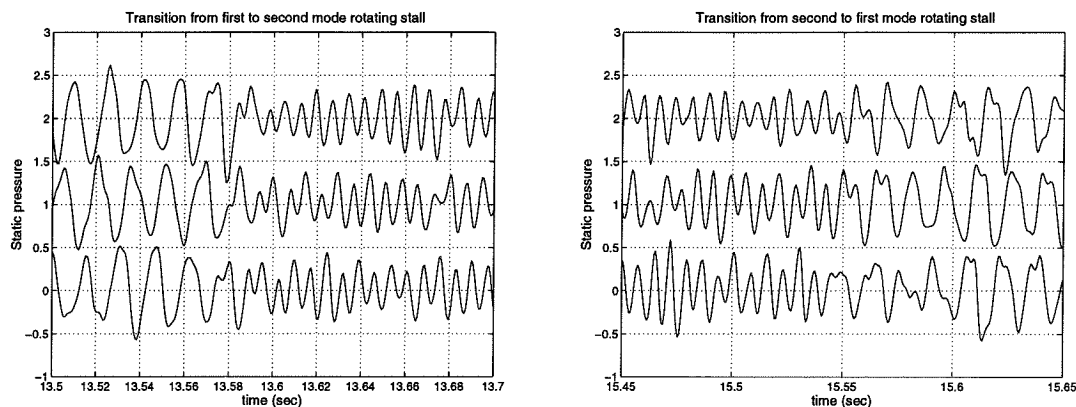
Figure 4.5 Bistable rotating stall, rig transitions between a dominant first mode rotating stall and a dominant second mode rotating stall.

altered by air injection. In Figure 4.6, the shifted compressor characteristics are plotted for various incident angles. In these plots, the flow coefficient corresponds to the mass flow through the compressor (sum of the inlet mass flow plus the injected mass flow). Note that for positive angles (air injected into the blade rotation), the shifting of the characteristic is approximately the same, the only difference is the stall inception point (as marked by circles).

In addition to the change in the flow and pressure rise coefficients at the transition to rotating stall, the size of the hysteresis region associated with clearing the rotating stall cell was also affected by the air injection. Figure 4.7 shows examples of how the size of the hysteresis region changes as the location and angle of air injection is changed. These effects are more carefully quantified an the air injection geometric parametric study.

Parametric study

The focus of these experiments was to determine how air injection upstream of the rotor can affect the stall characteristics of these compressors. In order to more carefully characterize these effects, several parametric studies were performed using continuous air injection. Figure 4.7 shows examples of how the steady compressor performance characteristic can be changed by continuous air injection; these figures where originally presented by D'Andrea et al. [9]. The shifts shown were obtained by changing the orientation of the air injection ports in the sensor/actuator ring, and three geometric variables are different between each of the plots. These three variables are the angle relative to the mean axial flow, the span position in the compressor annulus, and the distance that the injected air travels before reaching the rotor face. The experiments presented here separate the effects of each of these geometric parameters by measuring the compressor characteristic as each parameter is varied individually.

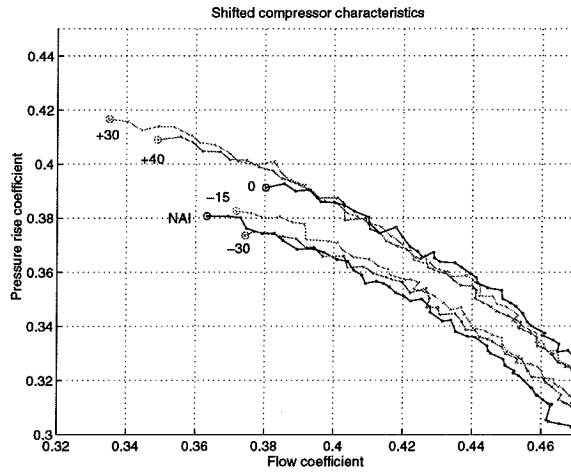Figure 4.8 shows a schematic of how the air injectors are physically placed in

Figure 4.6 Compressor characteristics for various air injection angles. 'NAI' corresponds to the unactuated case (no air injection). The circles mark the peak operating point for each compressor characteristic.
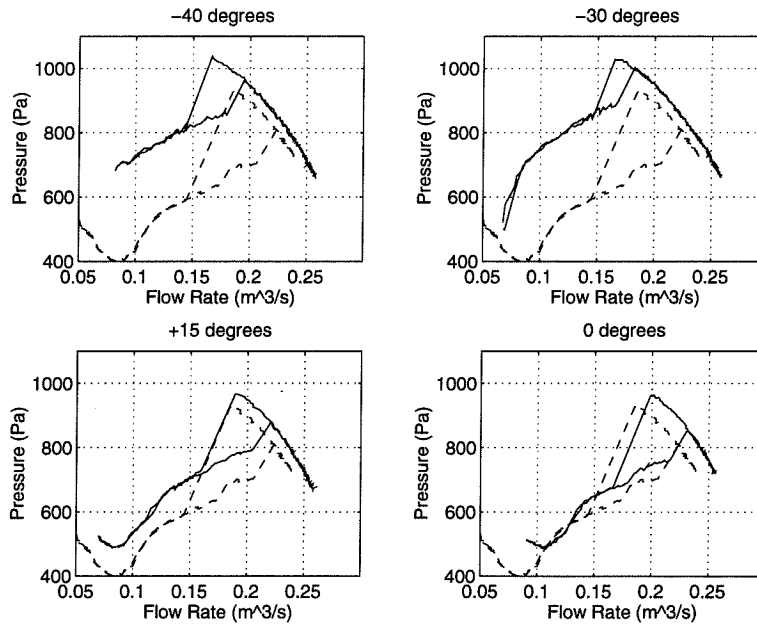

Figure 4.7 The compressor characteristic obtained for different air injection positions is shown as a solid line. For comparison, the compressor characteristic obtained with the air injection off is shown as a dashed line.
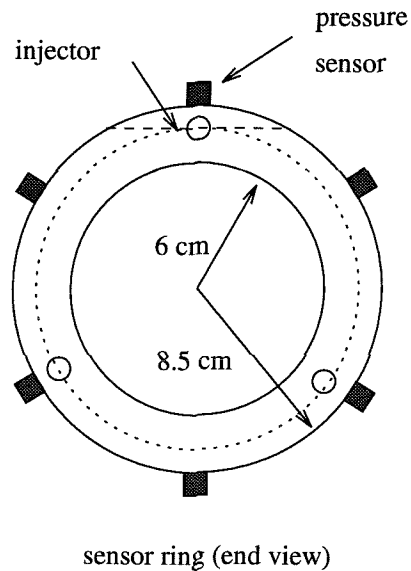
sensor ring (end view)

Figure 4.8 Parametric study details. The dashed line shows how the injection position was varied for the plots in Figure 4.7 and the dotted line shows how the injection position was varied for the plots in Figures 4.9 and 4.10.

the compressor annulus and shows each of the three geometric parameters described above. In the studies presented here, only the angle relative to the mean axial flow and the span wise position of the air injection were varied. The distance to the rotor face parameter has the additional effect of changing the velocity profile of the injected air by the time it reaches the rotor face, and this effect was investigated in a later parametric study where the amount of injected air was varied.

The shift of the compressor characteristic obtained by continuous air injection can be described by two parameters, the amount that the stall point is moved and the change in the size of the hysteresis loop. Figure 4.9 shows how the stalling flow rate is extended for various injection angles and spanwise injection heights. The plot shows the difference between stalling mass flow for the uninjected case and the continuous air injection case. Lower stalling flow rates than the uninjected case result in positive values in the plot. The results indicate that the greatest extensions occur at large angles and at near 100% span (i.e. tip).

In addition to the stalling flow coefficient extension, the presure rise at the stall point is also affected by the air injection. Figure 4.10 shows the change in the pressure rise delivered by the compressor system as a function of the injection angle and spanwise position. Again the results are plotted as the difference between the stalling pressure rise for the uninjected case and the injected case. Positive values in the plot correspond to the injected case providing higher pressure rise than the uninjected case. The plot shows that the greatest extension occurs for positive injection angles and 100% span injection.
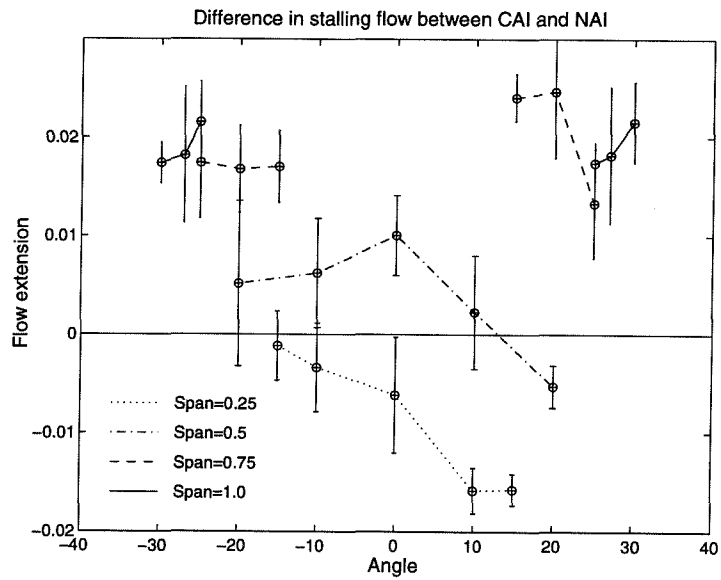
Figure 4.9 Air injection parametric study of geometric parameters: change in stalling flow coefficient.
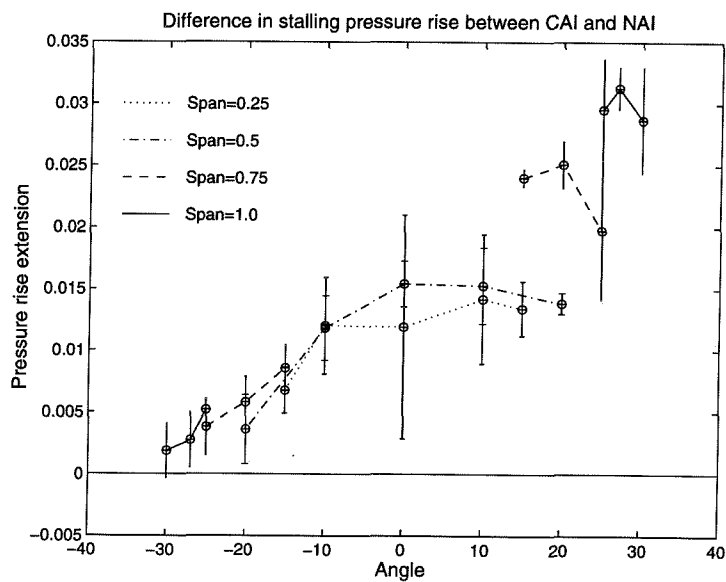

Figure 4.10 Air injection parametric study of geometric parameters: change in pressure rise at stall point.

The optimal choice for geometric location of the air injectors for closed loop experiments, based on the analysis presented in Section 2.3.1, would be positive injection angle around 30 degrees at the tip of the rotor.

In the second parametric study, the amount of injected air is varied in order to determine the minimum amount of injection required to achieve the decrease in stalling flow rate and the reduction in the size of the hysteresis loop. This study is of particular interest because the viability of air injection actuation on real gas turbine engines depends on using very low amounts of injection.

Chapter 5

Experimental Closed Loop Control of Stall and Surge

In this chapter, experiments in active control of rotating stall are presented. Experiments were performed to validate the analysis presented in Section 2.3.1 for a axial air injection scheme with proportional feedback on the stall cell amplitude. In addition, a pulsed air injection controller for rotating stall which takes advantage of the previously described shift in the steady state performance characteristic is presented (see Section 4.3). The optimal parameter choices for the pulsed air injection controller were determined through a global search. Based on these results, two rotating stall controllers are investigated, one which has a substantially different performance characteristic than the unactuated case and one in which the change in performance is not as drastic. The effects of this optimal controller, designed for the control of rotating stall, are investigated on the rig in the surge configuration. A second set of experiments is performed in an attempt to control surge using a bleed valve based controller. Finally, the combination of these two controllers is investigated experimentally as was suggested in Section 2.4.

5.1   1–D Rotating Stall Controller

In order to test the closed loop compressor characteristic shifting idea presented in Section 2.3.1, a series of experiments were performed. Recall that the control scheme presented there was based on a shift of the nominal compressor characteristic which was proportional to the amplitude of the first mode amplitude of the rotating stall, i.e.

$$\Psi_c = \Psi_{c_{nom}} + K J_1 \Psi_{c_u}. \tag{5.1}$$

In order to achieve this proportional feedback on the amplitude of the stall cell magnitude, the duty cycle of the air injectors was varied. A carrier frequency of 100 Hz was used, with the duty cycle varying between 0–100% proportional to the amplitude of the static pressure perturbation amplitude. Two shifts were investigated, one with a rotating stall hysteresis region that did not overlap that of the uninjected case and one with a hysteresis region that did overlap.
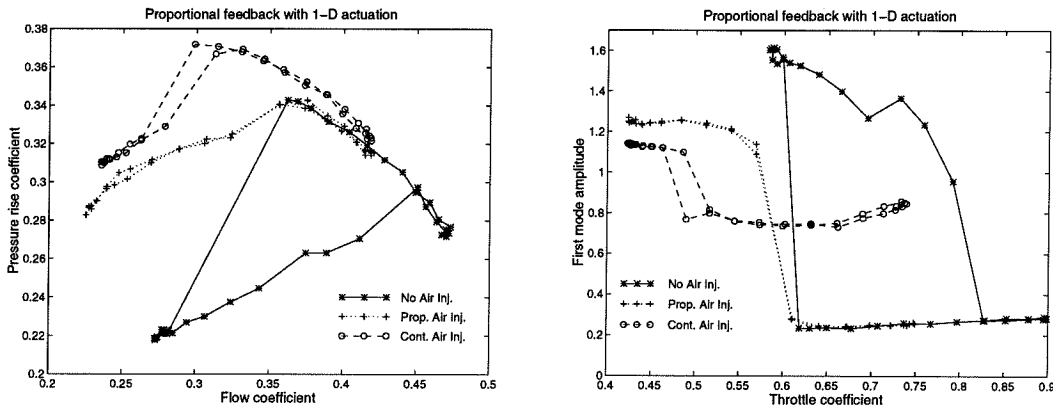
Figure 5.1 Closed loop compressor characteristic and bifurcation diagram, obtained with 1-D proportional feedback: non-overlapping hysteresis case.

Figure 5.1 shows the closed loop compressor characteristic obtained for the non-overlapping hysteresis region case (left of figure), along with an experimental bifurcation diagram (right of figure). The figure clearly shows that the entire nonzero equilibria branch is stable, and there is therefore no hysteresis region associated with rotating stall. This case is in exact agreement with the analytical results of Section 2.3.1.

Figure 5.2 shows the closed loop compressor characteristic obtained for the overlapping hysteresis region case (left of figure), along with an experimental bifurcation diagram (right of figure). The experimental bifurcation diagram shows the effects of saturation described in Section 2.3.1. The hysteresis region is as would be expected from the analysis in that section, but there is one discrepancy which is not accounted for. While the size of the hysteresis region for the closed loop system is as the analysis predicts, no new small amplitude rotating stall solutions were observed (the theory predicts that there should be some prior to transition to rotating stall). One possible explanation for this discrepancy is that the gain for the proportional control was not large enough. The experimental search for these new small amplitude rotating stall equilibria was not exhaustive, and there is room for more investigation of this phenomenon.

It should be noted that the bifurcation diagrams for the continuous air injection case show that the air injection introduces a large amount of non-axisymmetric flow disturbance. This is evident in both the non-overlapping and overlapping hysteresis cases, and is one reason that the active control strategy is better than simply using continuous air injection. In other words, with active injection flow perturbations are introduced only when necessary.

The MG-3 model of control using an axisymmetric compressor characteristic shift behaves very similarly to what was observed in these experiments. This suggests that other control methods which would rely on a compressor performance characteristic shift as a means of active control could be modeled in the same way.
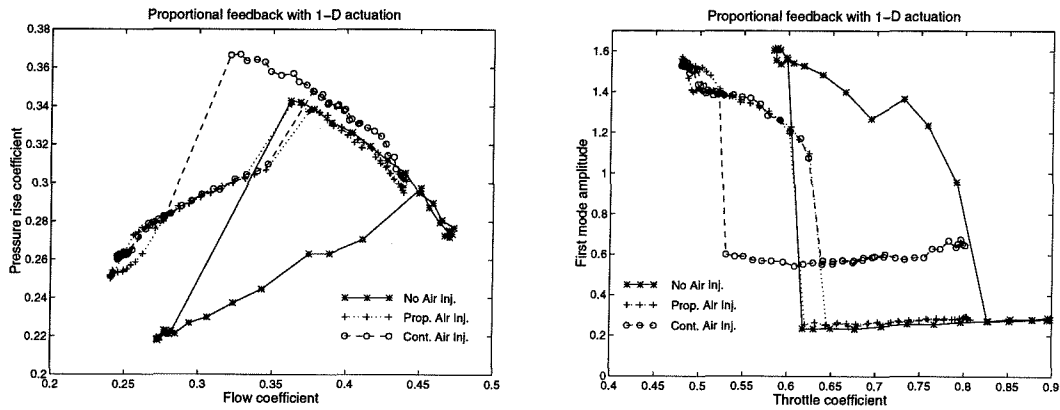
Figure 5.2 Closed loop compressor characteristic and bifurcation diagram obtained with 1–D proportional feedback: overlapping hysteresis case.

The analysis in Section 2.3.1 is general enough that it captures any mechanism for producing the shift from the nonmial compressor characteristic $\Psi_{c_u}(\Phi)$. Some other possible methods of achieving a shift in the compressor characteristic include active casing treatments and hub distortion.

5.2 2–D Rotating Stall Controller

In this section, experimental results on the use of pulsed air injection to control rotating stall are presented. This controller was developed (i.e. the optimal controller parameters were determined) on the Caltech rig in the rotating stall configuration (the configuration shown in Figure 4.1). In this study, optimal refers to the controller which was able to eliminate a growing stall cell the fastest; a more quantitative description of this is presented when the parametric study is described. The effects of this control strategy on the surge dynamics are also explored. Many of the results presented here were previously presented in [7, 8, 9] and represent joint work with Raffaello D'Andrea, but the presentation here includes additional details and investigations.

5.2.1 Optimal placement of air injectors

The experimental results from Section 4.3 and the theoretical results from Section 2.3.1 combine to give a choice for the optimal placement of the air injection actuators. The best choice of actuator geometric parameters is shown in the upper right of Figure 4.7. For that particular configuration, the hysteresis loop size is minimal and the stall point is moved the furthest up and to the left. A more generic sort of shift is shown in Figure 5.3, where the characteristic obtained using continuous air injection at an incident angle of 40 degrees is plotted along with the unactuated characteristic. The most distinct difference between these two cases is that in the
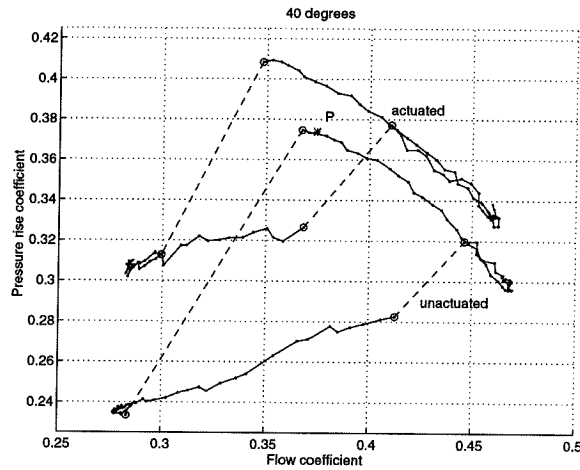
Figure 5.3 Compressor characteristic at air injection angle of 40 degrees.

former the hysteresis regions of the two open loop compressor characteristics do not overlap, and in the later the hysteresis regions do overlap. The operating point P, shown with a * in the figure, is the nominal operating point for the parametric studies presented in Section 5.2.3. In this chapter, closed loop controllers for both the overlapping and nonoverlapping hysteresis regions will be investigated.

5.2.2 Description of control algorithm

The basic strategy of this controller is to sense the location and magnitude of the peak of the first mode component of a circumferential pressure disturbance and inject air based on the location of this first mode relative to the positions of each air injector. The motivation for focusing on only the first mode was the unactuated measurements of the transition to rotating stall presented in Section 4.2.2. The measurements presented there showed that the first mode is the dominant Fourier component during the transition to rotating stall. While the second mode was detectable it was present to a lesser extent. A controller designed specifically for recovery from rotating stall might need to focus on both the first and second modes due to the bistable behavior present in the Caltech rig (see Section 4.2.2).

The action of the controller is parameterized by the following variables:

jeton	minimum pulse width
threshold	threshold for stall detection
window	angle window for stall detection
angle1	activation angle for air injector 1
angle2	activation angle for air injector 2
angle3	activation angle for air injector 3,

and the algorithm itself is shown schematically in Figure 5.4. The flow chart can be interpreted as follows: each air injector is activated when the magnitude of the
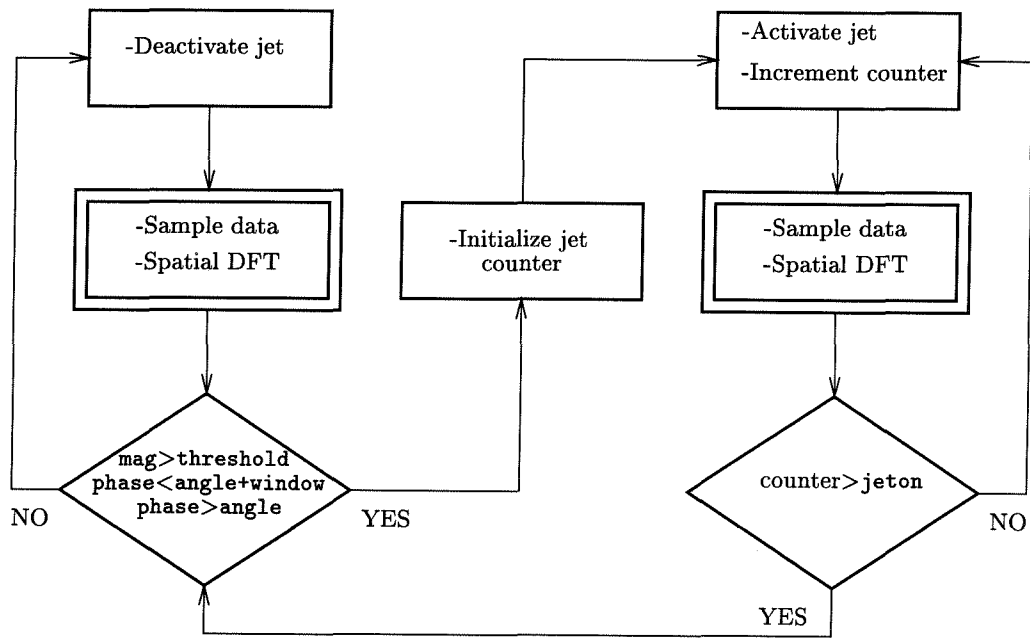
Figure 5.4 Control Algorithm. The above logic is repeated for each air injector. The double rectangle corresponds to the beginning of a servo-loop, which occurs at a rate of 2000 times per second. Figure courtesy of Raffaello D'Andrea.

first mode is greater than threshold and the location of the peak of the first mode is within a pre-specified range of angular positions (as determined by angle and window); once an air injector is activated, it remains activated for jeton number of servo-loops, irrespective of the magnitude mag and location phase of the first mode. Note that phase and mag refer to the phase and magnitude of the first Fourier coefficient, not the physical location and value of the peak pressure disturbance at the compressor face. The higher circumferential modes effect the exact location, but the available pressure sensors only provide the location of the first two modes. In the case that the pressure disturbance is sinusoidal (which is a good approximation when fully stalled), phase and the physical location of the peak pressure disturbance differ only by a constant, which is due to delays in the data acquisition stage.

5.2.3 Parametric search for optimal controller

The parametric search presented here was performed using the air injection geometric parameters that produced the compressor characteristic shift shown in Figure 5.3. Similar results were obtained for other compressor characteristic shifts. The parameters which describe the controller action were varied in order to determine the values that provided the best closed loop performance. The parameters varied were jeton and angle1, angle2 and angle3. For this parametric study, the value of threshold was set to correspond to a pressure rise coefficient of 0.004 (10 Pa), and window was set to 25 degrees.

The value of threshold was selected to be slightly above the noise level in the determination of the stall cell magnitude; this choice allowed the control algorithm to sense a stall cell forming as quickly as possible without introducing chatter.

The value of window was selected to ensure that the peak of the stall cell disturbance would not be missed. If the first mode is assumed to rotate at a constant rate of 65 Hz for all amplitudes (Figure 4.4 shows that this is a reasonable assumption), one servo-loop corresponds to a stall cell rotation of 12 degrees. It was found experimentally that the value of window could be set in the range of 15 degrees to 90 degrees without changing the performance of the controller.

Effect of activation angles

In order to determine the optimal control strategy, for a fixed value of jeton, a search was performed over the activation angle for each air injector. The compressor was operated at point P in Figure 5.3. Parameters angle1, angle2, and angle3 were each varied in 30 degree increments, from 0 to 330 degrees. These ranges gave a total of 1,728 different controllers that were tested for each value of jeton. For each of these controllers, the algorithm was operated for sixteen seconds, while the average size of the stall cell and the amount of time each air injector was on were recorded. A 0.1 second disturbance was generated every second using the high speed bleed valve in order to ensure that the compressor would stall. The sixteen disturbances also decreased the effects that fluid noise introduced into the testing.

The criterion used to determine the optimal setting for angle1, angle2, and angle3 for a fixed jeton was the setting which yielded the lowest value for the

average magnitude of the first mode (other criteria were also investigated, such as the total time that air injectors were on and the average pressure rise across the compressor, and produced roughly the same results).

The results of this parametric study for jeton = 15 are given in Figure 5.5. In the figure shows twelve separate plots; one for each setting of angle1. Dark areas correspond to low average values for the first mode disturbance, while light areas correspond to large average values. These plots show that the optimal setting for angle1, angle2, and angle3 is roughly (90, 210, 330), and that the performance of the control algorithm is insensitive to simultaneous parameter variations of up to 30 degrees from the optimal setting. The white asterisks in the plots correspond to the optimal setting for angle2 and angle3. The corresponding plots for jeton = 11, 13, 17 and 19 are shown in Figure 5.6.

Effect of time delays

In order to understand the operation of the controller, the activation and deactivation delays of the air injectors must be taken into account. Using hot-wire measurements of the velocity profile that the air injectors produce (see Appendix C for further details on these measurements), the average activation delay for each injector was determined to be 6.5 ms, while the deactivation delay was 4.5 ms. The activation delay corresponds to the time difference between when the injected air reaches 50% of its steady state value at the rotor face (which is a distance of approximately 9 cm from the exit of the injector) and the time that the injector is commanded to turn on. This delay includes the time required to open the solenoid valve and the transport delay incurred as the air moves from the injector exit to the rotor face. The deactivation delay corresponds to similar delays that occur when the injector is commanded to turn off. For further information see Appendix C.

If a constant rotation rate of 65 Hz is assumed for the stall cell, then the position of the peak of the stall cell disturbance relative position of the air injector at the valve activation time can be determined. This is depicted in Figure 5.7 for jeton = 15 and air injector 1. The 90 degree rotation corresponds to the experimentally determined optimal lag; the 185 degree lag corresponds to the delay from sensing to actuation; the −30 degree rotation corresponds to the measured physical location where the injected air strikes the rotor face (recall that the air injectors were angled into the blade rotation). Therefore air injector 1 activates approximately 55 degrees before the peak of the pressure disturbance and deactivates 70 degrees after the peak. Since the air injectors were physically spaced 120 degrees apart and the experimentally determined lags for angle1, angle2, and angle3 were also spaced 120 degrees apart, a similar argument holds for air injectors 2 and 3.

The experimentally determined optimal controller can easily be visualized in Figure 5.8. In the figure, the delays described above are taken into account so that the position of the injected air relative to the stall position can be seen. The light region corresponds to an area of higher pressure (stalled region), the boxes represent the position of the injected air, and the stall cell is rotating counter-clockwise. The stall cell position relative to the actuator when the flow from the injector reaches the
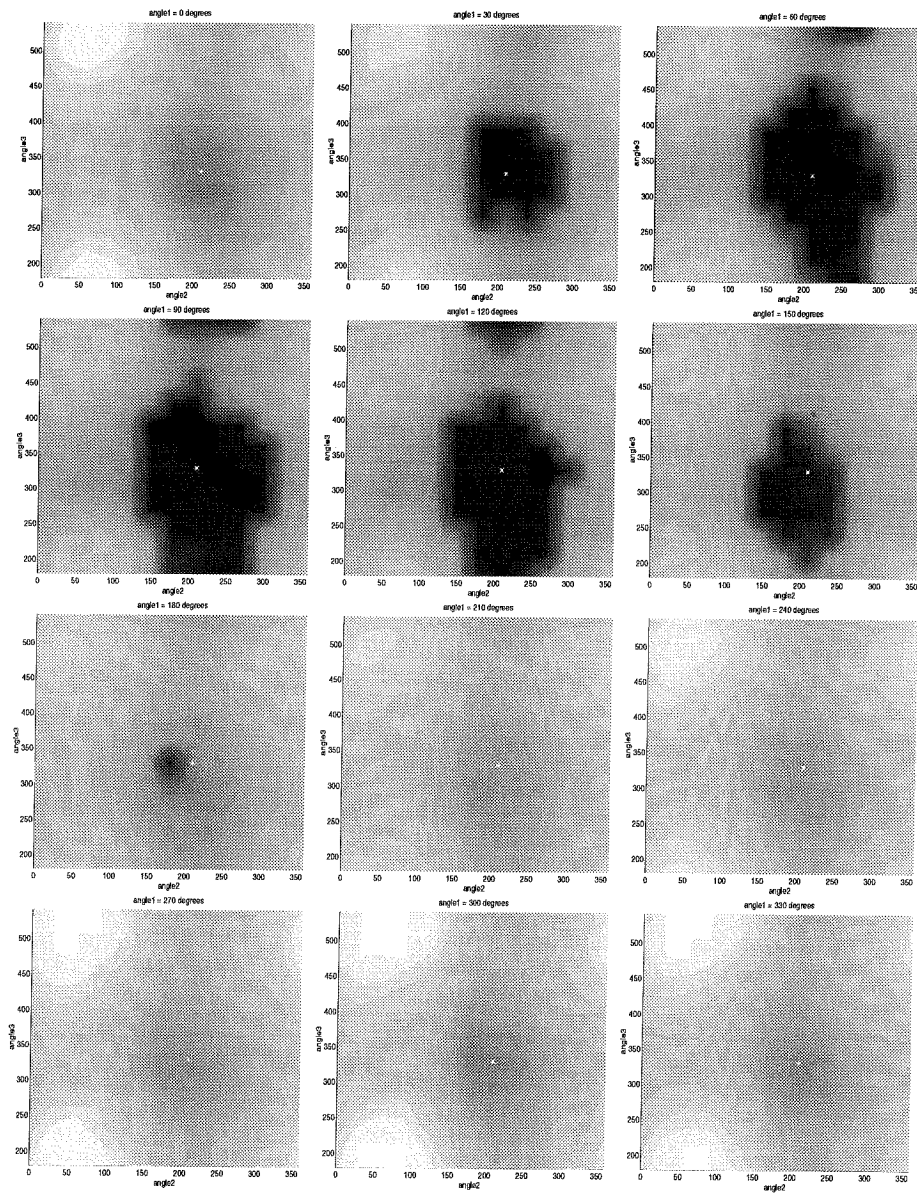
Figure 5.5 Parametric study, jeton = 15. Dark areas correspond to low average values for the first mode disturbance, light areas correspond to large average values. The white asterisk corresponds to the optimal setting for angle2 and angle3, 210 and 330 degrees. Figure courtesy of Raffaello D'Andrea.

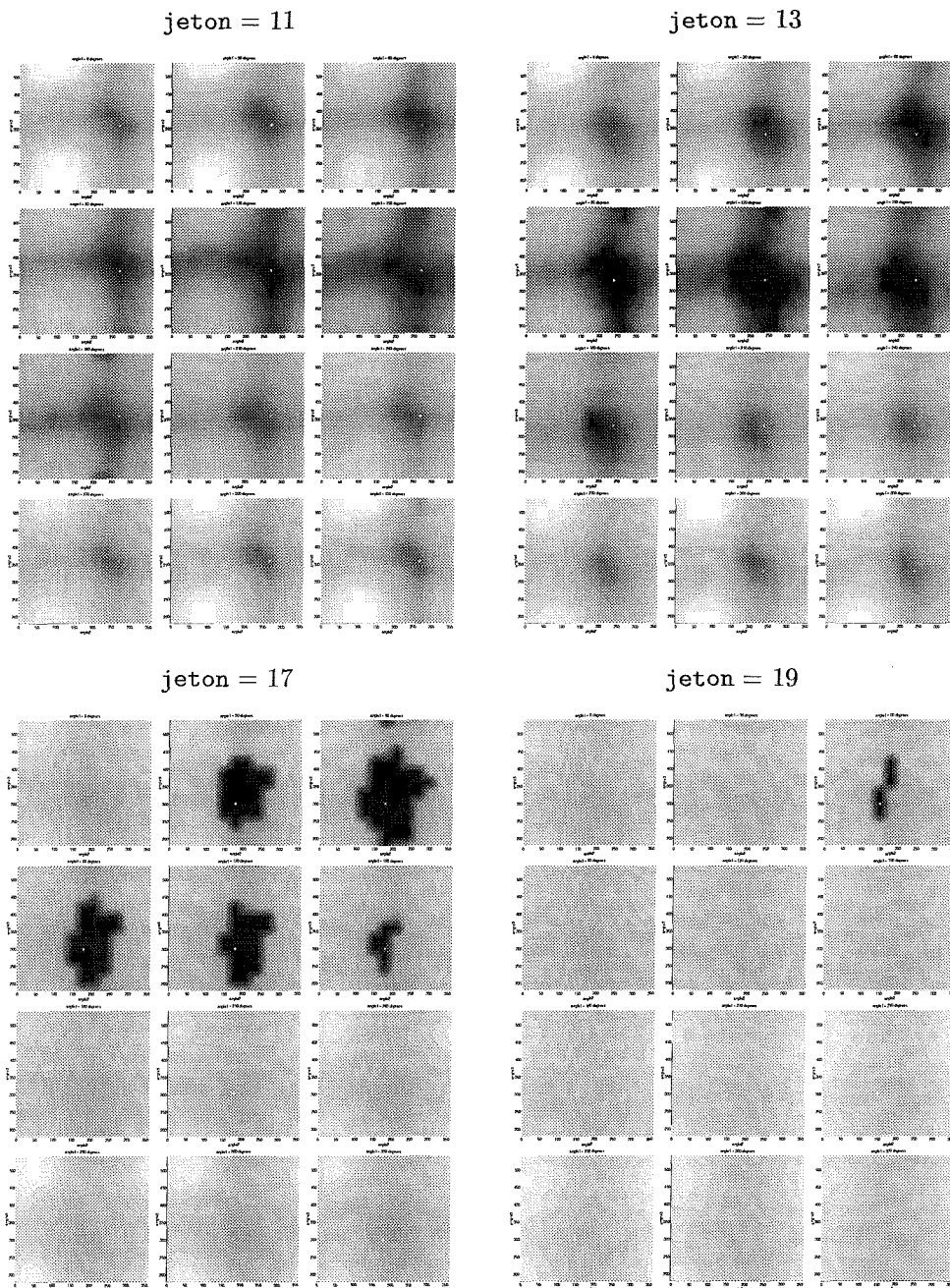**Figure 5.6** Parametric study, results for various values of jeton. Figure courtesy of Raffaello D'Andrea.
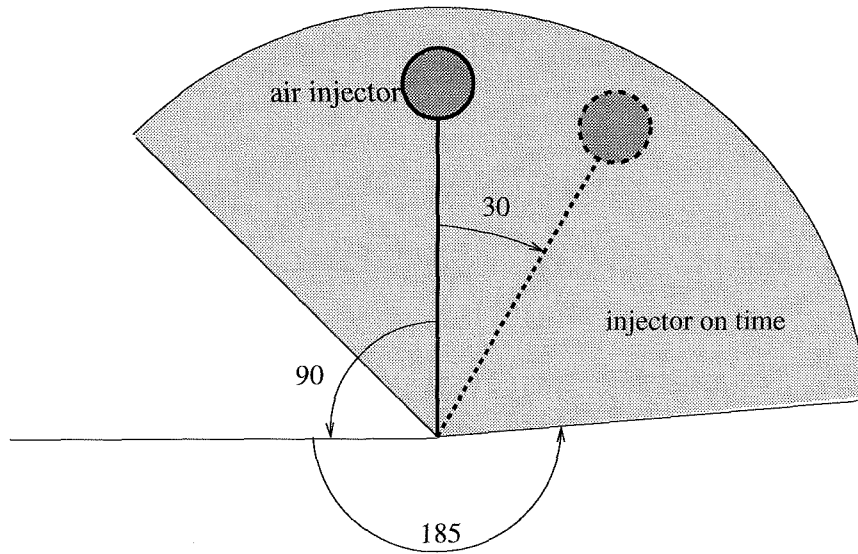
Figure 5.7 Stall cell position relative to air injector position. The shaded region corresponds to the location of the peak of the first mode disturbance for which the air injector is on (assuming a constant stall cell rotational rate of 65 Hz). Figure courtesy of Raffaello D'Andrea.
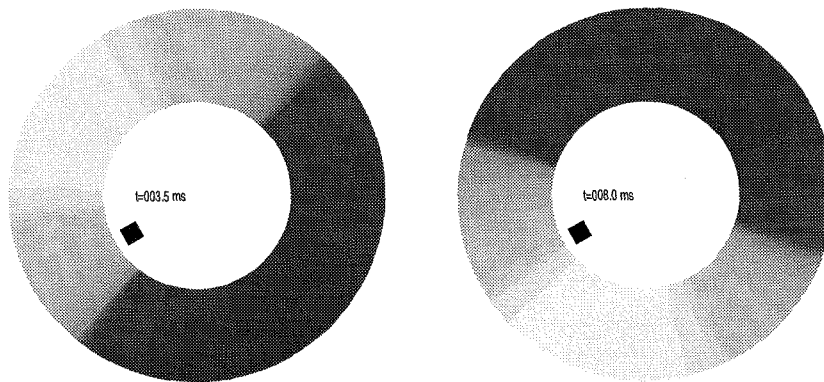

Figure 5.8 Injector Control Law. Light region corresponds to the stall cell (which rotates counterclockwise), figure at left shows stall cell position when the air injector turns on (injector position shown by box) and figure at right shows stall cell position when the air injector turns off.

rotor face is shown on the left and the stall cell position at the instant when the flow from the injector stops reaching the rotor face is shown on the right. Intuitively, the controller attempts to increase the flow in the regions of the rotor which are stalled. It should be noted that the illustrations in Figure 5.8 correspond to actual data.

Effect of pulse width

Experiments showed that for values of jeton less than 10 and greater than 21 the compressor remained stalled all of the time. If the air injector activation and deactivation delays into account, a value of 9 corresponds to approximately 2.5 ms of on-time for each injector, or a window of 60 degrees if the stall cell is assumed to rotate at 65 Hz. This amount of time apparently was not enough to bring the compressor out of stall. A value of 22 for jeton corresponds to approximately 9 ms of on-time for each injector, or about 210 degrees at a rotation rate of 65 Hz. For this value, the air injectors remain active even when the local flow is above the circumferentially averaged value (i.e. when the stalled region has passed).

One way to understand why there should exist an upper and a lower bounds for the value of jeton which eliminates stall is through limiting arguments. Clearly for jeton = 0 (no control), the compressor will transition into stall. When jeton = ∞, the air injection corresponds to the continuously on case shown in Figure 5.3. It was verified experimentally that the throttle disturbance was large enough to cause the rig to stall for the continuous air injection case, and the control law should behave no differently.

Another way to understand why there are minimum and maximum values for which the controller can eliminate the rotating stall cell is by visualizing the first circumferential Fourier mode of the injected air. If the controller is thought of as canceling the first mode of the rotating stall, then the controller will need to have some minimum amount of first mode component. When the injectors are off, there is clearly no first mode component, and when the injectors are all on there is also no first mode component. The optimal controller presented above maximizes the amount of first mode flow perturbation that three air injectors can produce.

Experimental investigation of the optimal controller

Experimental investigations of the optimal pulsed air injection controller presented above are described here. Transient measurements of the control law rejecting growing stall cells is presented.

A typical disturbance rejection by the pulsed air injection controller using the optimal parameter choices is shown in Figure 5.9. The figure shows time traces for three of the six annular pressure transducers, the amplitudes of the first two Fourier modes, the three air injector command signals, and the pressure rise delivered by the compressor. The figure shows that during the rejection of a developing stall cell the pressure rise coefficient drops by approximately 20% of the pressure rise developed at the nominal operating condition and then recovers. It can also be seen in the time traces of the annular pressure transducers that the controller drives the energy of the first mode rotating stall into a high frequency "surge-like" oscillation. This
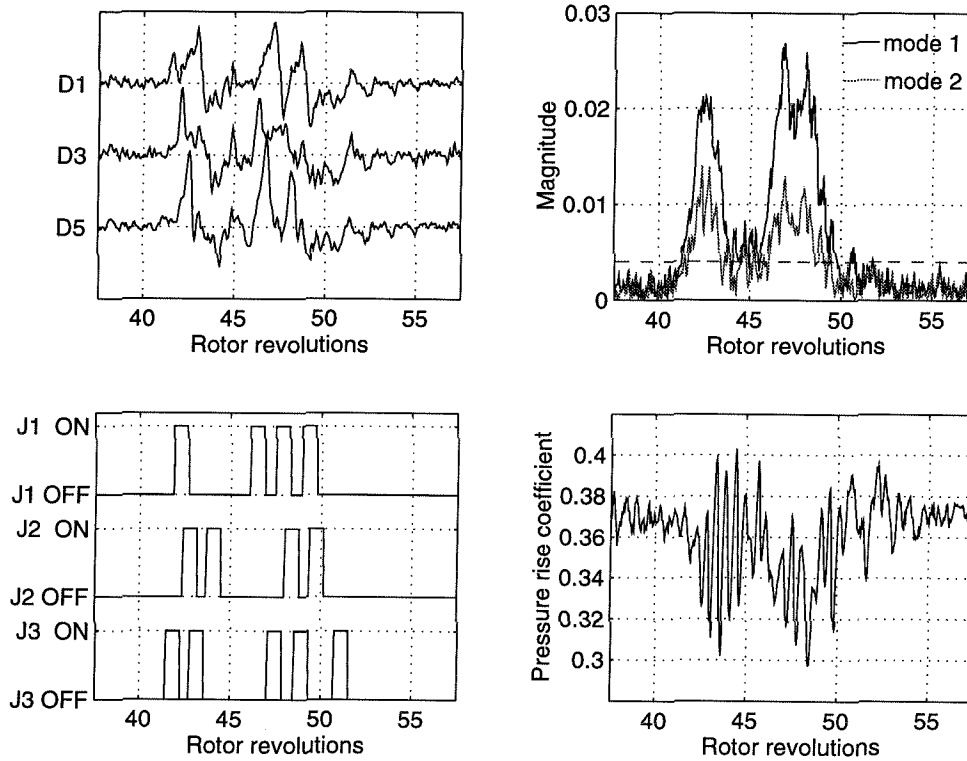
Figure 5.9 Time traces of closed loop operation. The upper left plot shows the output of three pressure transducers space 120 degrees apart in the compressor annulus. The lower left plot consists of the control signals applied to the air injectors. The upper right plot consists of the calculated first and second spatial Fourier mode magnitudes; the dashed line corresponds to the setting for `threshold`. The lower right plot consists of the variation in the pressure rise coefficient.
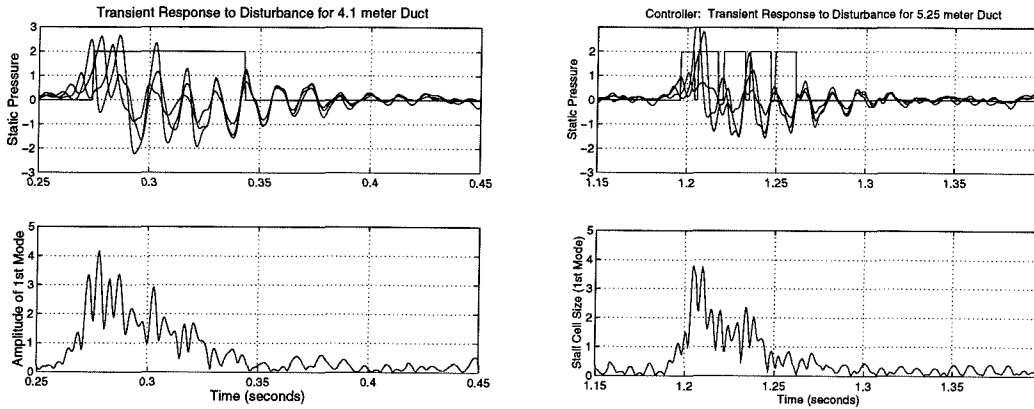
Figure 5.10 Comparison of surge-like ringing for different duct lengths.
Rotating stall is driven into acoustic mode of duct.

oscillation corresponds to the acoustic frequency of the ducting on the Caltech rig.
Figure 5.10 shows time traces of controller transients of the rig in the rotating stall
configuration with different total lengths of ducting. The upper plots correspond to
time traces of three pressure transducers spaced 120 degrees around the compressor
annulus, and the lower plots show the amplitude of the first spatial Fourier mode
computed from the three pressure transducers. The square waves denote air injector
controller action. The acoustic mode in the upper two plots are characterized by the
three pressure transducer time traces being in phase (for first mode rotating stall
the transducers are 120 degrees out of phase). The figure shows the disturbance be-
ginning as a non-axisymmetric perturbation, which is characteristic of rotating stall,
and then transitioning into an axisymmetric perturbation before dying completely
away. The frequency of the axisymmetric perturbations which occur at the end of
the disturbance transient were found to correspond to the acoustic frequencies for
ducts of the lengths shown in the figure.

Closed loop compressor characteristic

The closed loop compressor performance curve is shown in Figure 5.11 for the op-
timal choice of injector phasing and jeton = 15. The results shown to the left
of the peak of the characteristic are time averaged values, since the controller is
continuously rejecting stall disturbances in this region. Error bars are included to
show the time variation of the circumferentially averaged flow and the pressure rise
coefficients at these unsteady operating points (this is because the system is contin-
uously rejecting rotating stall disturbances in this region). The figure shows that
hysteresis loop associated with rotating stall is eliminated by the pulsed air injection
controller.

The closed loop compressor characteristic shown in Figure 5.11 resulted from
performing the above control algorithm with the air injectors placed in a configu-
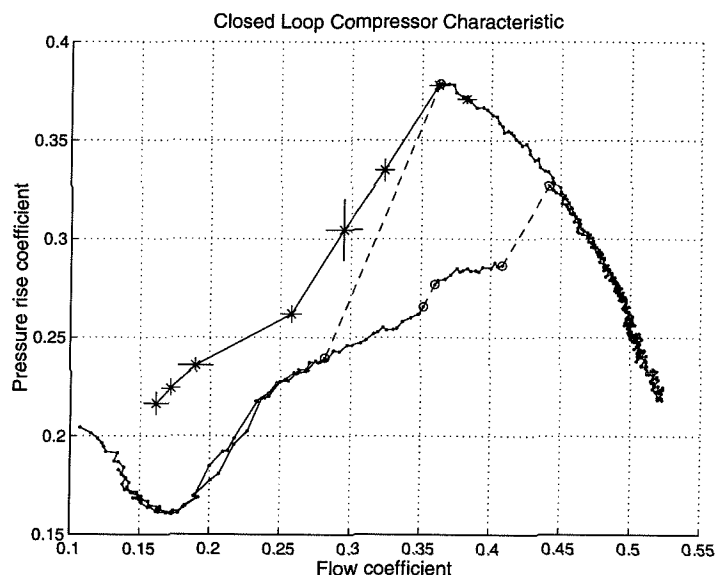ration that produced the shift in the compressor characteristic shown in Figure 5.3

Figure 5.11 Closed loop compressor characteristic for jeton = 15, optimal controller. The asterisks correspond to time averaged data, while the solid lines interpolate these points. The pressure and flow variance are included for each data point as error bars. The open loop compressor characteristic is included for comparison purposes.

when continuous air injection was applied.

In addition to the closed loop compressor characteristic for the optimal controller presented above, the closed loop characteristic for a case where the placement of the air injectors resulted in non-overlapping hysteresis regions for the continuous air injection and the uninjected case was determined. Using the air injection geometry which produced the shift shown in the upper right of Figure 4.7 produced the closed loop characteristic shown in Figure 5.12. The only difference that is apparent between two closed loop compressor characteristics is that the case with non-overlapping hysteresis regions has a less step dropoff in pressure rise as the throttle is closed past the peak of the compressor characteristic. From these results it is clear that shifting the characteristic to the point where the hysteresis regions do not overlap does not provide significant benefit for this form of controller.

Figure 5.13 shows the transient behavior at two points (A and B) on the closed loop compressor characteristic shown in Figure 5.12. The figure shows the unsteadiness associated with operating the closed loop system to the left of the compressor characteristic peak (point B). Again, there are no significant differences between this case and the overlapping hysteresis case. The fact that non-overlapping hysteresis regions were not required to eliminate the hysteresis associated with rotating stall (this was not the case for the 1–D proportional controller presented in Section 5.1) is a strong motivation to investigate this and other 2–D actuation schemes further.
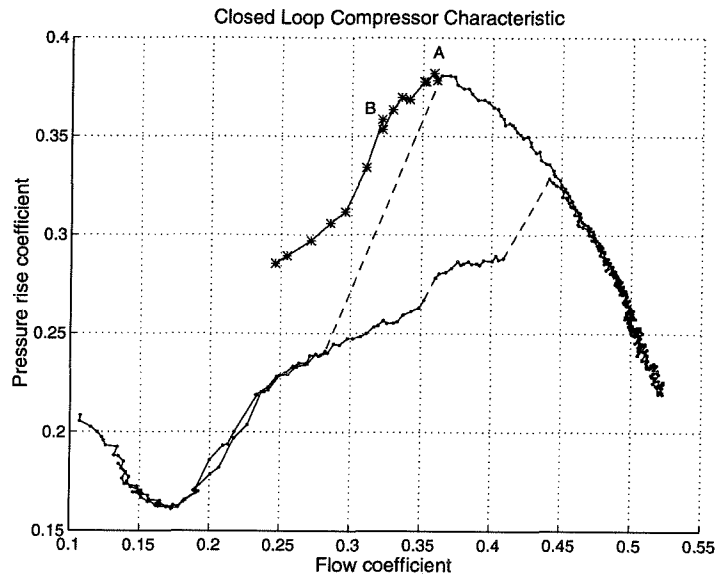
Figure 5.12 Closed loop performance characteristic for air injection geometric parameters which provide no overlap of the hysteresis regions.

5.2.4 Pulsed air injection control in the presence of surge dynamics

Several experiments were performed to determine the effect of the control algorithm when the rig was operated in the surge configuration, and the results are shown in Figure 5.14. At operating point P (see Figure 4.3), a throttle disturbance lasting 20 rotor revolutions (0.2 seconds) was generated using the high speed bleed valve. Data for the uncontrolled case is shown in the top four plots of Figure 5.14 for reference.

The plots of the uncontrolled case show two different surge modes, one at 1.4 Hz and the other at 1.8 Hz (these two different surge modes are investigated further in Chapter 6). The time traces for the first mode rotating stall clearly show that the compressor goes into stall during the low flow rate intervals and comes out of stall during the high flow rate intervals. The pressure rise coefficient versus flow coefficient plot clearly illustrates the two different surge limit cycles (note that the surge cycles are traversed in a counterclockwise direction).

The bottom four plots show the transient behavior of the compression system when the pulsed air injection controller for rotating stall is active. The plots show the response to a single throttle disturbance. As in the uncontrolled case, each pressure disturbance de-stabilized the system. Note that the controller had virtually no effect on the surge trajectory during the time the disturbance was present (in this 20 revolution time period, the trajectory is virtually the same as the one in the previous experiment). On the subsequent cycle the pressure and flow variations were substantially decreased and then eliminated. Experiments showed that by shortening the time duration of the pressure disturbance (while still keeping it large enough to cause the open loop system to go into surge), the pressure and flow
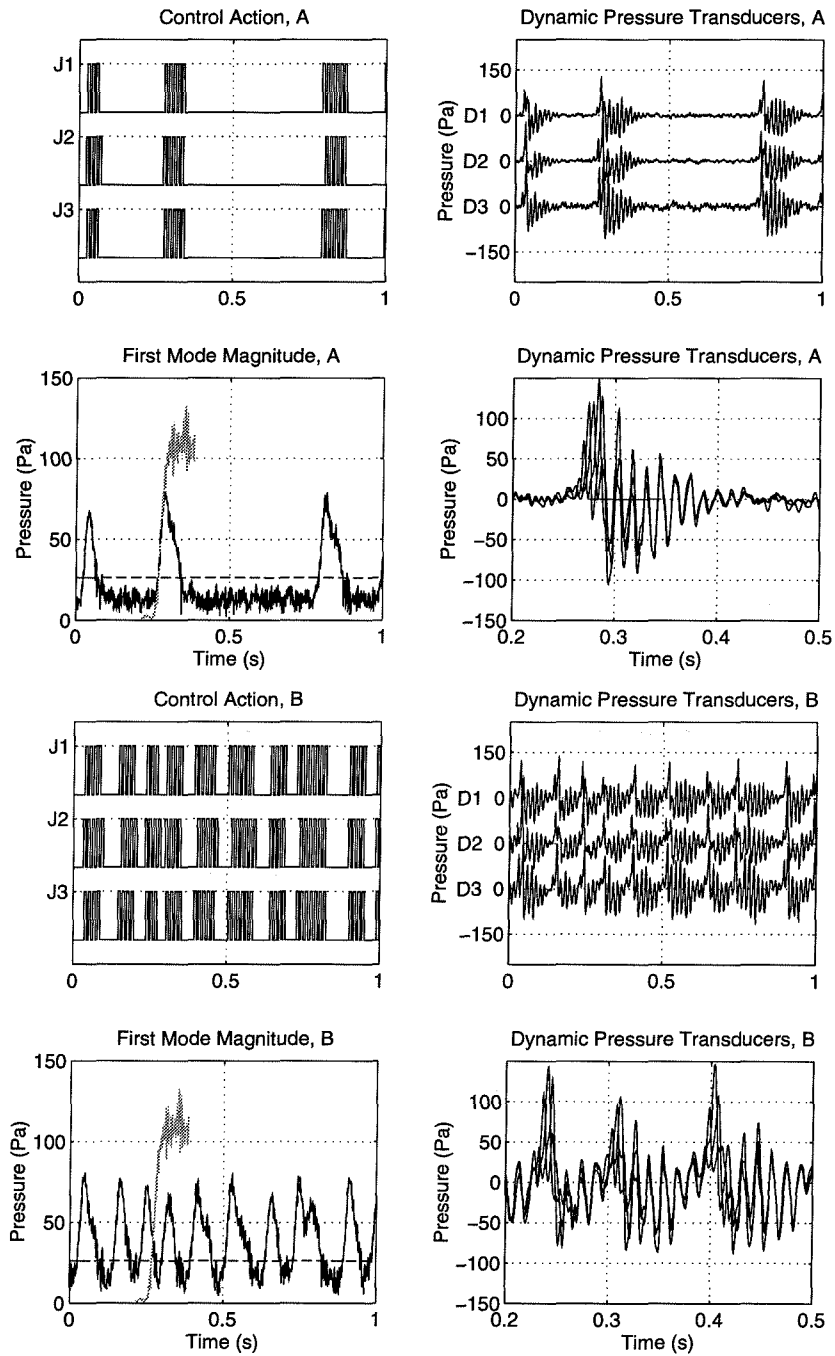
Figure 5.13 Comparison of controller performance for two different throttle settings. Points A and B refer to the operating points shown previously in Figure 5.12. The first mode stall cell amplitude for the uncontrolled case is shown in gray. Figures courtesy of Raffaello D'Andrea.
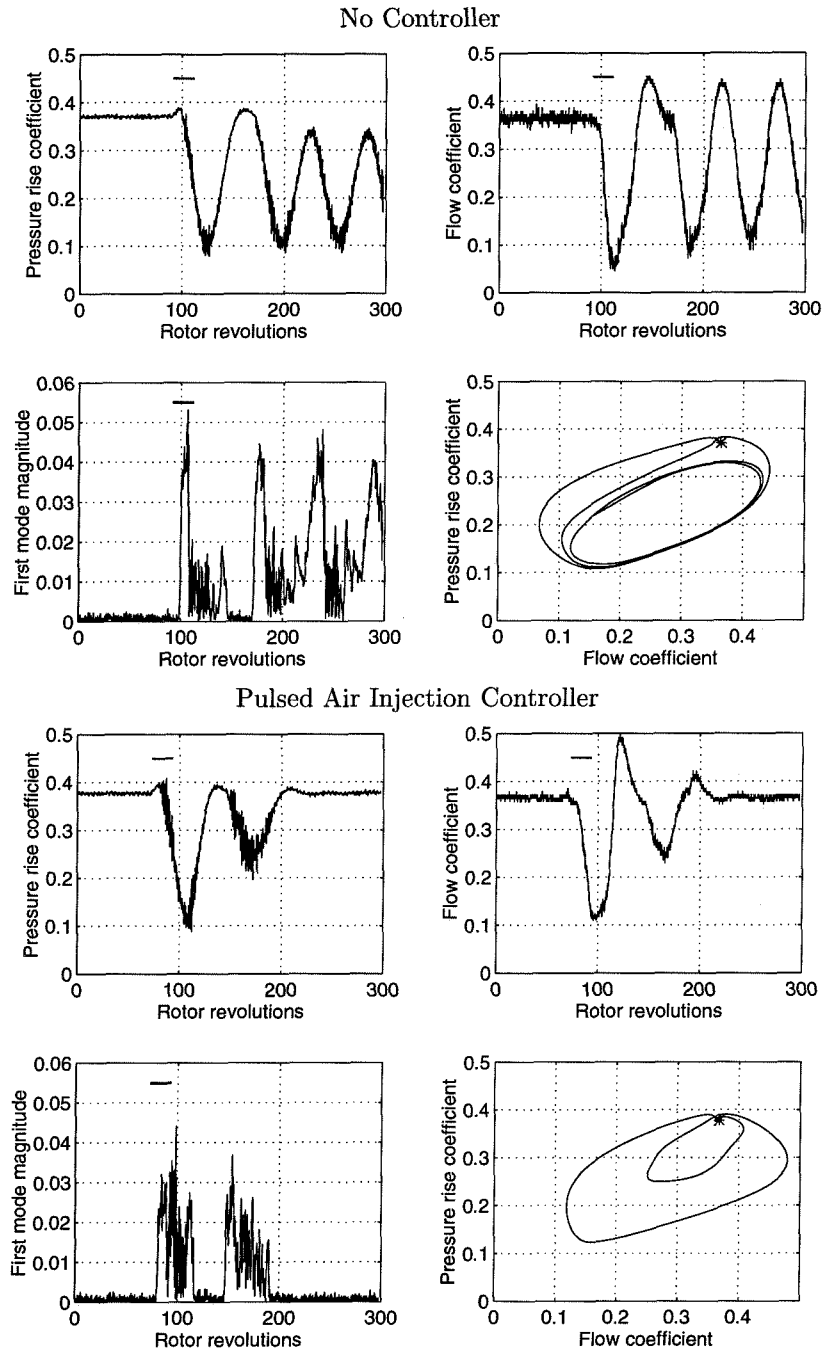
No Controller

Pulsed Air Injection Controller

Figure 5.14 Effects of pulsed air injection controller on the surge dynamics. The top four plots correspond to no control action, and the bottom four plots correspond to pulsed air injection control. The horizontal line in the time trace plots corresponds to the throttle disturbance on time.
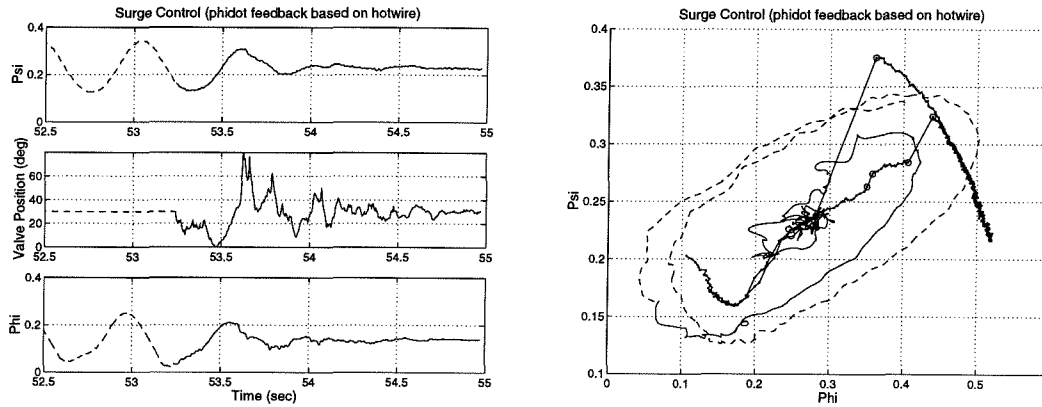
Figure 5.15 Bipolar closed loop throttle controller for surge. The dashed line corresponds to no control action, and the solid line corresponds to the controlled case.

variations during the first cycle were reduced. For short disturbances, the magnitude of the pressure and flow disturbances could be kept to within 30% of the nominal operating flow and pressure rise.

An explanation of why the control algorithm is successful at eliminating surge is based on the strong coupling between the surge and stall dynamics. Since the compressor begins to stall when the flow coefficient is decreasing, the stall controller can react to this aspect of the surge dynamics. When the system begins to stall, the control algorithm activates, and tries to eliminate the stalled condition. This has the effect of increasing the net flow rate through and pressure rise across the compressor when these states are low during a surge cycle. The control algorithm therefore provides positive damping to the surge dynamics.

5.3 Bleed Valve Control of Surge

The previously described rotating stall controller was experimentally developed using the rig in a configuration where surge does not occur. If the rig is operated in the surge configuration, then the surge dynamics must also be controlled. A controller which has previously been shown to stabilize the surge dynamics by Eveker et al. [15] and by Badmus et al. [4] is given by:

$$\gamma = \gamma_0 + k_2 \dot{\Phi}, \tag{5.2}$$

where k_2 is a negative constant. The reason that this sort of controller stabilizes surge was investigated in Section 2.4.

Figure 5.15 shows the experimental results from implementing this controller on the Caltech rig. The figure shows that the system recovered from a full amplitude surge (the worst case disturbance) in less than one complete cycle. The final operating point is a new equilibria corresponding to rotating stall. Note that the signal for
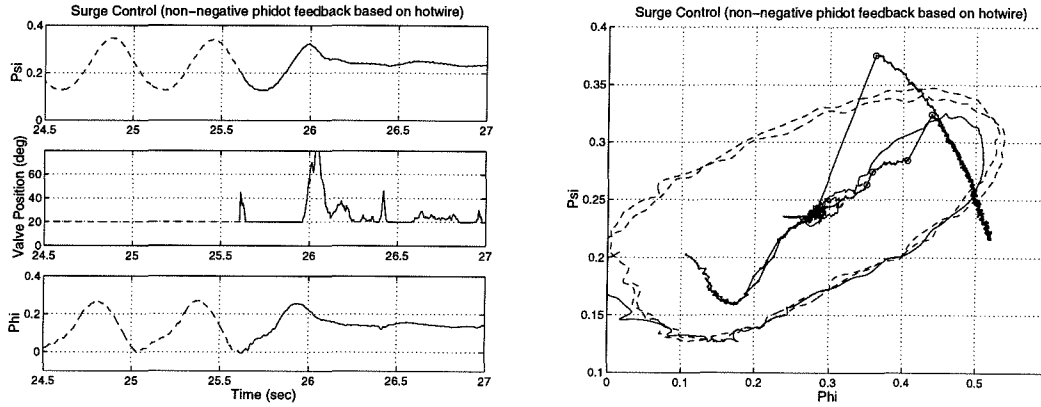
Figure 5.16 Unipolar closed loop throttle controller for surge. The dashed line corresponds to no control action, and the solid line corresponds to the controlled case.

$\dot{\Phi}$ was obtained using a hotwire anemometer in the inlet duct, and performing the differentiation using a digital filter. Other signals for the feedback (such as $\dot{\Psi}$ and the time derivative of the static pressure in the inlet duct) were also implemented and the results were similar.

In addition to implementing the controller described above for surge, a slightly different controller was also investigated. In this case, the value of k_2 was not a fixed constant, but had a value of zero when $\dot{\Phi} > 0$ and a negative value when $\dot{\Phi} < 0$, i.e.

$$k_2 = \begin{cases} 0 & \text{if } \dot{\Phi} \geq 0 \\ \text{negative constant} & \text{if } \dot{\Phi} < 0 \end{cases}. \tag{5.3}$$

This form of controller has the advantage of leaving the valve closed (no air is bleed off to atmospheric pressure) when the rig is operating under normal conditions. The results of using this sort of controller are presented in Figure 5.16. The figure shows that the recovery from fully developed surge takes less than on surge cycle, and that the controller performance is not significantly different than the previous case.

This nonnegative (unipolar) control strategy is the sort that would be used on an actual jet engine compressor, since it is obviously not efficient to dump some of the pressurized flow to atmosphere unless it is absolutely necessary. Experimentally this unipolar controller required a gain twice as high as that required for the bipolar case presented above, which is as would be expected since energy can only be pulled out of the surge cycle during half of the orbit.

5.4 Combined Control of Rotating Stall and Surge

The previously described air injection controller for rotating stall and bleed valve controller for surge were combined. The motivation for this combination was described in Section 2.4, and is that since the rotating stall dynamics occur on a much
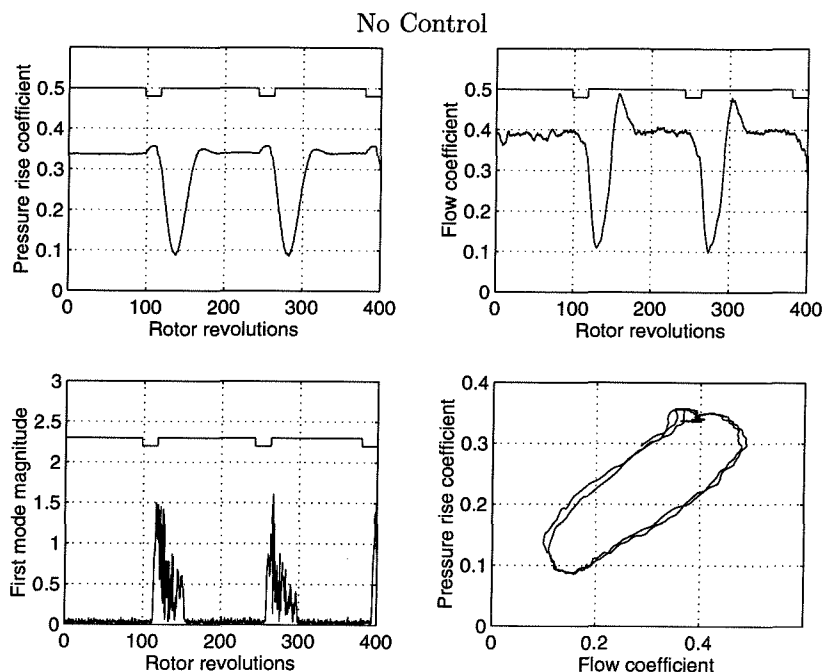
No Control

Figure 5.17 Open loop system response to throttle disturbance. The throttle disturbance occurs when the square waves in the time traces are low.

faster time-scale than the surge dynamics, the controller design for each aspect can be decoupled.

Since the surge controller alone removes the surge oscillations but leaves the system in a new rotating stall equilibria, some sort of rotating stall controller is of course required. In previous work by Eveker et al. [15] the rotating stall was controlled using the feedback proposed by Liaw and Abed [30]. In this case the rotating stall was controlled with the previously described pulsed air injection controller. Figure 5.17 shows response of the uncontrolled system to a throttle disturbance, and Figure 5.18 shows a comparison between the air injection controller for rotating stall alone, and the combined bleed valve surge/air injection rotating stall controller. In both figures a square wave shows the presence of the throttle disturbance in the pressure rise and flow coefficient time traces; the disturbance is active when the square wave is low. The combined case corresponds to using optimal air injection control strategy presented in Section 5.2 and the bleed valve controller for surge presented in Section 5.3. The figure shows that the combined surge/rotating stall controller has the minimum amplitude of the flow and pressure rise coefficient fluctuations, which are roughly half the size of those obtained using the air injection controller alone. The combined surge/rotating stall controller does have slightly more ringing in the pressure rise and flow coefficients for the choice of gains presented in Figure 5.18. For a complete engine system (i.e. if a combustor
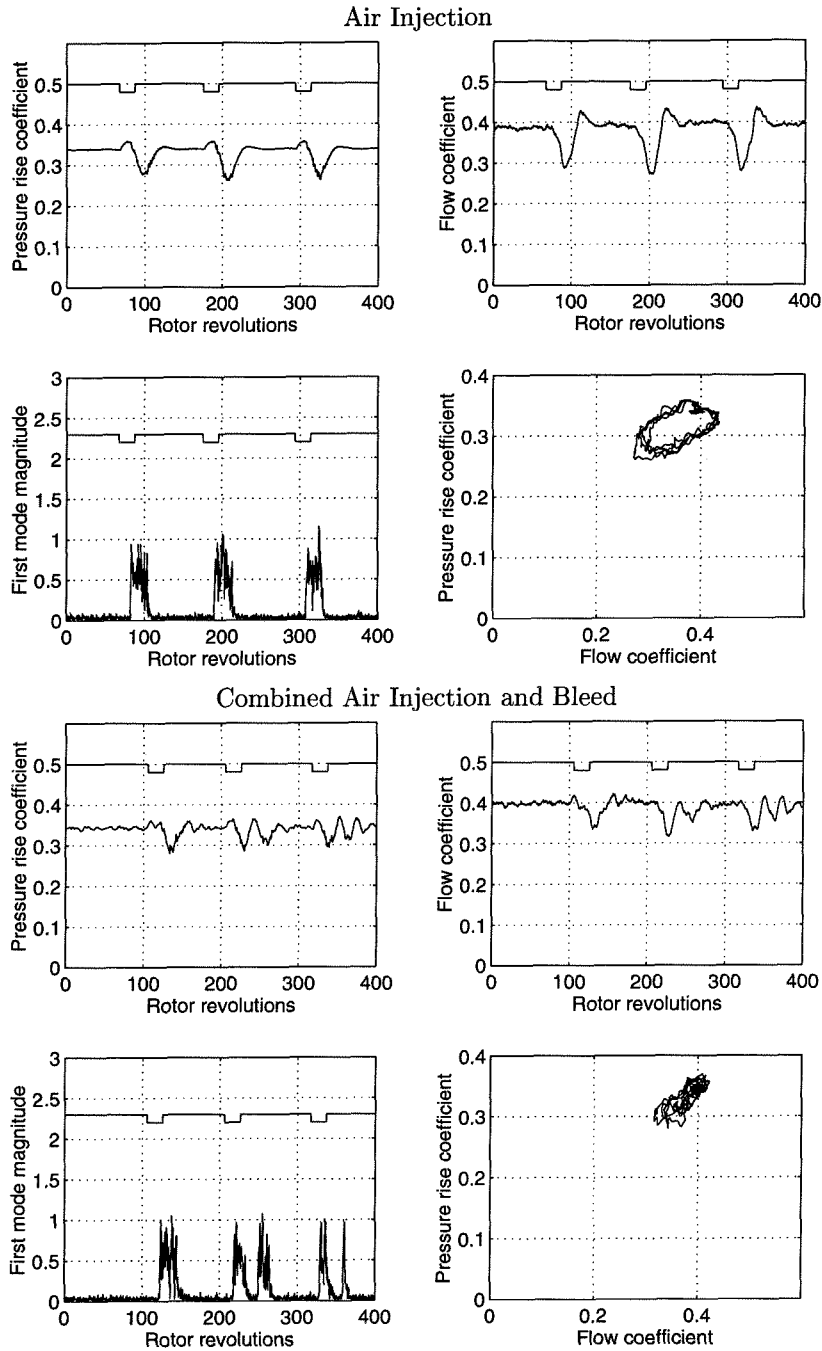
Figure 5.18 Combined air injection controller for rotating stall and bleed valve controller for surge compared with the pulsed air injector controller. The throttle disturbance occurs when the square waves in the time traces are low.

and turbine were included), these effects may be problematic, and a different set of gains may be desirable. These experiments clearly show that under some conditions the controller designs for rotating stall and for surge can be decoupled (as was suggested in Section 2.3.1).

Chapter 6

Identification and Validation

Until recently there has been little interest in the exact shape of the compressor characteristic performance curve, $\Psi_c(\Phi)$, at flow rates lower than that at which rotating stall or surge occurs (the unstable region for zero rotating stall). This has been primarily because the operating region was well to the right of this point (in the stable region for zero rotating stall). In order to develop models that accurately capture the transition into rotating stall, where the flow rate through the compressor is locally to the left of the peak of $\Psi_c(\Phi)$, the exact shape of the unstable portion of $\Psi_c(\Phi)$ must be known. This is easily seen in the MG–3 model by looking at the $\dot{J}$ dynamics, where $\frac{\partial \Psi_c}{\partial \phi}$ dictates the linear stability of the zero amplitude rotating stall solution, and therefore the slope of $\Psi_c(\Phi)$ must be known to determine the time evolution of J (where J is the square amplitude of the first Fourier mode of rotating stall, see Section 2.2 for further details).

In addition to open loop modeling, as active control is used to extend the operating region nearer to the unstable portion of the characteristic, the exact shape of this portion becomes more important. This shape becomes particularly critical as controllers are expected to reject disturbances that carry the system into the unstable region. The two main reasons to develop higher fidelity models for the behavior of compression systems are therefore to accurately capture the surge and rotating stall type oscillations (open loop matching) and to design controllers which avoid entering the unstable region "too much" (closed loop matching).

Previous work in identifying the unstable region of the compressor characteristic involved trial and error combined with considerations of what the basic shape the function $\Psi_c(\Phi)$ should be. The process involved matching simulation output for stall cell growth to experimental time traces of the same. Very good agreement between experiments and simulations for this technique were presented by Mansoux et al. [31], but only after substantial simulation [37]. It is also not clear from this sort of model matching that there is only a single solution for the compressor performance curve.

In this work, more systematic ways for determining the unstable region of $\Psi_c(\Phi)$ are presented. The first method is based on experimental data taken over surge cycles. This *dynamic correction* of compressor characteristic measurements was first suggested by Greitzer and Moore in [20]. Here multiple surge cycles were used to obtain uncertainty information about the final values for the map $\Psi_c(\Phi)$. This sort

of systematic way of backing out the compressor characteristic curve is important for any sort of model based control design, because it helps to give information on the robustness of the final control strategy and because it greatly decreases the model identification time. Another systematic method is investigated to identify parameters for the Caltech rig when it is operating in configurations which do not surge. This method involves measuring the system response to step changes in the operating point. The transient response of the compression system was recorded for throttle changes which did not excite rotating stall and was used to obtain values for rig parameters. Further work is presented which outlines an attempt to measure $\Psi_c(\Phi)$ directly by making measurements of the flow and pressure rise coefficients directly across a compressor stage.

Together these three techniques reduce the amount of trial and error simulations that need to be performed in order to develop a model for an axial flow compression system. This is of particular interest for the Caltech compressor rig where the system is often physically changed to the point where re-identification could be required.

Finally, the proposed identification scheme is applied to the output from distributed model simulation in order determine how much error is introduced by using the MG–3 model for identification of a much higher order system. This allows the sensitivity of the algorithm to parameter changes to be investigated, in particular, the sensitivity to changes in parameters which are fixed on the experimental rig and which do not appear in the MG–3 model but are included in the distributed model.

6.1 Experimental Apparatus Configuration

As was previously described in Chapter 4, the Caltech rig can be operated in both a stall configuration and a surge configuration, the difference between the two cases being the presence of a 1.81 m^3 (64 ft^3) plenum between the outlet duct static pressure ring and the bleed valve (see Figure 4.1). For the identification schemes presented here, the rig was operated in the surge configuration for the identification scheme involving surge cycle data and in the rotating stall configuration for the step response testing and during the local measurements of the compressor characteristic.

6.2 Identification Using Surge Cycle Data

Experimental data over surge cycles provides a rich source of information about the pressure rise delivered by the compressor as the flow rate through the system is varied. Since surge is a self excited limit cycle, no forcing actuator is required, as would be needed, for example, to perform step response testing. If a model for the compression system transient behavior is assumed, then information about the dynamic response parameters is present, as well as the static compressor characteristic map. This sort of experimental data is also relatively easy to collect because the surge dynamics occur in the 1-2 Hz. range. In this section the Moore-Greitzer surge model is combined with experimental data from surge transients to determine rig parameters and the compressor performance map.

Rotating stall is neglected in this first identification stage in order to gain information as to what level of model needs to be used to fully capture the rotating stall. The results from performing the identification with the surge model will be the effective compressor characteristic, first described by Moore and Greitzer in [35]. The shape of this effective compressor characteristic will be used to determine what number of rotating stall modes needs to be included in the identification model in order to capture the dynamics of the Caltech Rig.

6.2.1 Pure surge

The Moore-Greitzer equations of motion for the compressor system without rotating stall (pure surge) are given by

$$\dot{\Psi} = \frac{1}{4l_c B^2}(\Phi - \gamma\sqrt{\Psi}) \tag{6.1}$$

$$\dot{\Phi} = \frac{1}{l_c}(\Psi_c(\Phi) - \Psi), \tag{6.2}$$

where Ψ is the pressure rise coefficient, Φ is the flow coefficient, and l_c and B are parameters that depend on the compressor. If there were no rotating stall present during the surge cycle, the result of plotting experimental data for the solution of equation (6.2) for $\Psi_c(\Phi)$ would be the compressor characteristic. If rotating stall is present, the result would be referred to as the stalled or effective compressor characteristic.

If experiments could be performed in which the compressor system exhibited pure surge, then the compressor characteristic $\Psi_c(\Phi)$ (as well as the parameters l_c and B) could be computed using equations (6.1) and (6.2). One method which could be used to do this would be to assume a polynomial expansion for $\Psi_c(\Phi)$ and construct two least squares problems based on the experimental data. Choosing $\Psi_c(\Phi)$ to be a nth order polynomial

$$\Psi_c(\Phi) = a_0 + a_1\Phi + \cdots + a_n\Phi^n, \tag{6.3}$$

the following two standard linear least squares problems can be formulated:

$$\dot{\Psi} = \begin{bmatrix} \Phi & -\sqrt{\Psi} \end{bmatrix} x_1, \tag{6.4}$$

$$\dot{\Phi} = \begin{bmatrix} 1 & \Phi & \cdots & \Phi^n & -\Psi \end{bmatrix} x_2 \tag{6.5}$$

where x_1 and x_2 are unknown column vectors given by

$$x_1 = \begin{bmatrix} \frac{1}{4l_c B^2} \\ \frac{\gamma}{4l_c B^2} \end{bmatrix} \qquad x_2 = \begin{bmatrix} \frac{a_0}{l_c} \\ \frac{a_1}{l_c} \\ \vdots \\ \frac{a_n}{l_c} \\ \frac{1}{l_c} \end{bmatrix}. \qquad (6.6)$$

Experimental data would be used to determine the transient values of Ψ and Φ, and $\dot{\Psi}$ and $\dot{\Phi}$ would be determined by an appropriate filter.

Figure 6.1 shows typical experimental data for the Caltech compressor rig during a series of surge cycles. The data was collected at 2000 Hz (the high sample rate was so that the rotating stall development could also be captured for later use) using a hotwire anemometer in the upstream duct and pressure transducers in the inlet and outlet ducts. The values of $\dot{\Psi}$ and $\dot{\Phi}$ were determined after the data was collected by using digital filters. A striking feature of the data is that there are two distinct limit cycles for surge present. The difference between the two cycles is the amount of rotating stall present. The larger of the two cycles has rotating stall occurring over portion (two thirds) of its orbit and no rotating stall occurring over the remainder of the orbit. The smaller cycle is dominated by rotating stall over the entire orbit. The amplitudes of the first two modes of rotating stall over the surge cycles are also shown in Figure 6.1.

The identification procedure described above was performed for the data set shown in Figure 6.1; the resulting compressor characteristic is shown in Figure 6.2. This "dynamically corrected" characteristic curve was obtained by solving equation (6.2) for $\Psi_c(\Phi)$. This method provides values for the overall duct length parameter, l_c, and the Greitzer stability parameter, B [18]. Ideally these terms would be determined separately from the compressor characteristic identification process, but it is not clear how this could be done. Direct measurement of the geometry of the Caltech rig gives approximately B=0.35, using the following relationship from [18]:

$$B = \frac{U_r}{2a} \sqrt{\frac{V_p}{A_d L_d}}, \qquad (6.7)$$

where U_r is the rotor tip speed, a is the speed of sound, V_p is the volume of the plenum, A_d is area of the duct, and L_d is the length of the duct. This value for B gives a surge oscillation frequency which is about twice as fast that obtained from the experiment. This is partially explained by the flexibility associated with the walls of the plenum installed on the Caltech rig, but inclusion of these effects in the computation of B is not straightforward. The two different surge limit cycles also make the determination of the appropriate surge oscillation frequency difficult. Actually, equation (6.7) applies to a surge cycle without the presence of rotating stall, which is not observable on the Caltech rig.

The least squares fit results are plotted in Figure 6.2 along with the experimental
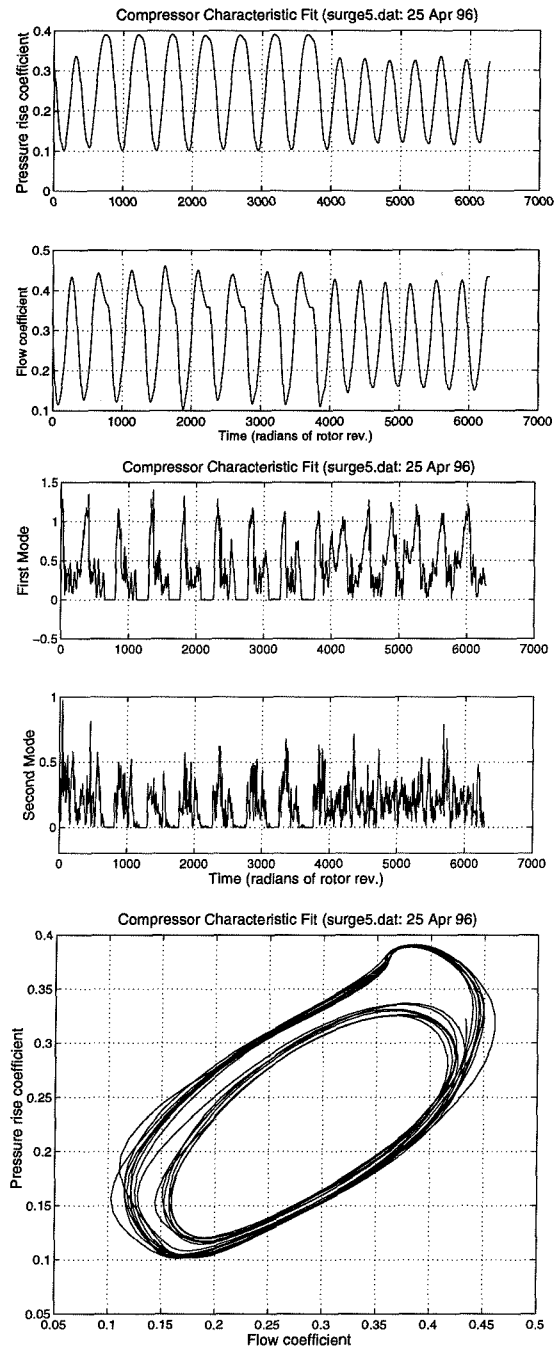
Figure 6.1 Experimental data from a series of surge cycles on the Caltech compressor rig. The graph at the top show time traces of the pressure rise and flow coefficients, the middle plot shows the modal amplitudes of static pressure perturbations at the rotor face, and the graph at the bottom shows the data in the Φ-Ψ plane.
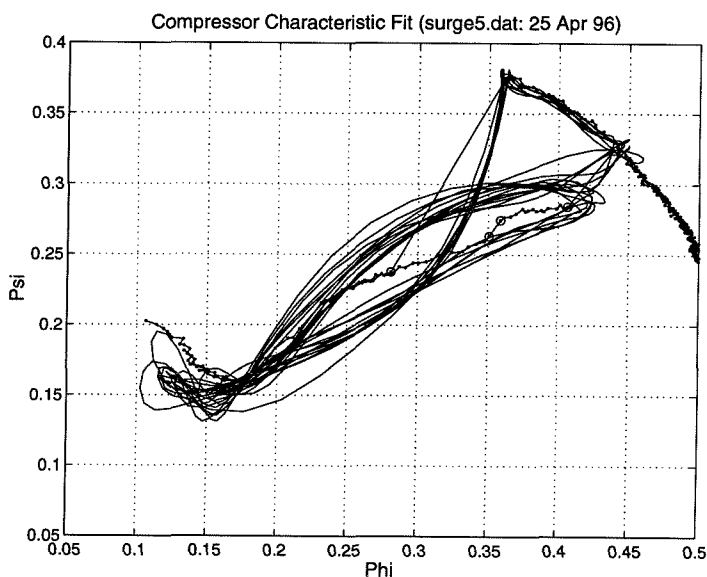
Figure 6.2 Solution of equation (6.2) for $\Psi_c(\Phi)$ based on experimental data. The multiple branches of this stalled compressor characteristic suggest that more than one mode of rotating stall is required to capture the behavior of the Caltech rig.

data (the experimental result corresponds to plotting the actual data for the group $l_c\dot{\Phi} + \Psi$). If the model above were accurate, then a plot of this group should show a basic "S" shape that is typical of the cubic polynomials normally used in modeling of the compressor characteristic. Figure 6.2 shows that this is not the case. There are three distinct branches of values for the compressor characteristic, and none of these leaves the branch of results obtained on the unstalled branch in a smooth way, therefore assuming the Moore-Greitzer model for surge and computing $\Psi_c(\Phi)$ based on experimental data does not give good results. The reason for this is that there is a significant amount of rotating stall present during portions of the surge cycle. This curve can therefore be used to decide what order of model (i.e. how many modes need the model should include) needs to be used to fully capture the rotating stall. While this technique doesn't give good results for the unstalled compressor characteristic in the unstable region, it does provide insight into the structure of the stalled characteristic.

If the rotating stall were dominated by the first mode, as the MG-3 model assumes, there would be only one solution branch for the stalled compressor characteristic, but the structure for the experimental data does not suggest this. Since the experimental data does not match the MG-3 model, more than a single mode of rotating stall must be present. This identification of the stalled compressor characteristic suggests that at least a second mode model for rotating stall is required to capture the dynamics of the Caltech rig. The next subsection extends the identification scheme to include the first two modes of rotating stall.

6.2.2 Including stall amplitudes

The coherent structure of the "dynamically corrected" compressor characteristic in Figure 6.2 suggests that the presence of rotating stall during portions of the surge cycle might be accounted for in a simple way. If the Moore-Greitzer equations are extended to include the first two modes of rotating stall, i.e.

$$\phi(\theta, t) = \Phi + \sqrt{J_1}\left(\sin\theta_1 + \cos\theta_1\right) + \frac{1}{2}\sqrt{J_2}\left(\sin\theta_2 + \cos\theta_2\right) \tag{6.8}$$

where $\phi(\theta, t)$ is the local flow coefficient in the annulus and J_1 and J_2 are the square amplitudes of the first and second modes of rotating stall which represent circumferential perturbations superimposed on the annulus averaged flow coefficient Φ, the result is:

$$\dot{\Psi} = \frac{1}{4l_c B^2}(\Phi - \gamma\sqrt{\Psi}) \tag{6.9}$$

$$\dot{\Phi} = \frac{1}{l_c}\left(\Psi_c(\Phi) - \Psi + \frac{1}{4}\frac{\partial^2\Psi_c(\Phi)}{\partial\Phi^2}(J_1 + J_2) + \right.$$
$$\left.\frac{1}{8}\frac{\partial^3\Psi_c(\Phi)}{\partial\Phi^3}J_1\sqrt{J_2}\cos\left(\theta_2 - 2\theta_1\right) + HOT\right). \tag{6.10}$$

With this set of augmented equations for a surge cycle, a new linear least squares problem can be developed for the compressor characteristic coefficients (the a_i for the polynomial assumption above) and the system parameters l_c, B, and γ. This identification scheme requires that Φ, Ψ, J_1, and J_2 can be measured directly.

On the Caltech rig the amplitudes of the first two modes of rotating stall for the Moore and Greitzer model cannot be measured directly. This is because flow measurements around the compressor annulus are not available. Static pressure measurements are however available, and these can be used to determine the magnitude of the rotating stall that is present. In order to perform the identification technique presented above for the Caltech rig, this relationship between the static pressure perturbations and the flow perturbations is required.

Based on equation (6.10), and assuming that the static pressure measurements at the wall capture the effects of the system transitioning into rotating stall, it seems reasonable to write the equation for $\dot{\Phi}$ as:

$$\dot{\Phi} = \frac{1}{l_c}\left(\Psi_c(\Phi) - \Psi + b_1 M_1 + b_2 M_1\Phi + b_3 M_1^2 + \cdots + d_1 M_1 M_2 + \cdots\right.$$
$$\left.c_1 M_2 + c_2 M_2\Phi + c_3 M_2^2 + \cdots\right), \tag{6.11}$$

where M_1 and M_2 correspond to the first and second Fourier modes of the upstream static pressure perturbation $\delta\psi$. The assumption that the pressure measurements completely capture the effects of rotating stall is based on the original assumption in the MG–3 model of potential flow in the inlet duct. Potential flow upstream,
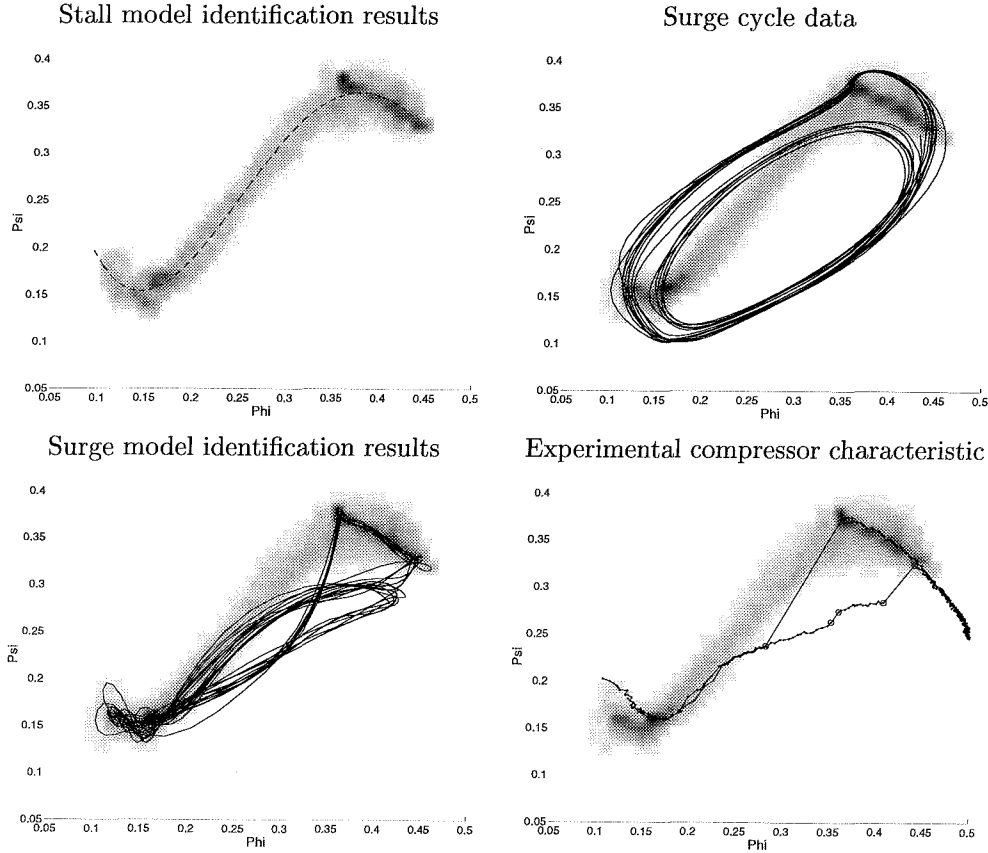
Stall model identification results

Surge cycle data

Surge model identification results

Experimental compressor characteristic

Figure 6.3 Solution of equation (6.11) for $\Psi_c(\Phi)$ based on experimental data. Shaded region corresponds to experimental data for $\Psi_c(\Phi)$, with darker regions corresponding to more experimental data.

combined with the unsteady Bernoulli equation, gives a closed relationship between the flow perturbations and the static pressure perturbations upstream of the rotor. The idea behind equation (6.11) is that the amplitudes of the flow coefficient perturbation amplitudes (J_1 and J_2) can be expanded in power series in terms of the static pressure perturbation amplitudes (M_1 and M_2). For the identification process presented here, it was determined experimentally that only the quadratic terms effected the identification process (i.e. including the cubic and higher order terms did not change how well the least squares fit approximated the measurements of $\dot{\Phi}$ and $\dot{\Psi}$). The development of the relation between the static pressure perturbations and the flow perturbations is explored further in Appendix D. Using equations (6.9), (6.11), and the experimental data shown in Figure 6.1, the problem can be cast as a least squares problem as was described in the previous subsection.

The results of this identification scheme are shown in Figure 6.3. The results of plotting the experimental data for the solution of equation (6.11) for $\Psi_c(\Phi)$ are
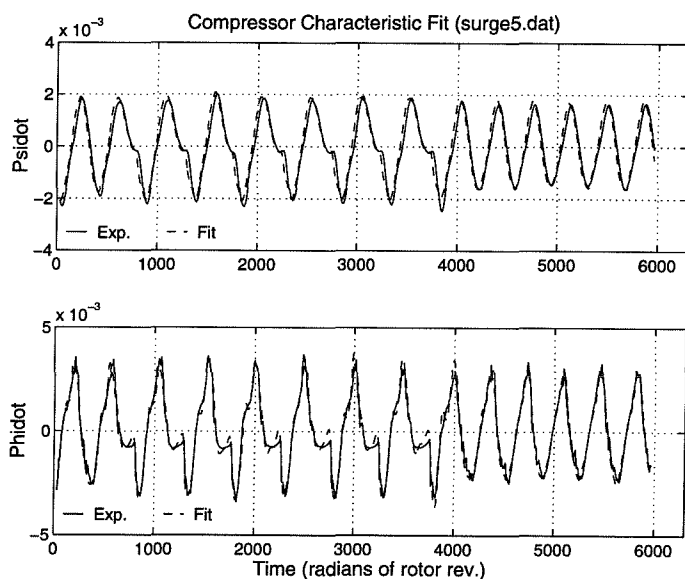
Figure 6.4 Experimental data compared with the least squares fit results obtained using the left hand side of equations (6.11) and (6.9).

γ	B	l_c	a_0	a_1	a_2	a_3	a_4	a_5
0.3033	0.71	33.0	0.354	-2.85	5.97	42.6	-151.2	127.2

Table 6.1 Caltech compressor surge configuration parameters.

shown as the shaded region, with the darker areas corresponding to higher density of experimental data points. The figure shows the identified region where the compressor characteristic lies compared with the polynomial curve for the compressor characteristic obtained during the identification, the surge cycle data, the stalled compressor characteristic obtained from the surge identification scheme presented in Section 6.2.1, and experimental measurements of the compressor performance.

Figure 6.4 shows a comparison between the experimental data time traces for $\dot{\Psi}$ and $\dot{\Phi}$ for the data shown in Figure 6.1 and the least squares fit which resulted in the coefficients in Table 6.1. The identification scheme was performed using data from 3000 to 4750 rotor radians (to capture both surge cycle amplitudes), and the comparison is presented for the entire data set. This time-series data matches extremely well match. In this identification scheme, a fifth order polynomial in Φ was used for $\Psi_c(\Phi)$.

Although the identification was performed using data over a series of surge cycles, it is possible to perform this method with data for only a single surge cycle. There would however be greater uncertainty in the parameter determination, particularly for a rig which had multiple surge oscillation frequencies (as the Caltech rig does).

6.3 Step Response on the Stable Side of $\Psi_c(\Phi)$

The identification scheme in Section 6.2 focused on identification based on surge transient data. On the Caltech rig, this requires that the rig be in a particular configuration; one with a large plenum installed in the downstream duct. In order to identify parameters for the rig in a configuration where surge does not occur (i.e. the configuration shown in Figure 4.1), a different technique must used. This configuration is of particular importance for studying controllers for rotating stall (for example, the configuration of the rig for the rotating stall controller presented be D'Andrea et al. [9] was in a configuration that did not surge).

The method presented here is based on the transients obtained during step response tests. If the throttle is stepped between two points on the stable side of the compressor characteristic curve, then a measurement of the transient response for the system can be used to calculate the parameters l_c and B. This is possible because $\Psi_c(\phi)$ is known on stable side of the peak. Transients of this form can be taken without exciting rotating stall, and the time-scale associated with the unsteady response of the compressor characteristic (unsteady loss dynamics) is much faster than the time-scale at which the surge dynamics respond. Therefore the unsteady loss dynamics can be ignored. These step response tests give measures for the values of l_c and B that will be used to simulate the rig in the rotating stall configuration, as opposed to the parameters obtained for l_c and B in Section 6.2 which will be used to simulate the rig in the surge configuration. The compressor characteristic information obtained using the surge cycle data is, however, applicable to both rig configurations.

The response of the compressor system states (Ψ and Φ) to step changes in throttle position were recorded. The step changes resulted in changes of Φ and Ψ as shown in Figure 6.5. Using Figure 6.6 as a lookup table for the value of γ as the bleed valve angle was varied, a least squares problem was formulated.

The resulting experimental data for step changes in the throttle position does not match the Moore-Greitzer surge model very well. One possible explanation for this is that the model assumes that compressibility effects are only important in the plenum. As the size of the plenum becomes small, the compressibility effects in other areas of the system (e.g. the upstream and downstream ducts, where the flow rate is not zero, but about 50% of the value in the of that in the annulus) become important. The experimental data also shows a substantial amount of noise in the measurement of Φ (see Figure 6.5). This is almost certainly part of the reason for the poor fit between the experimental data and the model. Different hotwire hardware was used to make the step response measurements presented in this section than was used to make the surge cycle measurements in Section 6.2 (which is why the surge measurements shown in Figure 6.1 have much cleaner signals for Φ). With clean data this identification method may hold more promise.

A second reason for the poor fit may be that the Moore Greitzer 2-D model does not capture the compressor dynamics for very small values of B. Because of these problems with this identification scheme, instead of using a least squares fit for the data, the value for $\frac{1}{4l_c B^2}$ was selected as the best match for the maximum or
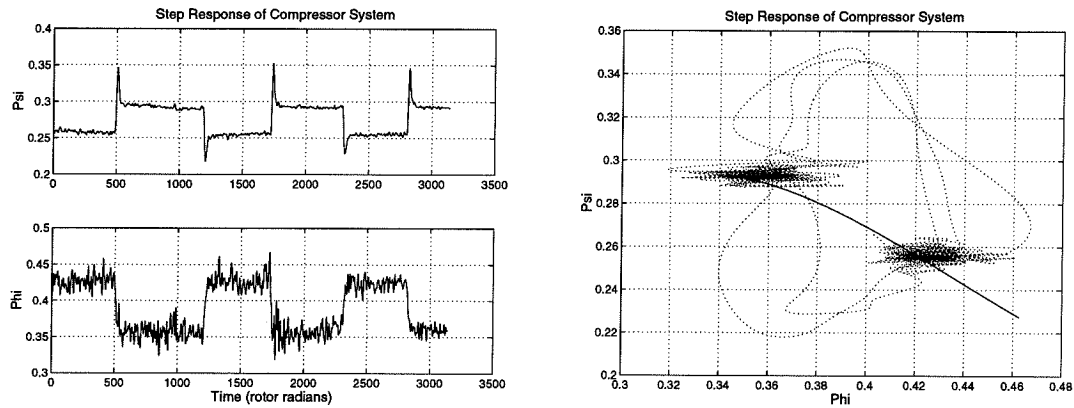
Figure 6.5 Step response of compression system. The plot at the left shows time traces of the experimental data, and plot at the left shows the transient data (dotted line) compared with the unstalled compressor characteristic.
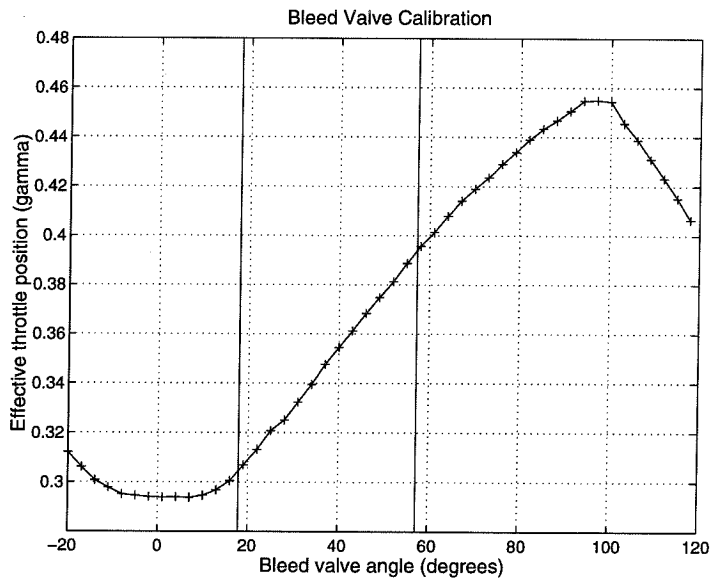

Figure 6.6 Effective throttle position γ versus bleed valve angle. The vertical lines show the two points that the valve was stepped between.
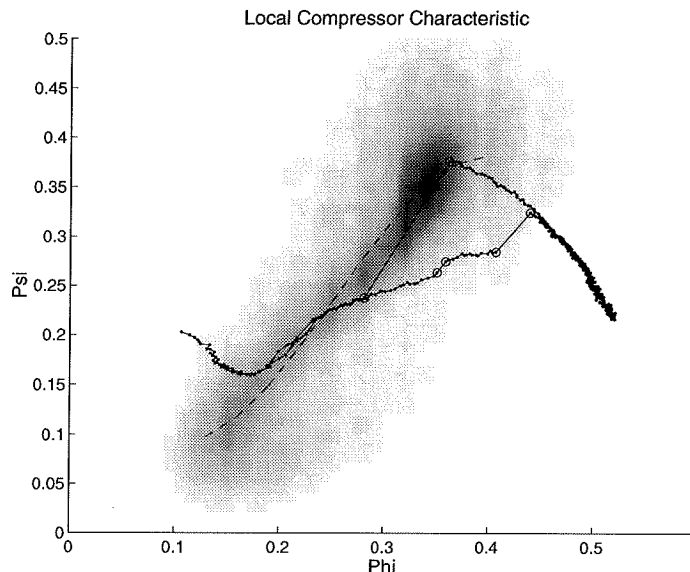
Figure 6.7 Experimental data for local measurement of $\Psi_c(\phi)$ across a compressor stage. The local measurements are shown as a density plot, with darker regions corresponding to more data for a given flow/pressure rise coefficient, and the dashed line is a polynomial fit to the data.

minimum values of $\dot{\Psi}$ that occurred during each step change in the throttle position. These extrema give bounds for the values of $l_c = 29.6$ and $B = 0.36$.

6.4 Local Measurement of $\Psi_c(\Phi)$

Just as the compressor characteristic can be backed out using transient data taken over surge cycles, the characteristic can also be backed out using transient data taken over rotating stall cycles. Instead of using annulus averaged values for the pressure rise and flow coefficients, local values are used. The distributed model for compression systems presented in [31] involves an assumption of a local compressor characteristic applying pointwise around the compressor annulus (the actuator disk assumption). In this section experimental measurements taken of the local pressure rise delivered by the Caltech compressor rig are presented. The measurements presented here were taken with the rig in the configuration shown in Figure 4.1 (rotating stall configuration).

The local flow rate through a rotor stage was measured locally using a hotwire probe placed in the compressor annulus within 0.15 rotor radii upstream of the rotor. The static pressure rise was measured locally across the rotor using a pressure transducer on either side of the rotor. The results were low pass filtered to help remove effects of the rotor motion (i.e. with a cutoff below the blade pass frequency).

Figure 6.7 shows experimental data for backing out the compressor characteristic

by measuring the local flow coefficient and pressure rise across the rotor. The cloud of data for the compressor characteristic obtained with these experiments is larger than that found in Section 6.2, but the results are comparable.

6.4.1 Determination of unsteady loss parameters

Dynamics for the transient response of the pressure rise delivered by the compressor were presented by Haynes et al. [23]. The dynamics presented there basically describe the time lag between changes in the flow rate through the compressor and the pressure rise delivered by the compressor, and therefore describes the transients of the pressure rise delivered by the compressor as the system moves between points on the steady compressor characteristic. These effects are important for getting simulations of rotating stall to match experimental data.

The size and shape of the "cloud" associated with the local measurement of the compressor characteristic gives information about the values of the time lag parameter in the unsteady loss dynamics equations. Since this parameter describes how quickly the pressure rise transitions from one steady state value to another as the flow rate is changed, if the lag parameter were large then a wide range of pressure rise values would be expected for a given flow rate. This would result in a large cloud of data from experimental measurement of the local compressor characteristic. The size of the cloud in Figure 6.7 shows that for the Caltech rig the unsteady loss time constant is relatively small. This is further explored in the simulation results presented in Section 6.5.

6.4.2 Comparison with surge cycle results

A comparison between of the compressor characteristics obtained using the surge cycle identification method and by measurements of the flow and pressure rise across the rotor are shown in Figure 6.8. The results show reasonable agreement for the shape of $\Psi_c(\Phi)$ between the two methods. It should be noted that the surge cycle identification provided data for $\Psi_c(\Phi)$ over a wider range of flow coefficients. The fits shown in the figure were not constrained to agree with known values of the compressor characteristic (values to the right of the peak when no rotating stall was present). For the simulations of the compression system presented in Chapter 7 the data from these two methods was combined with direct measurements of the compressor performance characteristic on stable side to determine a value for $\Psi_c(\Phi)$.

6.5 Comparisons with Simulation

The results presented in this section refer to simulations based on the distributed model of the (unactuated) Caltech rig presented in [8]. The details of that model are not presented here, but the theoretical basis for it is presented in [35], [31], and in [23].
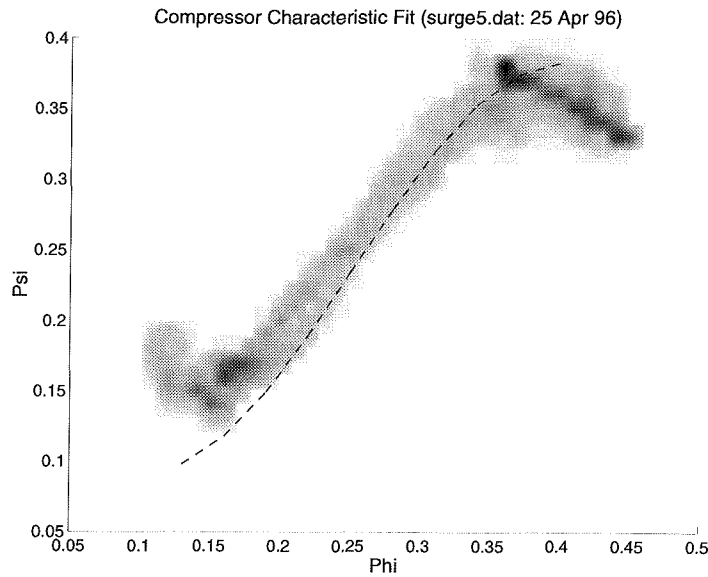
86

Figure 6.8 Comparison of compressor characteristics obtained from surge cycle identification method (density plot) and flow and pressure measurements across the rotor (dashed line).

6.5.1 Identification of a known model

In this section the identification procedures of Section 6.2 are applied to a simulation of a known compressor characteristic. The basic Moore-Greitzer model used in the surge identification scheme doesn't include the unsteady response of the compressor pressure rise to flow changes or higher order rotating stall modes. In order to fully capture the dynamics of stall cell growth, these effects are important. In this section the importance of these effects is considered by running simulations of a full distributed model for an axial flow compressor with unsteady loss effects included, and comparing the identified values for $\Psi_c(\Phi)$, B, and l_c, with those actually used as simulation inputs. This gives a measure for how much these parameters have been under/over estimated by assuming such a simple model of the system behavior during the identification process. In this section, simulation output for surge cycles is identified using the above identification techniques.

The compressor characteristic curve used as a simulation input was piecewise continuous, and the identification scheme performed here on simulation data is identical to that performed on the experimental data in Section 6.2. A polynomial in Φ is assumed for the compressor characteristic $\Psi_c(\Phi)$, and using the Moore-Greitzer model for surge a least squares problem is formulated for the coefficients of $\Psi_c(\Phi)$ and the rig parameters B, l_c, and γ.

Table 6.2 shows the parameters resulting from performing the surge identification based on the Moore-Greitzer model for surge on output data from the distributed model as the unsteady loss lag parameter, τ_L (see Section 3.1.1), is varied. The

τ_L	0.3	0.4	0.5	0.8	1.5
order = 11					
B	0.7709	0.7610	0.7524	0.7265	0.6738
l_c	6.4618	6.6323	6.7836	7.2761	8.4582
γ	0.2696	0.2696	0.2696	0.2696	0.2697
order = 9					
B	0.7709	0.7610	0.7524	0.7265	0.6738
l_c	6.4619	6.6324	6.7837	7.2762	8.4583
γ	0.2696	0.2696	0.2696	0.2696	0.2697
order = 7					
B	0.7707	0.7608	0.7522	0.7264	0.6737
l_c	6.4652	6.6355	6.7869	7.2792	8.4609
γ	0.2696	0.2696	0.2696	0.2696	0.2697
order = 5					
B	0.7691	0.7592	0.7507	0.7249	0.6725
l_c	6.4921	6.6630	6.8142	7.3082	8.4923
γ	0.2696	0.2696	0.2696	0.2696	0.2697
order = 3					
B	0.7564	0.7466	0.7387	0.7133	0.6622
l_c	6.7127	6.8893	7.0385	7.5471	8.7584
γ	0.2696	0.2696	0.2696	0.2696	0.2697

Table 6.2 Convergence of identification scheme on simulation data. Actual simulation values are: B=0.8, l_c=6.0, $\gamma = 0.27$.
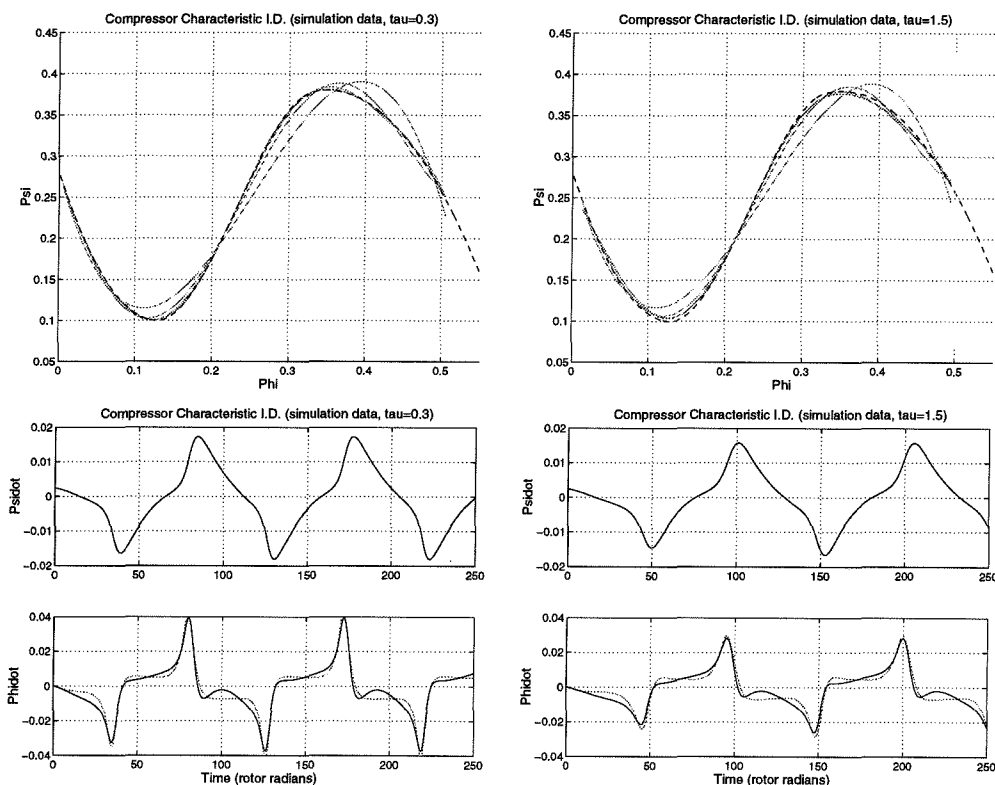
Figure 6.9 Surge identification results based on simulation outputs. The top plots show convergence to the simulated compressor characteristic as the order of the polynomial assumed for $\Psi_c(\Phi)$ is increased, and bottom plots show time traces for least squares fit compared with simulation output data.

table shows that as the order of the compressor characteristic assumed in the least squares problem is increased, the identified values of B, l_c, and γ get closer to the simulation input values. In addition, the top plots in Figure 6.9 show that the identified compressor characteristic approaches the compressor characteristic used as simulation input as the order of the polynomial assumed for $\Psi_c(\Phi)$ in the least squares fit was increased. The figure also shows that the identification scheme is robust to variations in the lag parameter associated with the unsteady loss dynamics, and the bottom two plots show how well the identified model fits the transient output data from the simulation data for a wide range of this parameter.

6.5.2 Unsteady loss parameters

The time evolution of $\Psi_c(\phi)$ (based on the model presented in [23]) can be simulated using the distributed model, and the results compared to the experiments to gain insight on the parameters associated with the unsteady loss dynamics. The time
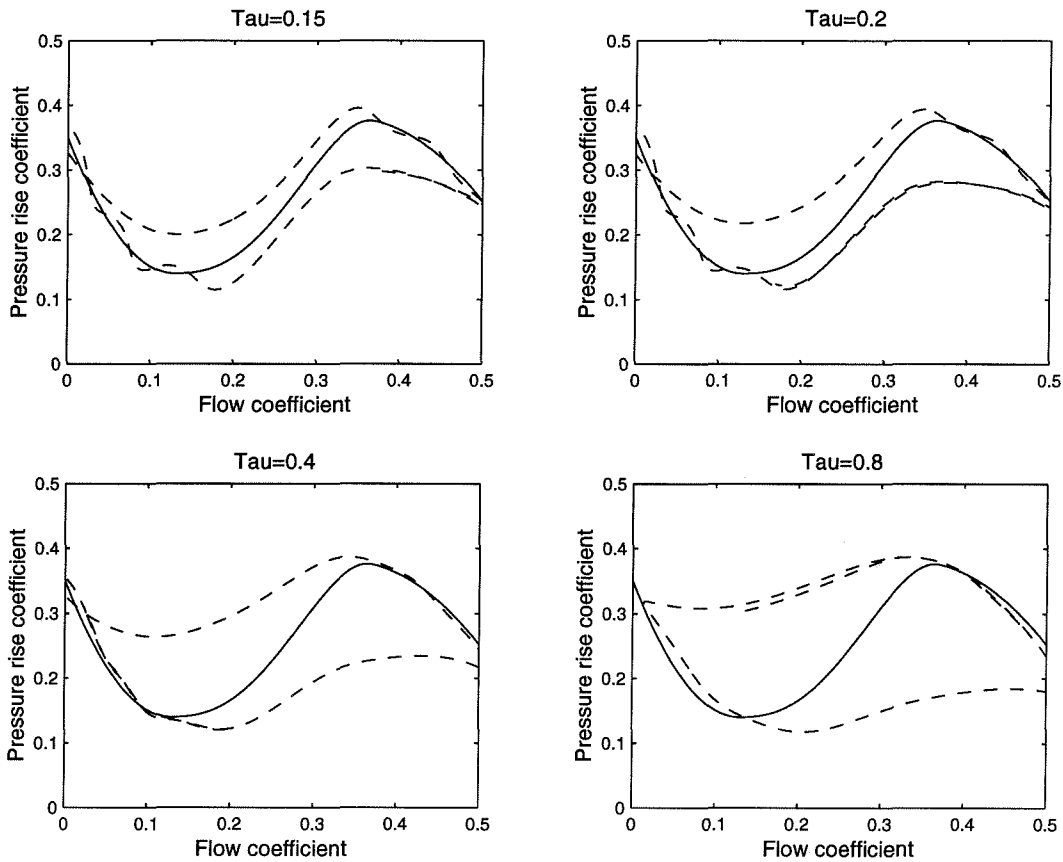
Figure 6.10 Simulated transient response of local compressor characteristic (dotted line) for various values of the unsteady loss dynamics time constant, τ_L. A surge like loop is present, the size of which is strongly dependent on the value of τ_L.

constant τ_L (see Section 3.1.1) has a drastic effect on the local compressor characteristic during rotating stall oscillations. Simulations of the sort just described are shown in Figure 6.10, where the comparison shows that the local compressor characteristic evolves in a surge like loop during a rotating stall cycle if unsteady loss lag parameter is high. Based on this simulation, the size of the cloud of data obtained in the experimental measurements of the local compressor characteristic, see Figure 6.7, shows that the value of τ_L on the Caltech rig is relatively small. Computation based on physical parameters suggests that the time constant on the Caltech rig is 0.5 (based on the fluid transport time through the rotor only), but a comparison between Figures 6.7 and 6.10 suggests that 0.15 is a more appropriate value.

Distributed Model: NAI
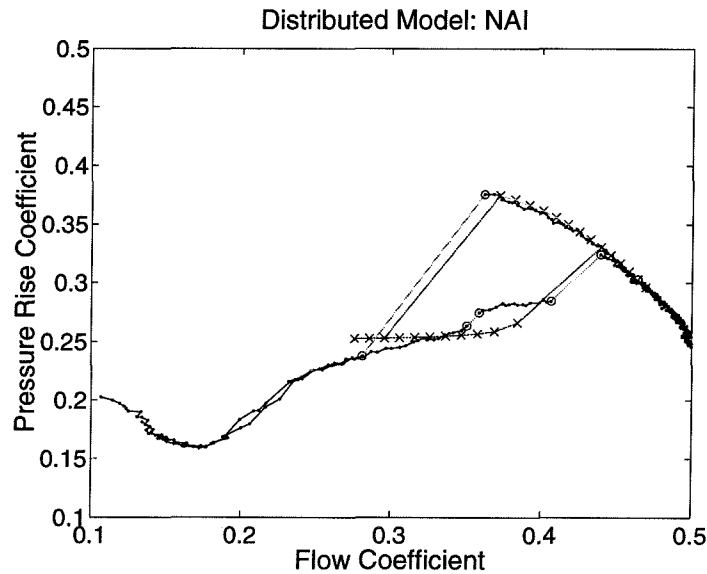
Figure 6.11 Simulated compressor characteristic using surge identification scheme including stall effects as presented in Section 6.2.2.

6.5.3 Open loop simulations of surge and stall

The main issue in simulations involving either the MG–3 model or the distributed model is determining which effects are the most important to match. In the lower order model, it is not possible to match all of the phenomena that are present in the experimental data. In this section we show how the distributed model simulation using parameters obtained with the above identification technique compares to experimental data for some phenomena.

Figure 6.11 shows the simulated hysteresis region due to rotating stall compared the experimental data. The distributed model with parameters based on the identification methods presented here agrees quite well with the experiments.

There are other comparisons to show between the experimental data and the simulation, these include (but are not limited to) the growth rate of stall cell, modal content of the stall, and the surge cycle amplitude. Further comparisons and investigation of the amount of noise required to match simulation and experimental data are presented in Chapter 7.

Chapter 7

Simulation Results

In this chapter, a simulation based on the distributed model described in Chapter 3 is correlated with experiments, the parameters used in the simulation were those identified in Chapter 6, including the results for the unstalled compressor characteristic curve.

The simulation of the open loop compression system is compared with experimental data for the compressor performance characteristic (as was shown previously in Chapter 6), the stall cell growth rate, and the amplitude of the surge cycle. In addition to comparisons between open loop simulation and experimental data, matching of a simulation of the air injection rotating stall controller with experimental results is explored.

First, the model for continuous air injection derived in Chapter 2 is investigated much the same way as the open loop model was investigated, with comparisons drawn between experimental data and simulation output. A similar procedure is then used to investigate the continuous air injection case and then the closed loop air injection case.

For the closed loop system, a search for the optimal phasing for the opening of the air injectors relative to the position of the stall cell is presented. This parametric study is quite similar to experimental search presented in Chapter 5. The results from simulation of the closed loop compressor characteristic are then shown to predict the elimination of the hysteresis region associated with rotating stall, as was previously found in experiments.

7.1 Open Loop Simulation

The previous chapter showed some correlations between experiments and the distributed model simulation, and here these issues are addressed in further detail. When it comes to modeling for complex systems for control it is important to use the lowest order model which captures the relevant system transients. For an axial flow compressor, there are many different details which could be selected as important to capture in a modeling effort. The three phenomena which have been selected as the most important for control purposes in this work are the size and shape of the hysteresis associated with rotating stall, the growth rate of the stall cell, and

B	0.1
l_c	29.6
μ	1.26
λ	1.26
η	-0.2
R	0.738
τ_L	0.15

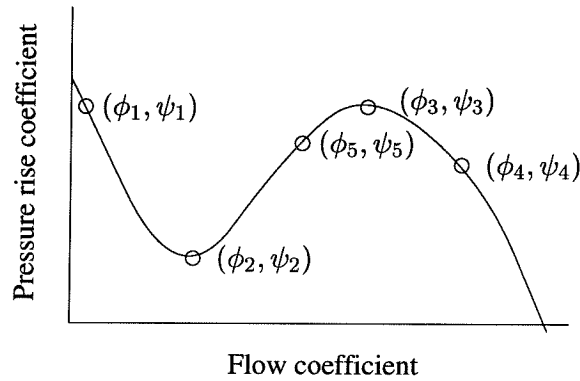**Table 7.1** Simulation parameters for the Caltech rig in the rotating stall configuration.

Figure 7.1 Piecewise continuous compressor characteristic used in distributed model simulations of the Caltech rig.

the amplitude of the surge cycle. The amount of noise in the system has an effect on each of the above areas and is also addressed.

The parameters used in the open loop simulation of the Caltech rig in the rotating stall configuration are given in Table 7.1. These parameters were previously described in Chapter 3, and further details about each of them can be found there. Figure 7.1 shows how the compressor characteristic was broken down into three polynomials. For flow coefficients below ϕ_2 and greater than ϕ_5 the characteristic is assumed quadratic and for flow coefficients between ϕ_2 and ϕ_5 a cubic polynomial was used. Note curve was required to have a continuous first derivative at ϕ_2 and ϕ_5, and the derivative at ϕ_2 and ϕ_3 were assumed to be zero.

7.1.1 Hysteresis regions

One of the most basic aspects of the compressor dynamics that the simulation must capture is the point at which the system transitions to rotating stall. Even the simple MG–3 model can capture this aspect of experimental results relatively easily, since

in that model the throttle setting where the linear stability of the rotating stall cell can be selected directly (and when no noise is present is given by the slope of the unstalled compressor characteristic, see Chapter 2, equation (2.22)).

The next step in capturing the hysteresis region is the transition out of rotating stall. The MG–3 model doesn't capture this aspect for the Caltech rig, but by including more than the first mode of rotating stall and more complicated expressions for the compressor characteristics (the MG–3 model typically models the compressor characteristic as a third order polynomial), this can be captured as well.

For the distributed model simulations of the Caltech rig, the first seven modes of rotating stall were modeled (seven modes were used in the open loop tests was so that same model could be also be used for the closed loop simulations) and the compressor characteristic was modeled as a piecewise continuous function, based on the identification data presented in Chapter 6. This piecewise continuous curve was constrainted to agree with experimental data taken of the compressor characteristic in the steady unstalled operating region.

Figure 6.11 showed a comparison of the hysteresis regions obtained in experimental tests compared with the results from the distributed model simulation, and that the throttle settings at which the simulation predicts that the system will transition to and from rotating stall matches quite well.

7.1.2 Stall cell growth rate matching

In order to develop a simulation to test controllers for rotating stall in a compression system, capturing the stall cell growth rates (the plural refers to the fact that the growth rate is a nonlinear function of the amplitude of the stall cell) is very important. This aspect of the dynamics is actually an extension of matching the size and shape of the hysteresis loop since matching the hysteresis loop involves getting the sign of the growth rate correct at two particular points.

The matching of the stall cell growth rate is one of the benefits of using a full nonlinear model for the rotating stall dynamics. If the model captures the growth rates correctly, then it gives a good estimate of how fast a controller must react in order to reject disturbances before they develop into full rotating stall. Figure 7.2 shows the growth rate of the amplitude of the first mode of rotating stall compared with experimental data from the Caltech rig. It is easy to see the nonlinear effects as the stall cell begins to grow. To the left of the peak, the slope of the compressor characteristic is positive, and it is this positive slope that dictates the linear stability of the first mode of rotating stall (see Section 2.2.3). As the flow is decreased from the stalling mass flow rate (as occurs during the transition to rotating stall), the slope typically increases. This causes the growth rate to increase as the stall cell initially begins to grow. The nonlinear effects clearly soon take over and the amplitude of the stall cell reaches equilibrium.

7.1.3 Amplitude of surge cycle

In the simulation, the coupling between the surge dynamics and the rotating stall dynamics is best addressed in conjunction with how noise affects the size (in the Φ
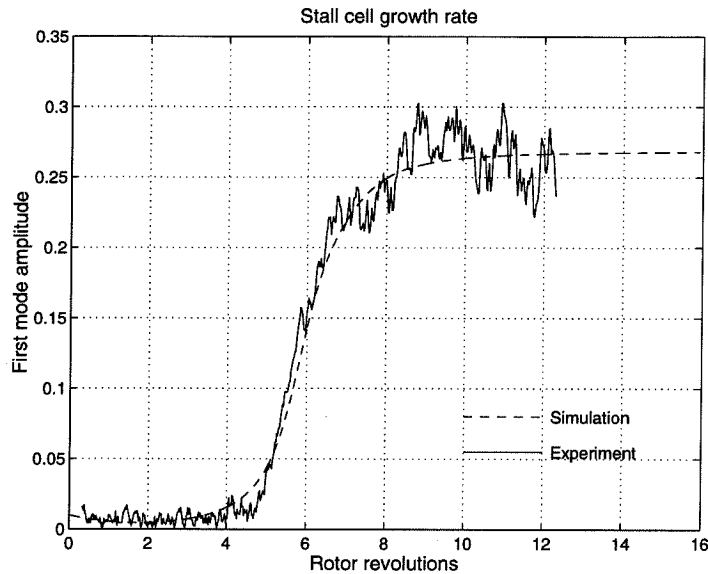
Figure 7.2 Comparison between simulation and experimental data for
first mode rotating stall growth rate.

versus Ψ plane) of the surge limit cycle. Since amplitude of the rotating stall cell
greatly affects the effective compressor characteristic (as was shown in during the
identification scheme presented in Section 6.2 for both the model and experimental
data), some method for exciting rotating stall during simulated surge oscillations
must be included. Figure 7.3 shows a comparison of the size of the surge limit cycle
for different amplitudes of noise exciting the rotating stall modes. Experimental data
is also presented. The figure shows that the phenomena of classic surge, and that the
amplitude of the rotating stall excitation effects the amplitude of the surge cycle very
strongly. Increasing the noise amplitude clearly brings the simulation results closer
to the experimental data. One reason for the discrepancy is that on the Caltech
rig the noise amplitude is dependent on the flow coefficient. This was determined
by measuring how much the static pressure transducers in the compressor annulus
deviated from their mean value at different flow rates. This could only be done on
the right side of the peak of the compressor characteristic where the rig was not
stalled. The results of these measurements showed that the noise amplitude varied
by at least a factor of three. The determination of the relationship between the flow
rate and the noise amplitude is still an open issue on the Caltech rig.

   In addition to the amplitude of the surge oscillation cycle the frequency of the
surge oscillation is affected by the amount of rotating stall present during the surge.
Figure 7.4 shows a comparison between the amount of noise present and the period
of the surge oscillation. Since the mount of noise present dictates how large the
rotating stall will grow over a single surge cycle, and the amount of rotating stall
affects the frequency of surge cycle, the noise becomes a parameter in the system for
matching experimental data. Table 7.2 shows the value of the surge frequency for
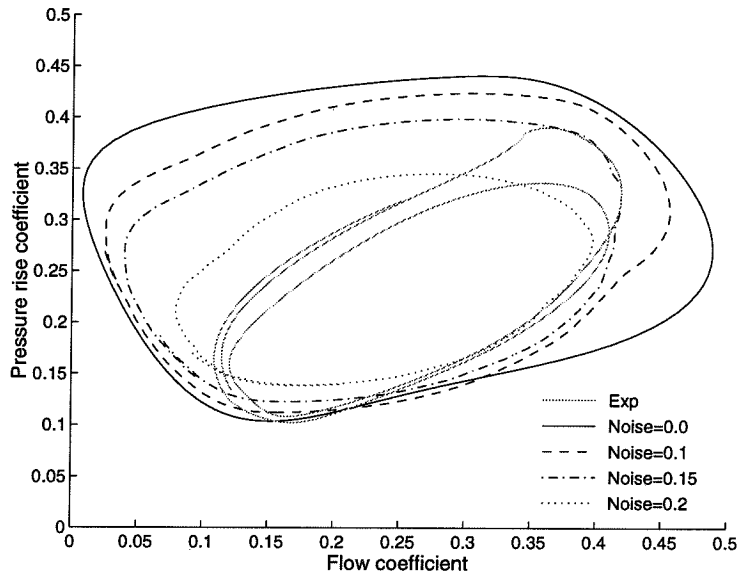
Figure 7.3 Comparison of surge cycle amplitudes for different amplitudes of noise. Experimental results for the surge cycle is shown as a gray line.
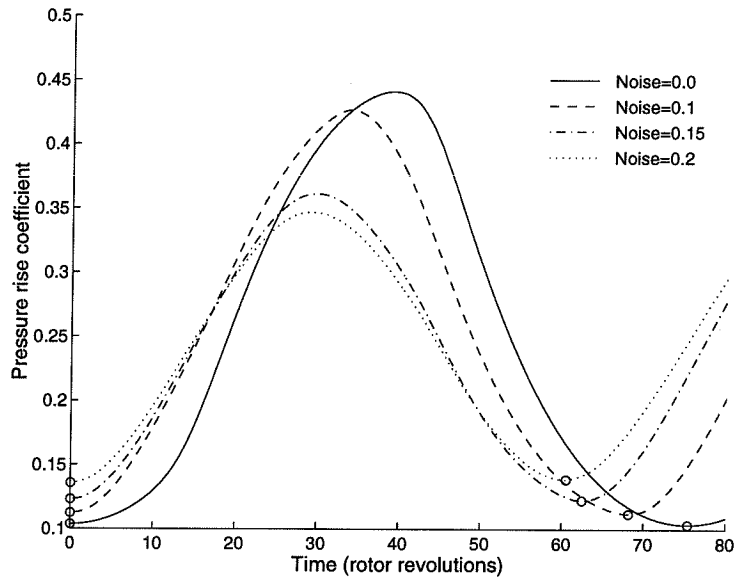
Figure 7.4 Surge frequency as noise amplitude is varied. The increased amount of rotating stall decreases the amplitude and period of the surge cycle oscillation.

Noise Amplitude	Surge Frequency (Hz)
0.0	1.33
0.1	1.47
0.15	1.60
0.2	1.65

Table 7.2 Surge frequency as noise amplitude is varied. Increased amount of rotating stall increases the surge cycle frequency.

each of the noise amplitudes presented in Figures 7.3 and 7.4. For comparison, the frequencies obtained for the two different surge cycles that occur on the Caltech rig (see Figure 6.1) were 1.4 and 1.8 Hz. Again, in order to match the experiment more closely the noise amplitude would need to be made a function of the flow coefficient.

7.1.4 Noise issues

The identification scheme presented in Section 6.2 results in parameters and a compressor characteristic. A distributed model simulation of the compressor system with these results does not produce output that is comparable to the experimental measurements of the system states without a good model of the noise level in the experiment. This is particularly true for simulations of the surge dynamics since the amplitude and frequency of the oscillation is directly affected by the amount of rotating stall present. In the simulation, noise is continuously required to perturb the system away from the invariant zero amplitude stall cell solution (see equation (2.22)). This issue was touch on in the proceeding subsections, and is further addressed here.

Simulations were performed with different amplitudes of noise to determine how the simulation predicted the amplitude (and location) of the surge cycle would be affected. The noise was introduced into the local flow coefficient variables, i.e.

$$\phi(\theta, t) = \phi_{endstep}(\theta, t) + n(\theta, t), \tag{7.1}$$

where $\phi_{endstep}(\theta, t)$ refers to the fact that the noise was added to the flow variables at the end of each time step, before the next integration step. The motivation for introducing noise in this was to allow a single noise model to affect the system dynamics of the compressor system and the sensor dynamics of the control system. Another noise model which is more popular for simulating compression systems is given by

$$\Psi_c(\phi, t) = \Psi_{c_{endstep}}(\phi, t) + n(\theta, t) \tag{7.2}$$

where the noise is introduced as a perturbation on the pressure rise delivered by the compressor. This model contains the fact that the determination of the compressor

performance characteristic is uncertain. The two models are roughly equivalent since

$$\Psi_c(\phi, t) = \Psi_{c_{endstep}}(\phi(\theta, t) + n(\theta, t)). \tag{7.3}$$

The motivation for using this model for adding noise into the system is that it allows a single model for noise to be used to introduce noise into both the stall call computation and into the system dynamics. The simulation produced similar results for either noise model.

7.2 Continuous Air Injection Simulations

In order to perform simulations of the continuous air injection on the Caltech rig, the shifted compressor characteristic must be identified, as well as the amplitude of the mass and momentum that the air injectors add to the flow. The simulations presented here for the actuated compression system includes the dynamics of the actuators were included as described in Section 3.2 and both the compressor characteristic shift and the mass/momentum addition effects are included in this simulation.

Again, it should be noted that it is clear from the analytical results of Section 2.3.1 that a shift of the compressor characteristic is not enough to eliminate the hysteresis region for the case where continuous air injection case and the unactuated case have overlapping hysteresis regions. The experimental results of Section 5.1 that this is the case. The experiments of Section 5.2 show however that more than just the compressor characteristic shifting effects are important for eliminating the hysteresis region. Further details on the simulation of open loop continuous air injection are presented later.

7.3 Closed Loop Air Injection Simulations

The closed loop air injection simulations are based on the 2–D air injection control law presented in Section 5.2. The dynamics of the actuators were included as described in Section 3.2. In order to improve the stability of the simulation, the unsteady loss dynamics time constant was increased from $\tau_L = 0.15$ (used in the unactuated simulations, see Table 7.1) to $\tau_L = 0.35$. Without this increase, the highest mode in the simulation tended to go unstable (which would indicate that more modes need to be simulated). These instabilities seem to be caused by the discrete nature of the air injection, and would be eliminated by air injection that acted in a smoother way. This increase in this time constant does not drastically affect the size of the rotating stall hysteresis or the growth rate of the rotating stall. Note that both the compressor characteristic shift and the mass/momentum addition effects are included in the simulation.

Distributed Model: Compressor Characteristics
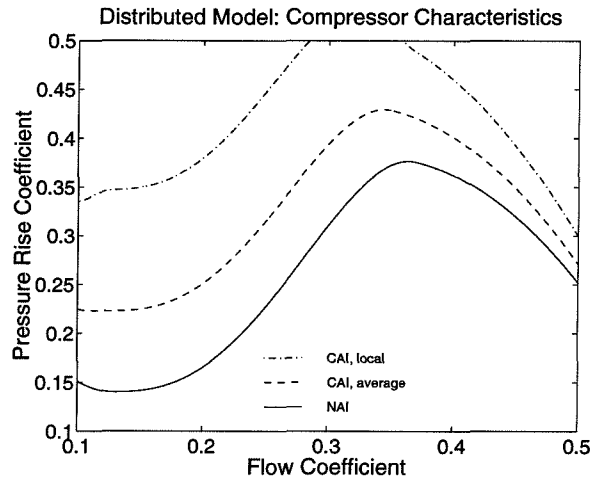
Figure 7.5 Shifted compressor characteristics.

7.3.1 Parametric study on simulations

The geometric parameters associated with the distributed model were first calculated from physical measurements of the Caltech rig, and initial guesses were taken for those that remained. The simulation parameters were then adjusted (specifically the compressor characteristics) to match the rotation and growth rate of the transition to rotating stall and to match the pressure rise delivered during fully developed rotating stall. Compressor characteristics were determined for both the no air injection (NAI) and continuous air injection (CAI) cases, as per the experimental data shown in Figure 5.3.

Since the simulation parametric study will compare how controllers respond to a disturbance from the peak of the unstalled compressor characteristic (as was done for the experimental setup), the compressor characteristics for the two cases were selected so that stall occurred at the same point as determined experimentally (there is a slight discrepancy to account for the noise in the experimental setup). In addition, the characteristics were adjusted so that the open loop simulations corresponded to the behavior observed experimentally at the transition to stall and at recovery from rotating stall. For this reason, the simulated open loop characteristics do not match up perfectly with those observed experimentally over the entire hysteresis region. In order to correct these errors, the details of fully developed rotating stall would have to be modeled over the entire range of the throttle settings, and a substantially more complicated model would be required.

The next step was to simulate the open loop air injection case with a non-uniform compressor characteristic. From the characteristics shown in Figure 7.5, the equivalent local compressor characteristic for the stations where air injectors are located, Ψ_{csh}, can be determined. This was done by requiring that the average characteristic obtained when using the characteristic shown as a solid line in Figure 7.5 have the same value as that obtained when using the locally shifted characteristic at three

Distributed Model: CAI
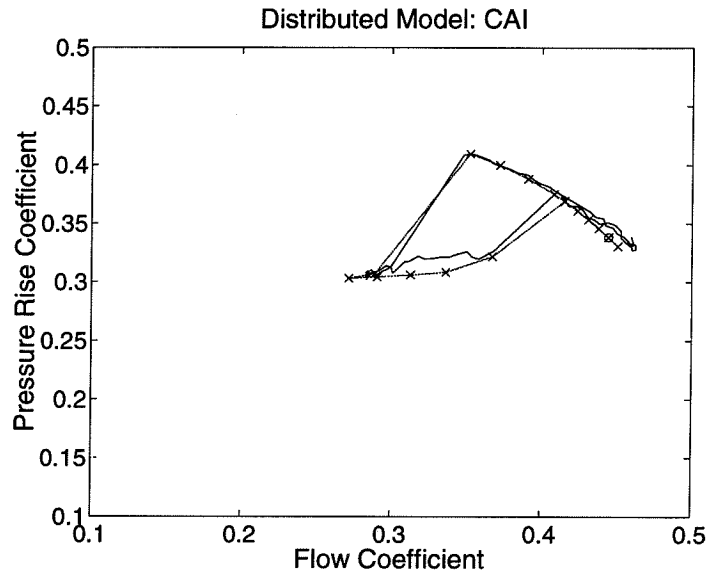
Figure 7.6 Hysteresis loop for simulation continuous air injection compressor characteristic. Simulation data points are denoted with an x.

stations (dash-dot line in figure), and the average nominal compressor characteristic (shown as a dashed line in the figure) at the remaining stations.

Figure 7.6 shows the compressor characteristics used in simulation for the continuous air injection case, as well as the experimental results for the same situation for comparison purposes. The figure shows that the simulated and experimental hysteresis regions match quite well.

7.3.2 Parametric study

The goal of the simulation based parametric study was to determine the optimal control strategy based on a model for the compressor. In particular, a search for the optimal phasing for the activation of each air injector relative to the measured position of the peak of the first mode stall disturbance was performed.

The control algorithm was essentially the same as the one described in Figure 5.4 in Section 5.2. The major difference was in the implementation of what corresponded to activating the air injectors for jeton number of servo-loops in the experimental study. This was accomplished by activating each air injector when the magnitude of the first mode disturbance became greater than some threshold magnitude and the phase of the first mode disturbance was within a pre-specified window. The threshold magnitude was based on the noise level in the experimental determination of the magnitude of the first mode.

In terms of the logic of Figure 5.4, this corresponds to setting jeton to 0 and window to 120 degrees, and running the servo-loop at an infinitely high rate. This
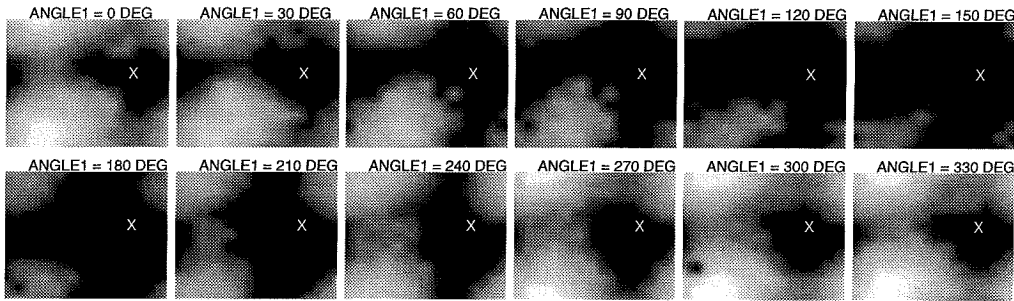
Figure 7.7 Simulation parametric study: dark regions correspond to
good controller performance.

is roughly how the control algorithm behaved in the experimental studies. This
algorithm was used to simplify the simulation code and vastly decrease its running
time.

As in the experimental study, the phasing of each air injector was independently
varied in 30 degree increments. For each controller tested, the average amplitude
of the first mode stall cell was recorded. Analogously to the experimental results
of Figure 5.5, the simulation results are shown in Figure 7.7. The simulation study
predicts the same periodic trends for the optimal phasing as are seen in the experi-
mental data.

In all the simulations, the same initial stall cell disturbance (both in magnitude
and phase) was used. It should be noted that this and the nonlinear growth rate of
the stall cell cause any symmetries in the plots of Figure 7.7 to break down, i.e. we
would not expect the plots to be shifted versions of one another because while the
geometry of the system is symmetric, the initial conditions are not.

7.3.3 Closed loop compressor characteristic simulations

The closed loop characteristic for the optimal controller obtained via simulation
is shown in Figure 7.8. The hysteresis region has essentially been eliminated, as
was determined experimentally. The transition to rotating stall is also gradual,
i.e. there is no jump from zero stall to fully developed stall. These two results,
along with the matching of the trends between the experimental and simulation
parametric studies strongly support the air injection model presented here. Further
work on refining the model will focus on using numerical techniques to determine
the bifurcation characteristics, and coupling surge controllers with the pulsed air
injection controller for rotating stall.

It should be noted that the mass/momentum addition terms are quite impor-
tant for obtaining the elimination of the rotating stall hysteresis. Figure 7.9 shows
the closed loop compressor characteristic that results if the mass and momentum
addition terms are left out of the simulation. The hysteresis region is clearly not
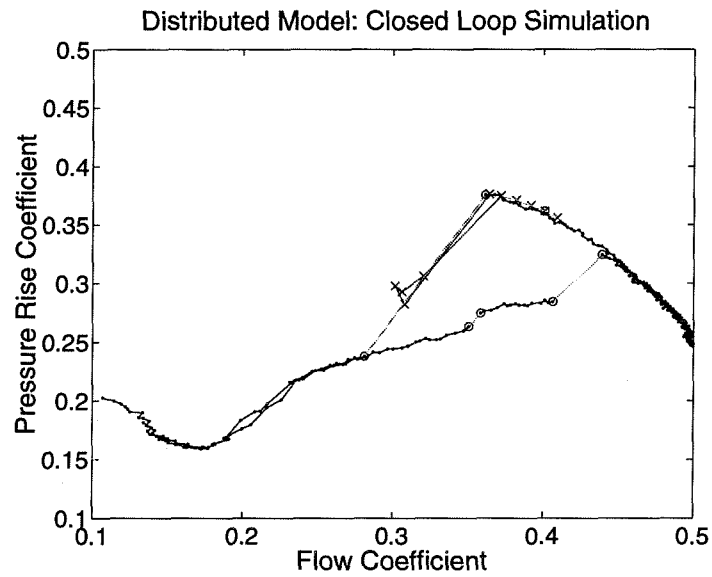
Figure 7.8 Simulated closed loop compressor characteristic. Simulation data points are denoted with an x.
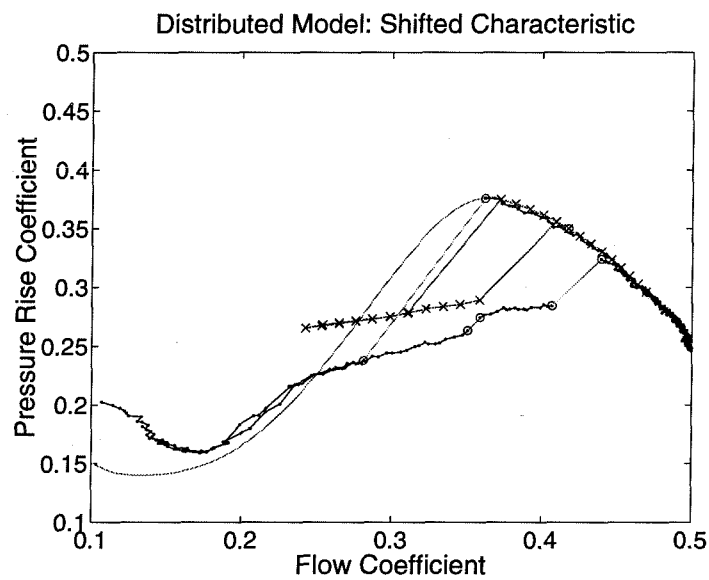
Figure 7.9 Simulated closed loop compressor characteristic without mass/momentum addition terms. Simulation data points are denoted with an x.

eliminated. This suggests that an analysis on a low order (MG–3 level) model which includes these terms may be insightful.

7.4 System Level Considerations

There are several issues to be addressed when adding a closed loop controller for rotating stall or surge to an engine. Answering all of the questions which arise is beyond the scope of this thesis, but the more important of these issues are outlined below. The topics addressed include the use of recirculation for air injection control, the wasteful nature of bleed valve controllers (they dump pressurized air to atmosphere), and the effects of rotating stall and surge controllers on the downstream components such as the combustor and turbine.

7.4.1 Recirculation for air injection controllers

Before a real engine will be outfitted with an air injection actuator for control of rotating stall, it must be determined where the injected air will come from. One option for developing the injection air is using a small compressor driven off of the main engine.

In order to determine the feasibility of this actuation method, analysis based on the steady state operation of the 2–D air injection controller running on the Caltech rig was performed. In this comparison, the amount of control effort expended to accomplish the control is subtracted from the amount of useful work delivered by the compressor.

Figure 7.10 shows the closed loop compressor characteristic for a controller which uses pressurized air from downstream of the compressor to generate the air to be used by the injectors. The plots in the figure were generated by assuming that the energy required by the air injection control law would be drawn from the flow directly downstream of the compressor. A family of curves obtained by assuming different efficiencies (7, 10, 17, and 50%) for the device which supplies the injectors is presented. The horizontal axis shows the effective flow rate through the combined compressor/actuator system (i.e. air drawn off to power the air injectors is not available for use in the combustor/turbine). Figure 7.10 implies that if the compressor is operated for extended periods to the left of the peak, a significant amount of flow (which would normally be used for producing thrust) would be used by the actuator. For short duration operation to the left of the peak, a plenum could be used to store enough air to drive the injectors, and there would be no drop in the effective flow through the compressor. These considerations suggest that the air injection controllers presented here are best suited for disturbance rejection, not for stabilizing the system while it is operated on the left side of the compressor characteristic peak.

The flatness of the peak of the compressor characteristic shown in Figure 7.10 is somewhat misleading. This flat range is not useful as an operating region; it represents the transition from no control action to full control action, which occurs nearly immediately for throttle settings to the left of the peak of the characteristic.
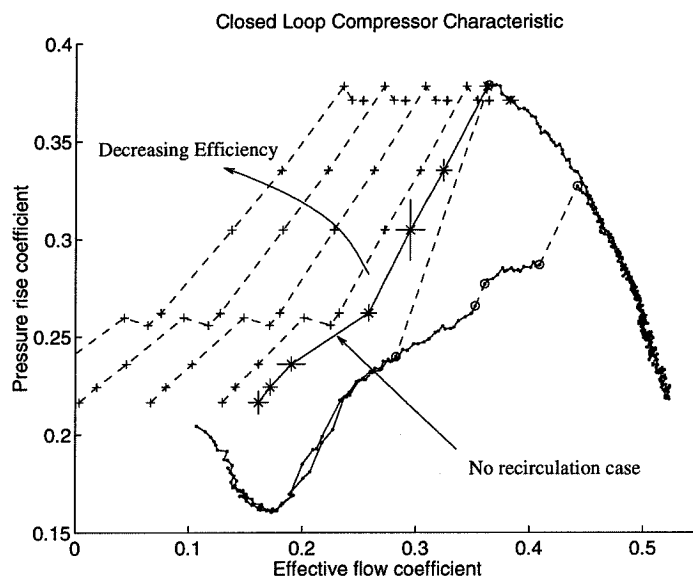
Figure 7.10 Effective compressor characteristic for experimental air injection controller data. Dashed curves correspond to air injection recirculation of different efficiencies.

7.4.2 Bleed valve controllers

Before a rotating stall control system will be installed on a jet engine, the mass/momentum/energy used to drive the actuator will have to be compared to the amount of energy delivered by the compressor when the actuator is operating. All forms of actuation will therefore penalize rig operation in some way. With a bleed valve type actuator, the control is accomplished by allowing some of the pressurized flow on the back side of the compressor to leak out to the atmosphere. This is true for rotating stall controllers and for surge controllers. Clearly, in this situation the compressor does useless work by compressing air that will not be used. If the amount of compressed air is substantial, this sort of control law must also be used only for disturbance rejection.

It is difficult to compare the different sorts of actuators for controlling rotating stall. Computing the amount of energy in the air which must be bled for the bleed valve controller to function and the amount of energy required for an air injection actuator to accomplish the same task is one method which could be used to determine the best controller for a given task.

7.4.3 Effects of controllers on downstream components

Before any of the air injection rotating stall controllers can be implemented on a real engine, a detailed analysis which includes the thermodynamic effects of bleeding air from downstream (or injecting air upstream) of the compressor will be required. This is also true for the bleed valve control strategies currently under development

(see Section 1.2.2 for an overview). This sort of analysis would focus on determining the temperature changes which occur at the turbine inlet (one of the likely places for overheating) when the controller is active.

In Chapter 1 the stability stack reduction in the size of the stability stack was described as one of the motivations for using active controllers on engines. In order for the ideas presented there to be fully applicable, the thermodynamic efficiency obtained when operating above the nominal steady-state operating line must be must be computed. If operating in the new region (with a controller) is substantially less efficient than in the original operating region (without a controller) the control system may not be useful.

In addition to the steady thermodynamic analysis described above, a full analysis of the transient effects that active control may introduce is also required. The transient effects caused by the controller which must be considered include any plenum pressure fluctuations which occur downstream of the compressor, thermal transients, and blade loading. The pressure fluctuations are particularly important because they may cause problems for the combustion process (the main purpose of the engine is the combustion). The other effects must be addressed because they may effect the lifespan of the engine. The controller may eliminate rotating stall and surge, but may stress the engine components in ways nearly as damaging.

The sort of steady state thermodynamic modeling and transient analysis described above is not an issue on the Caltech rig, but would certainly be important on any real engine. The level of modeling requires detailed information about engine performance; information which is usually not available outside of engine manufacturing companies.

Chapter 8

Conclusions

This chapter contains a summary of the work presented in this thesis as well as some ideas for future work in the control of axial flow compressors. The summary doesn't contain the exact details of each piece of analysis, simulation, or experiment; these results are contained in the individual chapters.

8.1 Summary

Part of the focus of this thesis was to develop a model which explained the air injection control strategy that was developed through experiment on the Caltech rig [7]. The starting point of this modeling work was the Moore and Greitzer model for axial flow compressors [35]. As a first cut, the MG–3 model was extended to include the effects of air injection (as a shift in the compressor performance characteristic) and bifurcation analysis was performed to determine how the closed loop system dynamics are different from those of the open loop system. This low order model was then shown to capture qualitatively some of the effects seen in experiments and used to select parameters for the placement of the air injection actuators. The optimal choice for how the air injection should shift the steady state performance characteristic for control purposes was determined based on this low order model.

An experimental parametric study of the geometric parameters of air injection was performed, and the optimal choice of parameters for control purposes (based on the previous low order model analysis) was determined. Experiments which better characterize the results that the models capture were presented. It was shown that the hysteresis region in the compressor performance characteristic can be eliminated if air is injected using 1–D and 2–D schemes. For the 2–D air injection scheme, this was shown to be true even when the shifted steady state performance characteristic had a hysteresis region which overlapped that of the unshifted characteristic. The rotating stall controller was also shown to be beneficial in damping out surge oscillations. A throttle based surge controller was implemented and shown to create new stalled equilibria in the process of eliminating surge. The combination of this surge controller and the air injection rotating stall controller was shown to provide better performance than the rotating stall or surge controllers alone.

In order to develop simulations which matched experimental data from the Caltech rig, investigation of systematic methods for determining the simulation parameters were developed. In the past, identification has been based on running large number of simulations and adjusting the parameters to the output with experimental measurements. Now based on direct experimental measurements of system transients the open loop simulation parameters can be determined. In addition to the determination of the basic rig parameters, the methods that were developed which succeeded at backing out the shape of the compressor performance characteristic in regions where direct measurements were not possible. These methods also provided information on the size of the unsteady terms in the pressure delivery by the compressor.

A higher order model, based on the previously described distributed model of Mansoux et al. [31], was used to develop a qualitative match between experiments and a simulation. The results of this modeling effort compared quite well with the experimental results for the open loop behavior of the Caltech rig. The details of how the air injection actuators affect the compressor flow and the pulsed air injection control algorithm was implemented in the simulation. The simulation then predicted the same optimal controller that was obtained through experiments. The simulation also reproduced the elimination of the hysteresis region for the closed loop compressor performance characteristic.

8.2 Areas for Future Study

There are several areas which still need investigation in the control of rotating stall and surge, both experimentally and analytically. There are still many interesting issues to explore in the area of closed loop control of rotating stall and surge on axial flow compressors.

One of these areas is how distortion affects the controllers presented here. One of the largest components in the stability stack presented in Section 1.1 is distortion, and if distortion is treated as a disturbance to be rejected, closed loop control can drastically reduce the amount of margin required to avoid instability.

The downstream effects of the control strategies presented here need to be investigated. It is not clear that the controllers presented will not cause difficulties when they are implemented on actual engines. There can be substantial coupling between the instabilities in the downstream combustor and the pressure transients in the compressor. The Moore and Greitzer model for axial flow compression systems doesn't concern itself with the circumferential perturbations that occur on the downstream of the compressor. The perturbations may have drastic effects on the performance on a downstream combustor. Further modeling efforts are therefore required in order to predict how the overall engine responds to active control of rotating stall in the compressor.

The tradeoff between the number of air injectors and the control authority of each injector has not yet been explored. The results from the closed loop air injection rotating stall controller suggest that three independent injectors are better than a single injector (since hysteresis loop was eliminated in one case but not the other),

but even though the Caltech rig has a substantial amount of second mode rotating stall. On an actual engine, unmodeled effects such as blade loading may have a strong influence in this area.

The Caltech rig is a single stage compressor, and it is not clear how well the controllers proposed here would perform on multiple stages. One possibility is to introduce some form of control between each stage, but this of course introduces much more complexity to the control system (in particular the amount of actuator hardware required).

There is clearly more work to be performed in the area of recirculation as a means of obtaining the injection air. The studies presented here show that (if energy is a reasonable measure) air injection could be accomplished with recirculation. While this is true on the Caltech rig, the results on a full size engine might not be so favorable. Before any closed loop control system for rotating stall and surge is implemented in a real engine (inlet guide vanes, bleed valves, air injection, etc.) a detailed thermodynamic analysis will be required to determine, for example, the effects on the turbine inlet temperature.

There is still work to be done on developing models which predict the closed loop behavior of a compression system. The identification schemes presented here give good results for developing open loop models, but they do not address the actuated cases. The air injection simulation presented in Chapter 7 was developed partially from first principles, but also had parameters which had to be tuned by matching simulation output with experimental results. This is unlike the open loop simulations which matched the experimental data quite well without iteration.

It is possible to perform numerical bifurcation analysis on the high order model developed to simulate the air injection controller. Using packages such as DsTool and AUTO94, a full simulation study of the nonlinear dynamics of the closed loop simulation could be performed. This analysis might provide insight into the further refinement of the controller. The high order models for axial compressors are an example of systems where most nonlinear control design techniques break down, and the use of numerical dynamical systems analysis packages provide the design tools needed to analyze controller designs.

There was no direct design method used for controller development on the Caltech rig. Most work was done by understanding the basics of how the system behaves and then trying to modify that behavior, for the most part through trial and error. While the MG–3 model provided useful for the controller analysis, it was not a design methodology. The development of systematic methods of controller design is therefore an area which needs further work.

Appendix A

Experimental Setup Details

Extensive details on the orignal construction of the Caltech rig were presented by Khalak in [26]. This rig has been modified during use in extensive experimentation, and more detail on its construction can be found in [27], [9], and [8]. Some further details are presented here, including manufacturers and specifications.

A.1 Compressor Experimental Details

Additional details on the construction of the rig are presented here for completeness. If you want to build your own compression system, then you might want to read this section, otherwise you should probably ignore it.

A.1.1 Compressor

The compressor is an Able Corporation model number 29680 axial fan. Table A.1 describes the exact shape of the rotor. The compressor is driven by a three phase electric motor attatched to a variable frequency power supply. By varying the frequency of the motor input voltage, the speed of the compressor can be changed. The compressor rotor rotates at one half of the input voltage frequency, i. e. 200 Hz supply voltage frequency corresponds to a rotation rate of 100 Hz.

Radius (m)	β set	t/c	f/c
0.060	51.6	.11	0.094
0.066	45.6	.11	0.080
0.072	40.2	.11	0.071
0.079	36.1	.11	0.066
0.085	32.6	.11	0.062

Table A.1 The blade shape parameters are defined as: β set is the angle between the chord and the plane of the rotor disk, t/c is the maximum thickness divided by the chord, and f/c is the camber ratio.

A.1.2 Plenum and duct work

The plenum on the Caltech rig is a 4'x4'x4' box made of 3/4" plywood. Most of the ductwork is made of 7" I.D. fiberglass tube, with many of the interchangeable subsystems (such as the sensing ring described in Chapter 4) being made of 7" I.D. acrylic tubing. The hole pattern on each component is uniform and allows the components to be bolted together in nearly any order.

A.2 Sensing

The Caltech rig is instrumented pressure transducers and with hotwire anemometers. The pressure transducers were used for tracking the stall cell during open loop measurements of the stall cell growth rate and for the closed loop control of rotating stall as described in Chapter 5. The hotwires were used for investigating the local flow rate in the compressor annulus during the transition to rotating stall and for sensing the unsteady axial flow rate (during surge cycles for example).

A.2.1 Pressure transducers

The pressure transducers used on the rig are all made by Honeywell Micro Switch. These transducers are availible in several different pressure ranges. On the inlet side of the Caltech rig, the transducers all have a range of $\pm$ 2.5" H_2O, and on the outlet side the transducers have a range of $\pm$ 5.0" H_2O. The bandwidth of these sensors is approximately 1 kHz. With a supply voltage of 8 volts, the output of these sensors range from 1 to 6 volts, with zero pressure corresponding to approximately 3.5 volts.

A.2.2 Hotwire

The hot-wire anemometers used on the rig are made by DANTEC, and are model number P11. These are platinum plated tungsten wires, and can measure velocities up to 200m/s in air. The hot-wire signal is conditioned by a MATILDA Meter constant temperature bridge. This bridge is custom equipment available for loan from the Caltech equipment pool and may not be widely availible.

A.3 Actuation

There are three main actuators on the Caltech Rig which were used for the work presented here. The are the air injectors, bleed valve, and the downstream throttle. Only the first two of these are useful for active control, the third is used to set the operating point of the rig.

A.3.1 Air injectors

The air injectors consisted of high speed solinoid valves designed for use in metering natural gas into piston engines. They are manufactured by Servo Jet Inc. and are supplied by Clean Air Partners. Since the air injectors are a major focus of the

work presented here, extensive detail on them is presented in the Appendix C. The bandwidth of the valves is approximately 200 Hz, and the flow rate through them is a function of the supply pressure.

A.3.2 Bleed valve

The bleed valve is a custom built butterfly valve and is controlled by a simple servo motor. The angle of the valve is downloaded to an HCTL1100 (by Hewlet Packard) which then sends a Pulse Width Modulated signal an amplifier which drives the motor. An optical encoder (HEDS 5500 by Hewlet Packard) is used for this position feedback.

A.3.3 Throttle

The setpoint for the rig is set using an plate at the end of the compressor downstream duct. The position of the throttle can be controlled from the computer using a stepper motor.

A.4 Interface Hardware

A.4.1 DAS1602

The DAS1602 by Keithley Metrabyte (and the clones by Computer Boards Inc.) provide up to 16 channels of bipolar A/D, 2 channels of D/A, an auxilary parallel port for digital signals. The A/D channels were used to sample the pressure transducers and the hot-wire anemometer. While the board has 16 channels of A/D, only 8 could be used at the typical access time of 2000 Hz. The auxilary parallel port was used to control the binary aspects of the rig such as: compressor motor on/off, air injector on/off, and downstream throttle opening/closing.

A.4.2 Filters

There are three separate hardware filters used on the rig. This does not include additional filtering that may be done in software in the servo-loop (using Sparrow [36]) or filtering that may be done after the data is collected (using MATLAB© for example).

Passive analog filters

A bank of resistors and capacitors is soldered directly on the input multiplexor of the DAS1602 board. These filters are required to reduce the amount of electrical noise (this noise is generated by the motor power supply) on the A/D lines.

Active analog filters

A series of active analog filters from Frequency Devices Inc. is used for anti-aliasing of the transducer and anemometer signals before sampling. These filters are low

pass four pole Bessel filters and are resistor programmable for cut-off frequencies of 10-5000 Hz. These filters were used with cut-offs of 500 or 1000 Hz.

Digital filters

These filters are from Krohn-Hite, and were used in the low pass, four pole Bessel mode. These were typically used as anti-aliasing filters with cut-off frequencies of 500 or 1000 Hz, but were also used as signal conditioners during closed loop operations.

A.4.3 Data acquisition

The data acquisition is performed using a Pentium based PC. All experimentating was controlled using the Sparrow real-time control kernal as described in [36]. Sparrow provides a set of C routines for accessing I/O boards. Capibilities include executing servo-loops, digital filtering, capturing data, and real time data plotting.

Appendix B

Unactuated Rig Behavior

This appendix contains additional experimental data which was useful for characterizing the behavior of the rig. The data presented here includes measurements of the pressure rise delivered accross the compressor components and detailed measurements of the transition to rotating stall in the compressor annulus.

B.1   Pressure Rise delivered by Rotor and Stator

The total pressure rise delivered by the compressor is divided into two parts, that developed over the rotor and that developed over the stator. On the Caltech compressor rig, roughly 95% of the pressure rise occurs across the rotor. Figure B.1 shows the pressure rise delivered by each compressor component for a variety of flow rates. The measurements were performed by measuring the static wall pressure on each side of the rotor and on each side of the stator using the pressure tranducers described in Appendix A. The data presented in the figure was taken with the rig unstalled. When the rig is operating in a stalled condition, there is a pressure drop accross the stator of nearly 20% of the total pressure rise delivered by the compressor.

B.2   Transition to Stall

In order to understand the development of the rotating stall in the Caltech rig, detailed experimental measurements were performed. Some of the results of these measurements are presented here; these include hotwire measurements of the two distinct types of rotating stall (first mode dominated and second mode dominated) events that were previously described in Section 4.2.2 and span wise hotwire measurements of the transition to rotating stall.

B.2.1   Hot-wire measurements of multiple stall modes

Two stable types of stalled operation have been found on the Caltech rig; time traces of each type are shown in Figure B.2. One type consists is dominated by the first mode, where the first mode corresponds to a pressure perturbation around
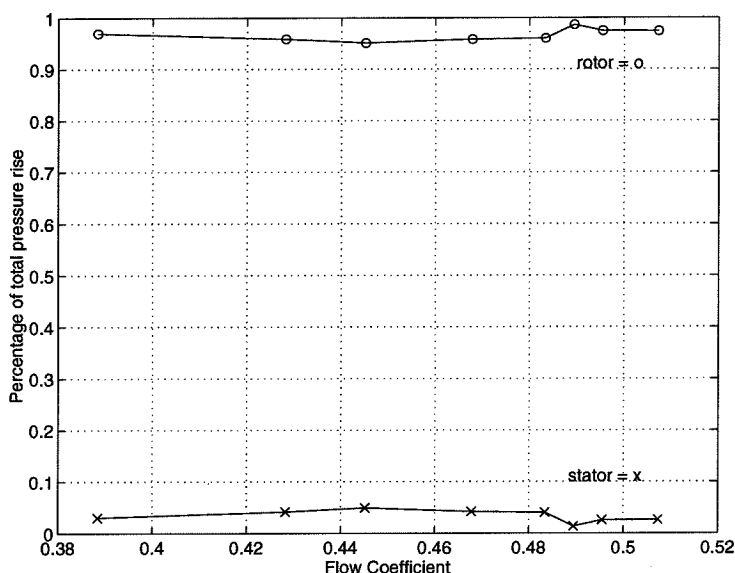
Figure B.1 Percentage of total pressure rise delivered across the rotor
and the stator.

the compressor annulus which has a single minimum and a single maximum (upper
plots in Figure B.2), and the second type is dominated by the second mode (lower
plots in Figure B.2). From the hot-wire measurements presented here, it is not
clear that that the second type of stall is not a single mode type disturbance which
rotates around the compressor annulus at twice the speed of the first type of stall,
but this description has been verified using multiple simultaneous static pressure
measurements around the annulus.

B.2.2   Hot-wire measurements over span

A hotwire anemometer was placed in the compressor annulus upstream 0.2 rotor
radii upstream of the rotor face, and measurements of the local flow rate were made
as the rig transitioned from unstalled to stalled conditions. The measurements show
much higher fluid noise near the tip than near the hub, as well as a decrease in flow
rate at the tip.

The increased noise level suggests that the rotating stall may begin near the tip
of the rotor. The growth rate of rotating stall disturbances seems to be lower in
the tip region (multiple data sets of stall inception in the tip region were taken and
this trend persists), this can be seen in Figure B.3 in the time trace for the hot-
wire at 0.75 span position. Transition to full rotating stall takes at least two full
cycles, where as the other positions the transitions is much more abrupt. Flow rate
measurements over at several span-wise positions need to be taken simultaneously
in order to verify this.

Hot-wire time traces   Spectral content
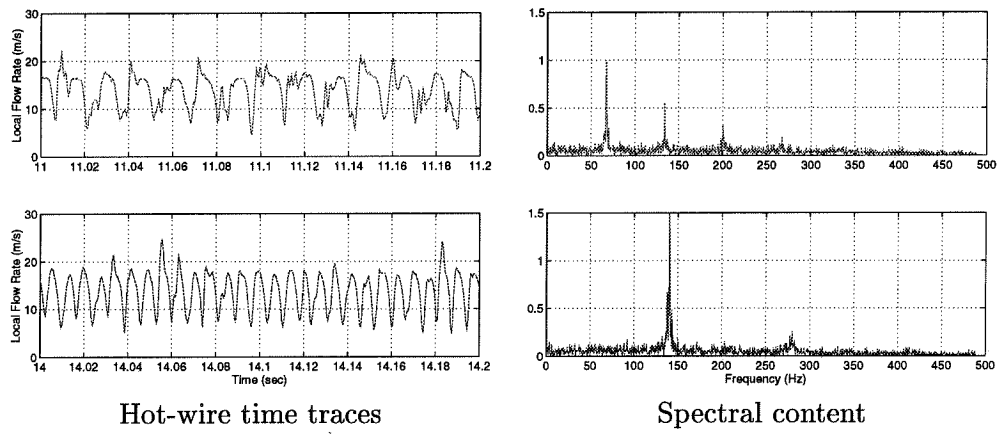
Figure B.2 Two different compressor system states for a fixed throttle setting.
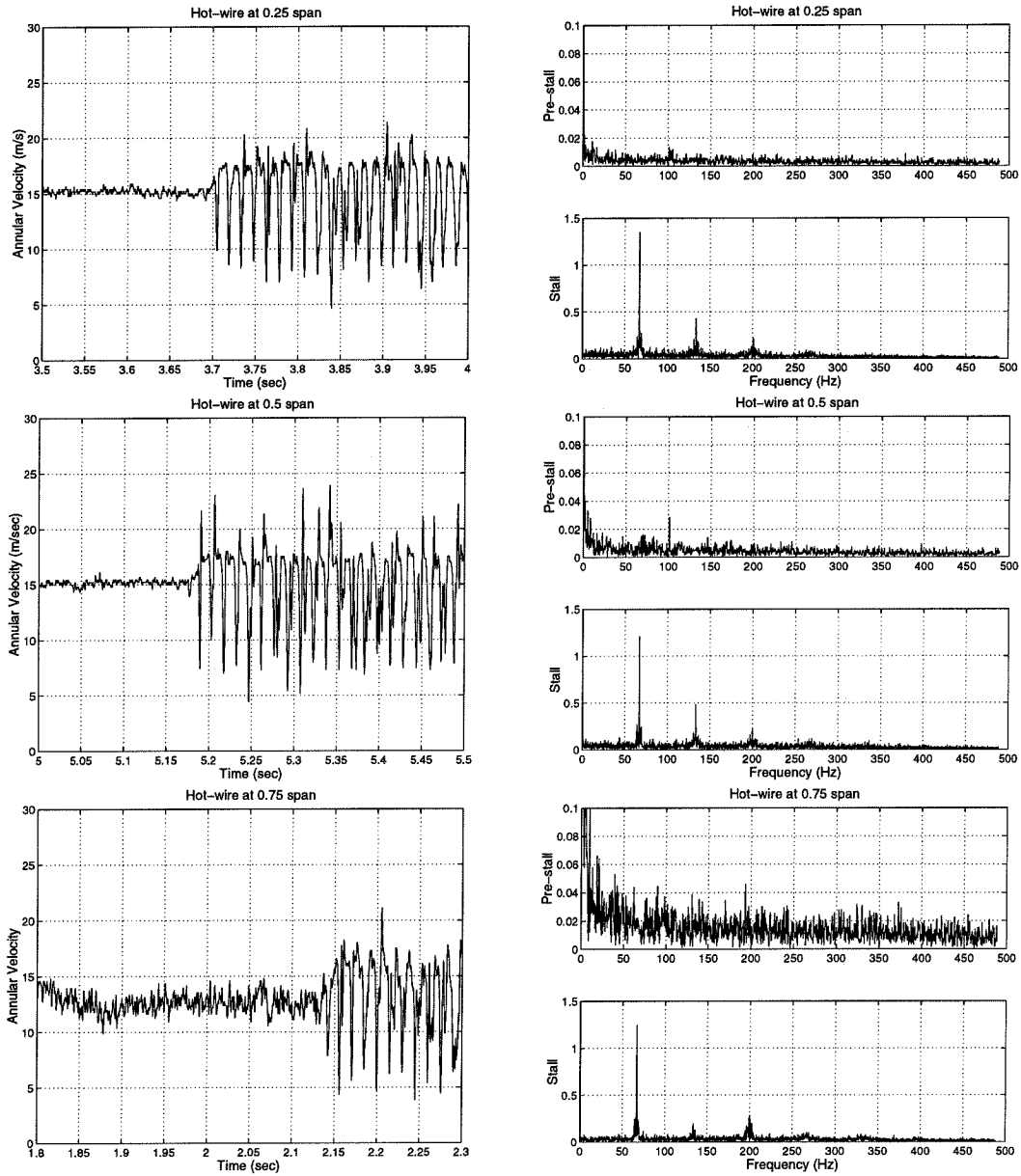
Figure B.3 Hotwire measurements near the rotor face at various span positions.

Appendix C

Characterization of Air Injectors

This appendix deals primarily with the air injection system in place on the Caltech compressor system. The Caltech rig has been previously described in [5], [9], and [27], so the description presented here will be minimal. Figure C.1 gives a description of the air injectors installed on the Caltech rig and some numbers which help describe the system, and Figure C.2 shows the compressor characteristics for the Caltech rig without and with air injection (at the optimal angle).

C.1 Flow Characterization Measurements

The air injectors are supplied with compressed air from the building reservoir at 60 psi. It should be pointed out the 60 psi is measured far upstream of the air injector control valves. Hot-wire measurements were performed to measure the velocity profile of the air injection at the compressor face and presented in [9]. The injected air was found to disperse from 3 mm at the exit of the injector to 2 cm at the compressor face, this dispersion occurs over a distance of 8.9 cm (the distance between the exit of the air injector and the face of the compressor face.) The velocity profile of the injected air at the compressor rotor face is shown in Figure C.3.

The compressor performance characteristics for the Caltech rig are shown in Figure C.2. The figure also shows the decrease in the size of the hysteresis loop for the air injected case.

In the sections to follow, some calculations showing the amount of mass, momentum, and energy flux that the air injection control scheme adds to the compressor system are presented. The values computed are small compared to the values for the overall compression system, suggesting that the air injectors may be an efficient method of increasing the performance of the system. It should also be pointed out that the numbers computed are for continuous air injection (i.e. they correspond to the maximum control authority), and our control strategies operate the injectors intermittently.

All computations are performed based on the compressor performance at the peak of the unactuated compressor characteristic.
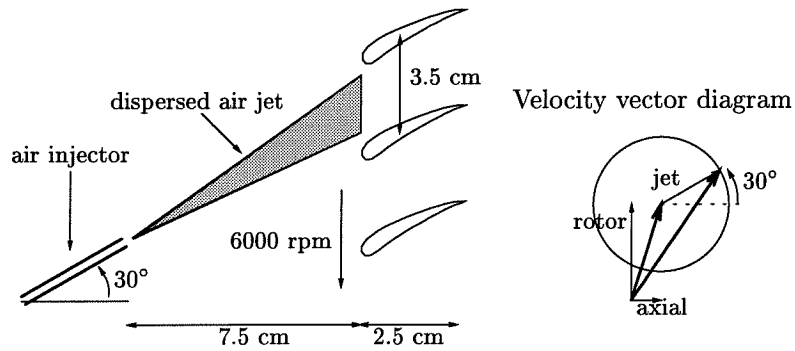
- Velocity in compressor annulus (near stall): 16 m/sec
- Velocity of jet at rotor: 37 m/sec
- Rotor tip velocity: 53 m/sec
- Mass flow through each jet: up to 1.3% of mean flow
- Momentum flux added by each jet: up to 2.3% of momentum flux

Figure C.1 Air Injection on the Caltech rig: some physical parameters.
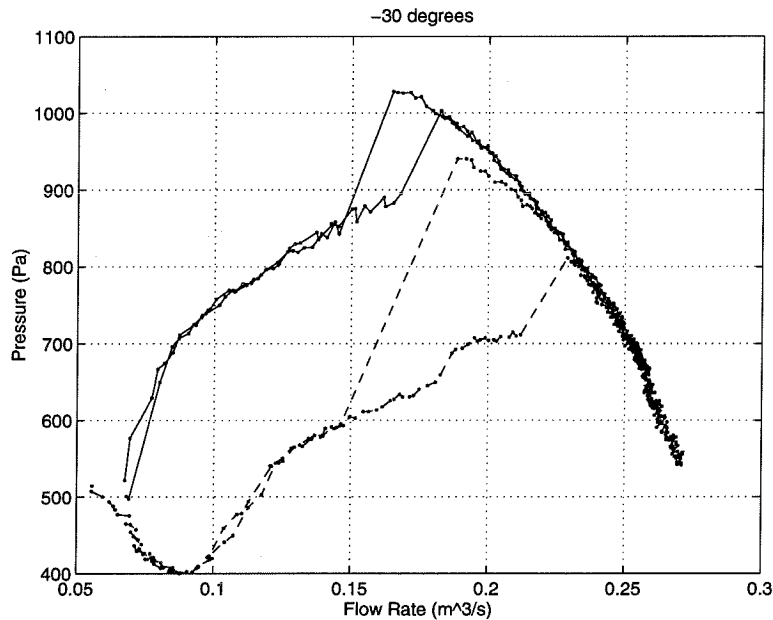
Figure C.2 Compressor performance characteristic for Caltech rig, without air injection: dashed line, with continuous air injection: solid line (corresponding to -30 degrees in Figure 4.7).
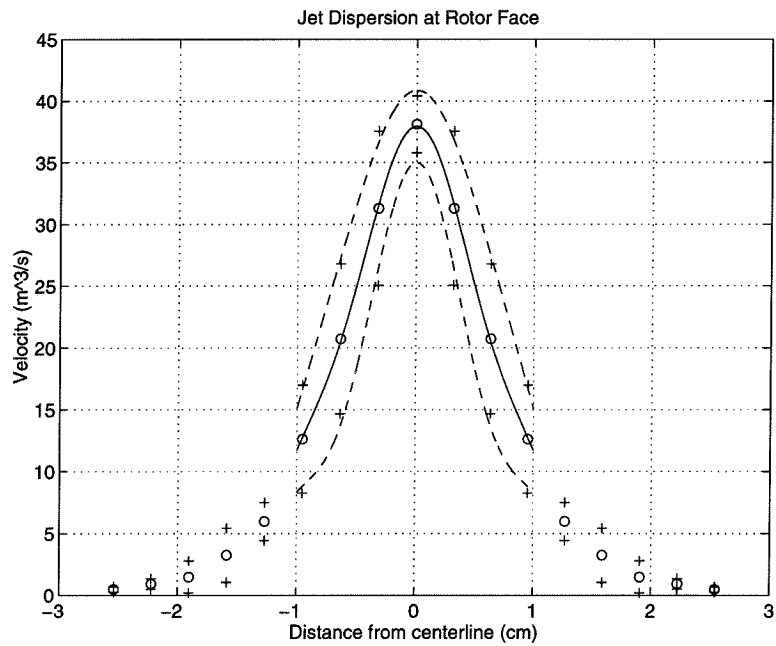
Figure C.3 Velocity profile of the injected air at the compressor face. The points marked with o correspond to mean ($\bar{x}$) value of the velocity at the point, points marked with + correspond to the mean value +/- two standard deviations ($\bar{x}\pm2\sigma$). The solid line corresponds to a least-squares polynomial fit of the $\bar{x}$ values, and dashed lines correspond to polynomial fits of the $\bar{x} \pm 2\sigma$ values.

	Mean $\bar{x}$	Worst case $\bar{x} + 2\sigma$	Best case $\bar{x} - 2\sigma$
a_0	37.93	40.87	34.98
a_1	-71.74	-44.43	-99.04
a_2	99.05	37.29	160.80
a_3	-84.82	-31.76	-137.87
a_4	40.39	17.60	63.19
a_5	-10.34	-5.13	-15.55
a_6	1.33	0.72	1.93
a_7	-0.07	-0.04	-0.09

Table C.1 Coefficients used to fit the experimentally measured air injector velocity profile shown in Figure C.3.

C.1.1 Mass flux

The amount of mass flow through the compressor can be taken directly from the compressor performance characteristic shown in Figure C.2, and is given by $\dot{m}/\rho = 0.19$ m^3/s. The mass flow introduced by a single jet is given by the integral

$$\dot{m} = 2\pi \int_0^R \rho V_j(r) r \, dr, \tag{C.1}$$

where R is the radius over which the injected air has an effect, $V_j(r)$ is the velocity of the injected air as a function of the distance from the center air jet r, and ρ is the density of air. The experimentally determined profile is given by

$$V_j(r)r = a_7 r^{14} + a_6 r^{12} + a_5 r^{10} + a_4 r^8 + a_3 r^6 + a_2 r^4 + a_1 r^2 + a_0, \tag{C.2}$$

where a_i are determined by the polynomial fit to hot-wire measurements of the air injector velocity profile. The coefficients for the polynomial fit to the velocity profile were determined for three cases. The first corresponds to a fit of the average velocity values measured via the hot-wire, the second (worst case) corresponds to a fit of the mean value at the point plus two standard deviations, and the third (best case) corresponds to a fit of the mean minus two standard deviations. The worst case corresponds to the air injectors disturbing the flow by the largest amount, and the best case corresponds to the least amount of disturbance. The values of the polynomial coefficients (the a_i) are given in Table C.1.

The final result was a range for the air injector mass flux with the mean value of $\dot{m} = 0.0039$ kg/s per jet, or that the mass flow added by all three air injectors running continuously is 5.0% of the total mass flow through the compressor. The upper bound for the mass flux (calculated using the upper dashed curve [mean plus two standard deviations] in Figure C.3) was computed as $\dot{m} = 0.0050$ kg/s per jet and the lower bound (calculated using the lower dashed curve in Figure C.3, i.e.

mean minus two standard deviations) was computed as $\dot{m} = 0.0029$ kg/s per jet, or for three jets on continuously, 6.4% and 3.7% respectively.

These numbers were verified for the mass flow through one actuator by collecting the air released from the injector when it was opened for a known amount of time. The result was a value of $\dot{m} = 0.0036$ kg/s, which compares quite well with the results presented for the hot-wire measurements.

C.1.2 Momentum flux

The momentum flux introduced by the air injectors is also a measure of the control authority of the actuators. The momentum flux into the compressor without air injection is given by

$$\dot{p}_a = 2\pi \int_{R_{ai}}^{R_{ao}} V_a(r_a)\rho V_a(r_a)r_a \, dr_a, \tag{C.3}$$

where R_{ai} and R_{ao} are the inner and outer radii of the compressor annulus, $V_a(r)$ is the velocity profile in the compressor annulus as a function of distance from the center of the duct r_a, and ρ is the density of air. For the Caltech compressor rig, $V_a(r_a)$ can be assumed to be a constant over the compressor annulus, and has a value of $V_a(r_a) = 16.3$ m/s, $R_{ai} = 0.060$ m, and $R_{ao} = 0.085$ m. Equation (C.3) then reduces to

$$\dot{p}_a = \rho V_a^2 A_a, \tag{C.4}$$

where A_a is the area of the compressor annulus. For the Caltech rig the momentum flux into the compressor is then $\dot{p}_a = 3.79$ kg m/s^2. The momentum flux introduced by the air injectors is given by

$$\dot{p}_j = 2\pi \int_0^R V(r)\rho V(r)r dr, \tag{C.5}$$

where the variables are as defined in the mass flux section. The values for the momentum flux introduced by the air injectors were computed based on the previously described polynomial fits to the experimentally determined air injector velocity profile. The results are, a mean value for $\dot{p}_j = 0.090$ kg m/s^2, with upper and lower bounds given by $\dot{p}_j = 0.140$ kg m/s^2 and $\dot{p}_j = 0.052$ kg m/s^2 respectively. For three jets on continuously this corresponds to a mean value of 7.1% and upper and lower bounds of 11.1% and 4.0% respectively.

C.1.3 Energy flux

In this section the calculations for the energy produced by the compressor compared to the amount of energy added with the air injectors are shown.

	Units	Velocity Profile Fit		
		$\bar{x} + 2\sigma$	$\bar{x}$	$\bar{x} - 2\sigma$
Mass Flux	kg/s	0.0150	0.0117	0.0087
	% of 0.233 kg/s	6.4	5.0	3.7
Momentum Flux	kg m/s^2	0.420	0.270	0.156
	% of 3.79 kg m/s^2	11.1	7.1	4.0
Energy Flux	watts	12.2	6.9	3.4
	% of 180 watts	6.9	3.8	1.9

Table C.2 Results of control authority calculations.

The amount of work done by the compressor is given by

$$\dot{W} = \frac{\dot{m}}{\rho}\Delta P, \tag{C.6}$$

where $\dot{m}$ is the mass flow rate through the compressor, ΔP is the pressure rise across the compressor, and ρ is the density of air. It should be noted that the simple form of the above equation is due to the very low pressure ratio of the Caltech rig, i.e. the temperature and density changes across the compressor are negligible.

For the Caltech rig near the stall point, $\frac{\dot{m}}{\rho} = 0.19\frac{m^3}{s}$ and $\Delta P = 940$ Pa, and therefore $\dot{W} = 180$ watts.

The amount of energy added by each of the jets can calculated by using the polynomial fit to the experimentally determined velocity profile shown in Figure C.3. The energy flux added by each jet is given by

$$\dot{E} = 2\pi \int_0^R \frac{V_j(r)^2}{2} \rho V_j(r) r \; dr, \tag{C.7}$$

where the variables are as previously defined. The values for the energy flux were computed based on the previously described polynomial fits to the experimentally determined air injector velocity profile. The final result was a range with the mean value of $\dot{E} = 2.3$ watts per jet, or that the power of three air injectors running continuously is 3.8% of the total power that the compressor produces. The upper bound for the energy (calculated using the upper dashed curve in Figure C.3) was computed as 4.16 watts per jet and the lower bound (calculated using the lower dashed curve in Figure C.3) was computed as 1.13 watts per jet, or for three jets on continuously, 6.9% or 1.9% respectively.

C.1.4 Summary

The measurements and calculations presented here for the control authority of the air injectors installed on the Caltech compressor rig are summarized in Table C.2 and show that the actuators are not substantially perturbing the flow through the compressor. The values computed here are upper bounds for the amount of control

effort that could be expended using the air injection scheme, and they correspond to the continuous full actuation case. The mass flow calculations based on the hot-wire measurements were verified by second measurement scheme.

There are several open issues to still be addressed in connection with air injection actuation. Included in these issues is deciding if these calculations are good measures of *control authority* for air injection actuation, particularly as the system is scaled to full size gas turbines. A good measure will be one that decides what amount of control authority is too much and what amount is trivial. If it is determined that these are not good measures, then better ones need to be identified. The introduction of air injection to other compressor systems will help to answer this question.

One possible method for determining if the measures presented are good ones is by determining if the mass/momentum/energy flux introduced by the injectors on the Caltech rig can be duplicated by a recirculation system. If the values cannot be reproduced, the maximum amount of each of these quantities that recirculation can provide needs to be determined. This is part of ongoing work, where measurements will be performed to determine the recirculation flow velocity profile; however, the Caltech rig is limited in terms of recirculation by its low pressure ratio. Comparisons between the velocity profile at the rotor face and that at the exit of a recirculation network might be one way of making feasibility calculations (for air injection actuation) for other systems and also allow the determination of realistic numbers for each of the control authority measures described here.

C.2   Air Injector Activation Lags

The valve activation and deactivation delays described in Section 5.2.3 were determined by measuring the air flow leaving the injector ports relative to the command signal applied to the air injector. Figure C.4 shows and example of this type of measurement. The figure includes the command signal and two time shifted versions of this time signal. The version of the command signal that is shifted by 6.5 ms (dashed line) rises during the actual power rise of the injected air (solid line); this 6.5 ms shift is therefore the activation delay for the air injector. The 4.5 ms time shifted version of the command signal corresponds to the deactivation delay in a similar way. It should be noted that the transport delay from the injector outlet to the rotor face is included in these activation/deactivation delay measurements. This was accomplished by placing the hotwire probe 9 cm from the injector outlet, the same distance that the injector outlet was from the rotor face when the actuator was installed on the rig.
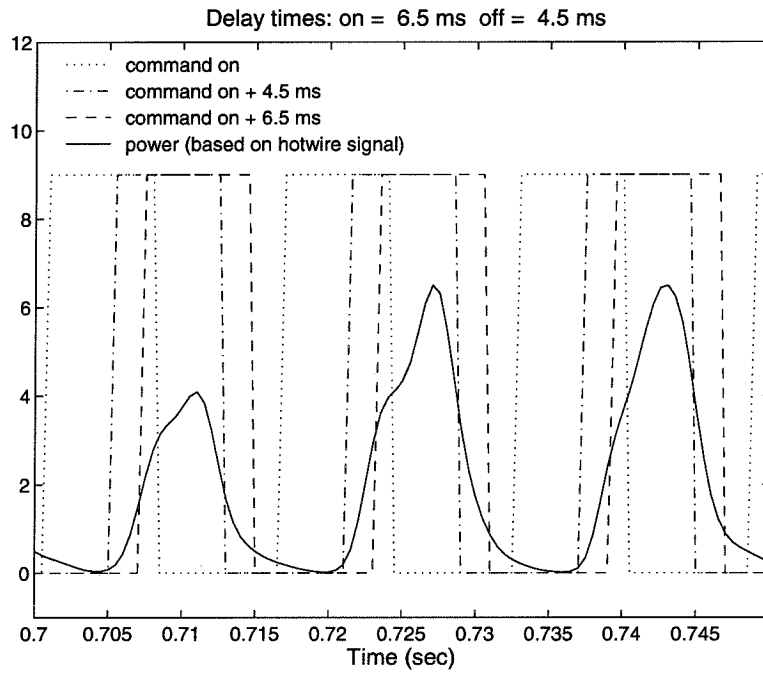
Figure C.4 Time delay and rise time between commanded on signal and actual arrivial of injected flow at the compressor face.

Appendix D

Using Static Pressure Measurements

In the original Moore Greitzer model presented in [35], the equations of motion for rotating stall and surge in axial flow compressor systems were derived in terms of three variables, the average flow coefficient Φ, the average pressure rise coefficient Ψ, and the amplitude of the amplitude of the first Fourier mode of rotating stall A_1. The equations are derived by assuming that the flow coefficient upstream of the rotor face is of the form

$$\phi = \Phi + \delta\phi, \tag{D.1}$$

where the flow coefficient perturbation satisfies Laplaces equation, and can be derived from the potential function $\delta\Theta$,

$$\delta\Theta = \sum_{n=1}^{\infty} \frac{e^{n\eta}}{n} A_n(t) \sin\left(n\theta + r_n(t)\right), \tag{D.2}$$

and the flow coefficient is therefore obtained as

$$\delta\phi = \frac{\partial \delta\Theta}{\partial \eta} = \sum_{n=1}^{\infty} e^{n\eta} A_n(t) \sin\left(n\theta + r_n(t)\right). \tag{D.3}$$

Since potential flow is assumed upstream, these solutions satisfy the Bernoulli (unsteady) equation:

$$\Psi + \delta\psi + \frac{1}{2}(\Phi + \delta\phi)^2 + \frac{\partial \Theta}{\partial \tau} = Constant. \tag{D.4}$$

Far upstream of the rotor:

$$\Psi + \frac{1}{2}\Phi^2 = Constant, \tag{D.5}$$

therefore,

$$\delta\psi + \Phi\delta\phi + \frac{1}{2}\delta\phi^2 + \frac{\dot{\delta\phi}}{|n|} = 0, \tag{D.6}$$

which gives a solution for the static pressure perturbation $\delta\psi$ in terms of $\delta\phi$. If a single mode expansion is used for the flow perturbation $(\delta\phi = A_1(t)\sin(\theta + r_1(t)))$, then

$$\delta\psi = \left(-\frac{1}{2}A_1^2 \sin(\theta + r_1) + \Phi A_1 + \dot{A}_1\right)\sin(\theta + r_1) + A_1\dot{r}_1\cos(\theta + r_1). \quad (D.7)$$

Equation (D.7) can be expanded to include higher modes as well.

Using the Moore Greitzer model cited above, the equations obtained by assuming a third order polynomial for the relationship between the flow coefficient, Φ, through the compressor and the pressure rise across the compressor, $\Psi_c(\Phi)$ are

$$\dot{\Psi} = \frac{1}{4l_cB^2}\left(\Phi - \gamma\sqrt{\Phi}\right), \quad (D.8)$$

$$\dot{\Phi} = \frac{1}{l_c}\left(\Psi_c(\Phi) - \Psi + \frac{A_1^2}{4}\frac{\partial^2\Psi_c(\Phi)}{\partial\Phi^2}\right), \quad (D.9)$$

$$\dot{A}_1 = \frac{a}{1+ma}A_1\left(\frac{\partial\Psi_c(\Phi)}{\partial\Phi} + \frac{A_1^2}{8}\frac{\partial^3\Psi_c(\Phi)}{\partial\Phi^3}\right). \quad (D.10)$$

Substituting equation (D.10) into equation (D.7), and choosing a first Fourier mode expansion for $\delta\psi$ one obtains

$$\delta\psi = \left(\Phi A_1 + \frac{aA_1}{1+ma}\left(\frac{\partial\Psi_c}{\partial\Phi} + \frac{A_1^2}{8}\frac{\partial^3\Psi_c}{\partial\Phi^3}\right)\right)\sin(\theta + r_1) -$$
$$\frac{A_1^2}{2}\sin^2(\theta + r_1) + A_1\dot{r}_1\cos(\theta + r_1). \quad (D.11)$$

On the experiment, the static pressure is measured at six discrete points around the compressor annulus. Using a discrete Fourier transform, the amplitude and phase of the first two modes of the rotating stall pressure perturbation can be determined, and can be represented as

$$\delta\psi = a_1(t)\sin(\theta + r_1(t)) + b_1(t)\cos(\theta + r_1(t))$$
$$= B_1(t)\sin(\theta + r_1(t) + \operatorname{atan}\frac{a_1}{b_1}). \quad (D.12)$$

By setting the sine moments of equations (D.11) and (D.12) equal, a_1 is found as

$$a_1 = \Phi A_1 + \frac{aA_1}{1+ma}\left(\frac{\partial\Psi_c}{\partial\Phi} + \frac{A_1^2}{8}\frac{\partial^3\Psi_c}{\partial\Phi^3}\right), \quad (D.13)$$

and doing similarly for the cosine moments gives b_1 as

$$b_1 = A_1\dot{r}_1. \quad (D.14)$$

This gives a relationship between the first Fourier mode amplitude for the pressure perturbations B_1 and first Fourier mode amplitude for the flow perturbations A_1 as

$$B_1 = A_1 \sqrt{\left[\Phi + \frac{a}{1+am} \left(\frac{\partial \Psi_c}{\partial \phi} + \frac{A_1^2}{8} \frac{\partial^3 \Psi_c}{\partial \phi^3} \right) \right]^2 + \dot{r}_1^2}. \qquad (D.15)$$

Using this relation, given $\Psi_c(\Phi)$, Φ, B_1, a, and m, a set of values of A_1 can be determined. For small values of rotating stall ($A_1 \ll 1$) the magnitude of the pressure perturbation will proportional to the magnitude of the flow perturbation, but for larger values of rotating stall, this relationship gains a strong dependence on the shape of the compressor characteristic. This linear relationship for small amplitudes of stall justifies the power series expansion for the flow coefficient perturbations in terms of the static pressure perturbations used to fit the surge cycle data to rotating stall in equation (6.11), as long as the amplitude of rotating stall is small (< 1).

Bibliography

[1] E. H. Abed, P. K. Houpt, and W. M. Hosny. Bifurcation analysis of surge and rotating stall in axial flow compressors. *Journal of Turbomachinery*, 115:817–824, October 1993.

[2] AMCA/ASHRAE. Laboratory methods of testing fans for rating. Technical Report ANSI/AMCA Standard 210-85, Air Movement and Control Association, 1985.

[3] O. O. Badmus, S. Chowdhury, K. M. Eveker, and C. N. Nett. Control-oriented high-frequency turbomachinery modeling - single-stage compression system one-dimensional model. *Journal of Turbomachinery*, 117:47–61, January 1995.

[4] O. O. Badmus, C. N. Nett, and F. J. Schork. An integrated full-range surge control/rotating stall avoidance compressor control system. In *Proc. American Control Conference*, pages 3173–3180, 1991.

[5] R. L. Behnken, R. D'Andrea, and R. M. Murray. Control of rotating stall in a low-speed axial flow compressor using pulsed air injection: Modeling, simulations, and experimental validation. In *Proc. IEEE Control and Decision Conference*, pages 3056–3061, 1995.

[6] Hoppensteadt F. C. Singular perturbations on the infinite interval. *Trans. Amer. Math. Soc.*, 123(2):521–535, June 1966.

[7] R. D'Andrea. *Generalizations of H-Infinity Optimization and Control of Rotating Stall in an Axial Flow Compressor*. Ph.D. thesis, Department of Electrical Engineering, California Institute of Technology, 1997.

[8] R. D'Andrea, R. L. Behnken, and R. M. Murray. Active control of an axial flow compressor via pulsed air injection. CDS Technical Report 95-029, Caltech, 1995. (To appear *Journal of Turbomachinery*).

[9] R. D'Andrea, R. L. Behnken, and R. M. Murray. Active control of rotating stall using pulsed air injection: A parametric study on a low-speed, axial flow compressor. In *Sensing, Actuation, and Control in Aeropropulsion; SPIE International Symposium on Aerospace/Defense Sensing and Dual-Use Photonics*, pages 152–165, 1995.

[10] I. J. Day. Active supression of rotating stall and surge in axial compressors. *Journal of Turbomachinery*, 115:40–47, 1993.

[11] I. J. Day. Stall inception in axial flow compressors. *Journal of Turbomachinery*, 115:1–9, 1993.

[12] I. J. Day. The fundamentals of stall and surge in axial compressors. In *von Karmon Institute for Fluid Dynamics, Lecture Series 1996-05*, 1996.

[13] H. W. Emmons, C. E. Pearson, and H. P. Grant. Compressor surge and stall propagation. *ASME Transactions*, 6:455–469, 1955.

[14] A. H. Epstein, J. E. Ffowcs Williams, and E. M. Greitzer. Active suppression of aerodynamic instabilities in turbomachines. *Journal of Propulsion and Power*, 5(2):204–211, 1989.

[15] K. M. Eveker, D. L. Gysling, C. N. Nett, and O. P. Sharma. Integrated control of rotating stall and surge in aeroengines. In *Sensing, Actuation, and Control in Aeropropulsion; SPIE 1995 International Symposium on Aerospace/Defense Sensing and Dual-Use Photonics*, pages 21–35, 1995.

[16] P. M. Gerhart and R. J. Gross. *Fundamentals of Fluid Mechanics*. Addison Wesley Publishing Company, 1985.

[17] G. B. Gilyard and J. S. Orme. Subsonic flight test evaluation of a performance seeking control algorithm on an F-15 airplane. In *Joint Propulsion Conference and Exhibit*, pages AIAA paper 92–3743, 1992.

[18] E. M. Greitzer. Surge and rotating stall in axial flow compressors—Parts I and II. *Journal of Engineering for Power*, pages 190–217, April 1976.

[19] E. M. Greitzer. The stability of pumping systems—The 1980 Freeman scholar lecture. *ASME Journal of Fluids Engineering*, 103:193–242, 1981.

[20] E. M. Greitzer and F. K. Moore. A theory of post-stall transients in axial compression systems—Part II: Application. *Journal of Turbomachinery*, 108:231–239, 1986.

[21] J. Guckenheimer and P. Holmes. *Nonlinear Oscillations, Dynamical Systems, and Bifurcations of Vector Fields*, volume 42, of Applied Mathematical Sciences. Springer-Verlag, 1983.

[22] D. L. Gysling. *Dynamic Control of Rotating Stall in Axial Flow Compressors Using Aeromechanical Feedback*. Ph.D. thesis, Department of Aeronautics and Astronautics, Massachusetts Institute of Technology, Cambridge, Massachusetts, 1993.

[23] J. M. Haynes, G. J. Hendricks, and A. H. Epstein. Active stabilization of rotating stall in a three-stage axial compressor. *Journal of Turbomachinery*, 116:226–239, 1994.

[24] G. J. Hendricks and D. L. Gysling. Theoretical study of sensor-actuator schemes for rotating stall control. *Journal of Propulsion and Power*, 10(1):101–109, 1994.

[25] T. P. Hynes and E. M. Greitzer. A method for assessing effects of circumferential flow distortion on compressor stability. *Journal of Turbomachinery,* 109:371–379, 1987.

[26] A. Khalak. *Air-injection Actuation of Rotating Stall in an Axial Fan.* Senior thesis, Department of Mechanical Engineering, California Institute of Technology, 1994.

[27] A. Khalak and R. M. Murray. Experimental evaluation of air injection for actuation of rotating stall in a low speed, axial fan. In *Proc. ASME Turbo Expo,* 1995.

[28] H. K. Khalil. *Nonlinear Systems.* Macmillan Publishing Company, 1992.

[29] M. Krstić, I. Kanellakopoulos, and P. Kokotović. *Nonlinear and Adaptive Control Design.* John Wiley and Sons, 1995.

[30] D. C. Liaw and E. H. Abed. Control of compressor stall inception: A bifurcation-theoretic approach. *Automatica,* 32(1):109–115, 1996.

[31] C. A. Mansoux, D. L. Gysling, J. D. Setiawan, and J. D. Paduano. Distributed nonlinear modeling and stability analysis of axial compressor stall and surge. In *Proc. American Control Conference,* pages 2305–2316, 1994.

[32] F. E. McCaughan. Application of bifurcation theory to axial flow compressor instability. *Journal of Turbomachinery,* 111:426–433, 1989.

[33] F. E. McCaughan. Bifurcation analysis of axial flow compressor stability. *SIAM Journal of Applied Mathematics,* 20(5):1232–1253, 1990.

[34] F. K. Moore. A theory of rotating stall in multistage axial compressors: Parts I, II, III. *Journal of Engineering for Gas Turbines and Power,* 106:313–336, 1984.

[35] F. K. Moore and E. M. Greitzer. A theory of post-stall transients in axial compression systems—Part I: Development of equations. *Journal of Turbomachinery,* 108:68–76, 1986.

[36] R. M. Murray and E. L. Wemhoff. *Sparrow 2.0 Reference Manual.* California Institute of Technology, 1994.

[37] J. D. Paduano. Personal communication, February 1995.

[38] J. D. Paduano, A. H. Epstein, L. Valavani, J. P. Longley, E. M. Greitzer, and G. R. Guenette. Active control of rotating stall in a low-speed axial compressor. *Journal of Turbomachinery,* 115:48–56, January 1993.

[39] J. D. Paduano, L. Valavani, A. H. Epstein, E. M. Greitzer, and G. R. Guenette. Modeling for active control of rotating stall. *Automatica,* 30(9):1357–1373, 1994.

[40] R. H. Sabersky, A. J. Acosta, and E. G. Hauptmann. *Fluid Flow, a First Course in Fluid Mechanics*. Macmillan Publishing Company, 1989.

[41] J. D. Setiawan. Rotating stall inception: Nonlinear simulation and evaluation of unsteady loss effects. In *MIT Advanced Special Project Report*, 1993.

[42] R. H. Smith, J. D. Chisholm, and J. F. Stewart. Optimizing aircraft performance with adaptive, integrated flight/propulsion control. *Journal of Engineering for Gas Turbines and Power*, 113(87–94), 1991.

[43] S. Wiggins. *Introduction to Applied Nonlinear Dynamical Systems and Chaos*, volume 2, of Texts in Applied Mathematics. Springer-Verlag, 1990.

[44] D. G. Wilson. *The Design of High-Efficiency Turbomachinery and Gas Turbines*. MIT Press, Cambridge, 1984.

Index